A Numerical Study on Intraseasonal Variations in Planetary Waves and Ozone Distribution in the Southern Hemisphere Stratosphere

（南半球のプラネタリー波とオゾン分布の季節内変動に関する数値的研究）

Shinji Ushimaru

牛丸 真司

1996年4月

Contents

1 Introduction

1.1 Planetary waves in the stratosphere

Dynamical properties in the stratosphere and mesosphere are much different between the Northern Hemisphere (NH) and Southern Hemisphere (SH). Climatological data show that the westerly jet, whose core is located just above the midlatitude stratopause, is stronger in the SH during wintertime. It is also well known that the polar vortex in SH is stably maintained until when it breaks down in early spring. On the other hand, the vortex in NH is sometimes broken even in midwinter.

The differences originate from the inter-hemispheric asymmetry of the surface undulation and land-sea distribution. Most of the waves propagating into the middle atmosphere are generated in the troposphere. Surface undulation with smaller horizontal scale than several hundreds kilometers generates disturbances, which propagate into the stratosphere and mesosphere as internal gravity waves. Surface undulation with large horizontal scale, like Rocky mountains and Tibetian plateau, causes planetary waves in the midlatitude troposphere. Planetary waves are also generated by land-sea contrasts through the difference of their heat capacities. Planetary waves can propagate into the stratosphere especially in winter season. Both of the undulation and land-sea contrast are more remarkable in NH than SH. Therefore, gravity waves and planetary waves in SH is less active than in NH.

Waves in the middle atmosphere have an important role on the momentum budget. In general, waves transport momentum accompanied by their propagation. When the transported momentum is absorbed into the mean field due to wave breaking or dissipative processes, the mean flow is accelerated or decelerated. The surface-originated waves, like mountain waves and topographical Rossby waves, have momentum whose direction is opposite to the mean flow where the waves are propagating. Namely, these waves decelerates the mean flow when the momentum of the waves is transferred into the mean flow. Since planetary waves and gravity waves are generated from other processes than surface undulation or land-sea contrast, the waves do not always decelerates the mean flow.

The most primitive explanation why the jet and polar vortex is weaker in NH is that the surface-originated waves is stronger in NH than in SH. More sophisticated explanation from the context of the wave-mean flow interaction has been presented by many researchers. If the polar vortex is weak, planetary waves could propagate to the polar region. Since the poleward intrusion of the planetary waves weakens more the polar vortex, the waves can propagate into the polar region and decelerate the polar vortex. Conversely, when the polar vortex is sufficiently strong, planetary waves could not intrude to the polar region. In this case, the strong vortex will be stably maintained unless an extreme amplification of the planetary waves takes place. The former case

corresponds to the situation in NH and the latter case does to that in SH.

Asymmetrical structure of the stratosphere appears not only in the dynamical aspect but also distribution of materials. Zonally averaged column ozone content (total ozone content) is asymmetrically distributed in latitude during winter and early spring, as shown by several observations. Fig.1.1 shows a seasonal change of the latitudinal distribution of total ozone content reported by Dütsch (1971), which was based on the ground-based observations during 1960-1965. Total ozone content in the NH winter and spring takes the maximum at the north pole. On the other hand, it appears around 50° S in SH winter, which is called *subpolar maximum*. The location of subpolar maximum gradually shifts poleward as the season progresses from midwinter to spring, and reaches 65° S in November. Similar seasonal variation in latitudinal ozone distribution is found in a recent satellite observation (*e.g.*, Bowman and Krueger 1985), with an exception of the significant ozone decrease at the south pole in early spring, *i.e.*, *ozone hole*.

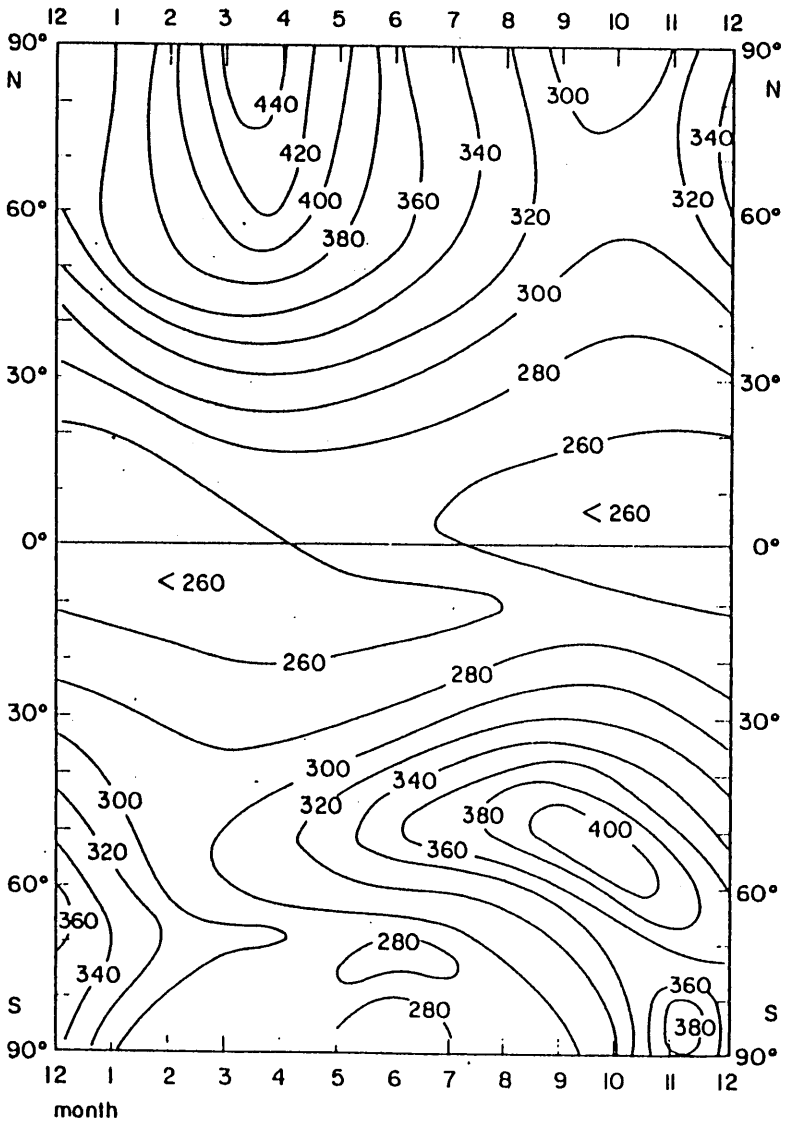

Fig.1.1: Seasonal variation of total ozone content averaged from 1960~1965 (From Dütsch 1971). Contour interval is 20 DU.

It is known that the asymmetric distribution of total ozone content is associated with the difference of wave activity. In NH, planetary waves are frequently amplified in the stratosphere during wintertime. The amplification of the planetary waves induces poleward circulation in the stratosphere and downward circulation in the polar region (Matsuno and Nakamura 1979). The induced circulation increases the ozone amount at the polar region. Accompanied with the extreme amplification of the waves, the polar vortex is broken down and the temperature in the lower stratosphere suddenly increases by several tens degree within a few days; this phenomenon is known as major stratospheric sudden warming. During the warming event, a stronger downward motion is induced at the polar region, and the air mass between midlatitude and highlatitude is well mixed (Hsu, 1981).

In SH, the strong polar vortex is formed in early winter and the vortex stably remains constantly until late spring. The strong polar vortex prevents the intrusion of the planetary waves into the polar region as mentioned above. Consequently, both of the downward motion in the polar region and mixing of the air mass are so weak that the ozone amount remains smaller in highlatitude than that in midlatitude.

The fundamental understandings of the asymmetries of dynamical states and ozone distribution have been reviewed up to here. Quite roughly speaking, the stratosphere in the NH polar region is significantly disturbed by planetary waves, while in SH the planetary wave activity is so weak that the polar vortex is separated from the midlatitude.

The activity of planetary waves in SH is not steady, but significantly varies in winter season somewhat similarly in NH. Remarkable amplitude variations of planetary waves in the stratosphere frequently occur during wintertime with a time scale of a few tens of days, which is called *intraseasonal variation*. Several researchers found based on satellite data that, when a remarkable amplification of planetary wave with wavenumber 1 occurs in the SH stratosphere, the amplification repeats several times with an interval of a few tens of days (Shiotani and Hirota, 1985). This fact leads to an idea that the transport of ozone is caused by intraseasonal variation of the wave activity rather than steady waves. Satellite data of total ozone content also supports the importance of the temporal variation of planetary wave activity as reviewed in next subsection. Therefore, in order to consider precisely the wave-mean flow interaction and related ozone transports, the processes must be treated as transient phenomena.

A review of the previous studies of the planetary wave amplification in the SH stratosphere and interhemispheric asymmetry of ozone distribution associated with planetary wave activity will be presented in the following subsections. The subject and purpose of this thesis will be summarized at the end of this section. Note that hereafter in this thesis, planetary waves with wavenumbers 1, 2, and 3 are sometimes called for simplicity as waves 1, 2, and 3, respectively.

1.2 Interhemispheric asymmetry in column ozone content

Several researchers have elucidated the interhemispheric asymmetry from a standpoint of the meridional circulation in the stratosphere. Rosenfield *et al.* (1987) derived a diabatic circulation from satellite data, and showed that a uniform downward motion covers NH polar region while there is a kink of the downward motion at SH midlatitude middle stratosphere. Plumb and Mahlman (1987) showed that the meridional circu-

lation obtained by GCM tracer experiments exhibits asymmetric pattern in the lower stratosphere; downward motion in NH winter is broadly distributed in midlatitudes and highlatitudes but that in SH winter is located around 35° S. By analyzing GCM data, the similar result was obtained by Iwasaki (1992) based on a pressure-isentrope hybrid coordinate model developed by Iwasaki (1989), which seems closer to a Lagrangian-mean circulation than a transformed Eularian-mean (TEM) circulation.

Several studies have been conducted using two-dimensional model, in which effects of planetary waves are simply introduced by diffusion tensor parametrization, in order to simulate the seasonal variation of total ozone content. Serious efforts to clarify what process mainly cause the interhemispheric asymmetry of ozone distribution have been made by Hou *et al.* (1991). They found that asymmetry of the diffusion tensor (i.e., planetary wave activity) mainly causes the interhemispheric asymmetry of total ozone content through a distinct meridional circulation. However, any experiment using two-dimensional model has not suitably simulated the position of subpolar ozone maximum in SH and subsequent poleward shift; the position of the maximum is located slightly poleward and temporally fixed at about 60°S (Pyle and Rogers 1980; Hou et al. 1991; Akiyoshi and Uryu 1992). The results of two-dimensional models indicate that only the planetary wave activity seems to cause the interhemispheric asymmetry. Other effects work, more or less, to form symmetrical pattern.

Diffusion tensor method is just an approximation to parametrize planetary waves. Planetary waves are treated as if they are turbulent eddies with somewhat ordered structure. Therefore, the meridional circulation obtained from diffusion tensor parameterization may well approximate planetary waves only when the time scales of the variation of zonal-mean fields are much longer than the time scale of individual planetary waves. In the atmosphere, however, the amplitude of planetary waves are significantly varies even within a month (*e.g.*, Hartmann *et al.* 1984, Shiotani and Hirota 1985). Also, the poleward and downward shift of stratospheric jet in SH is controlled by intermittent upward propagation of planetary waves (Mechoso et al. 1985). In NH, some of transient wave amplification lead to stratospheric sudden warmings. Thus, to evaluate the role of planetary waves more exactly, three-dimensional models, which can explicitly treat the planetary waves, must be applied.

1.3 Quasi-periodic variation of total ozone in SH midlatitude

In the previous subsection, asymmetric distribution of the zonally averaged total ozone content was reviewed and simply discussed. The subpolar maximum in SH is likely associated with the planetary wave activity in midlatitude. TOMS (Total Ozone Mapping Spectrometer) data obtained from NIMBUS 7 clearly shows the effects of planetary waves, that is, daily TOMS data show that the distribution of total ozone is considerably varies not only in latitude but also in longitude. Planetary-scale structures are usually more obvious than synoptic-scale structures. The planetary wave disturbance of ozone content has typically wave 1-like structure, where maximum of total ozone content is usually located from 45° E to 90° E in longitude. The structure, however, is not steady but significantly variable.

Fig.1.2 shows the daily TOMS data on 6, 9, 12, 15 in August in 1988. The regions where total ozone content exceeds 400 DU (hereafter called *ozone-rich region*) are broadly distributed around 180° E/W on 6th in August (Fig.1.2a). Localized ozone-rich

regions also exist at around 40° E and 130° E. The structure of the total ozone observed on 9th (Fig.1.2b) is quite different from that on 6th. The ozone-rich region spreading over the date line disappears. Alternatively, an ozone-rich region is formed around 45° E. The maximum value of total ozone content in the region is more than 450DU. 3 days after, the ozone rich region moves eastward about 45 degrees, and the center of the region reaches 90° E on 12th (Fig.1.2c). The structure is maintained until 15th in August (Fig.1.2d). The eastward moving speed is decreased during on 12th to 15th.

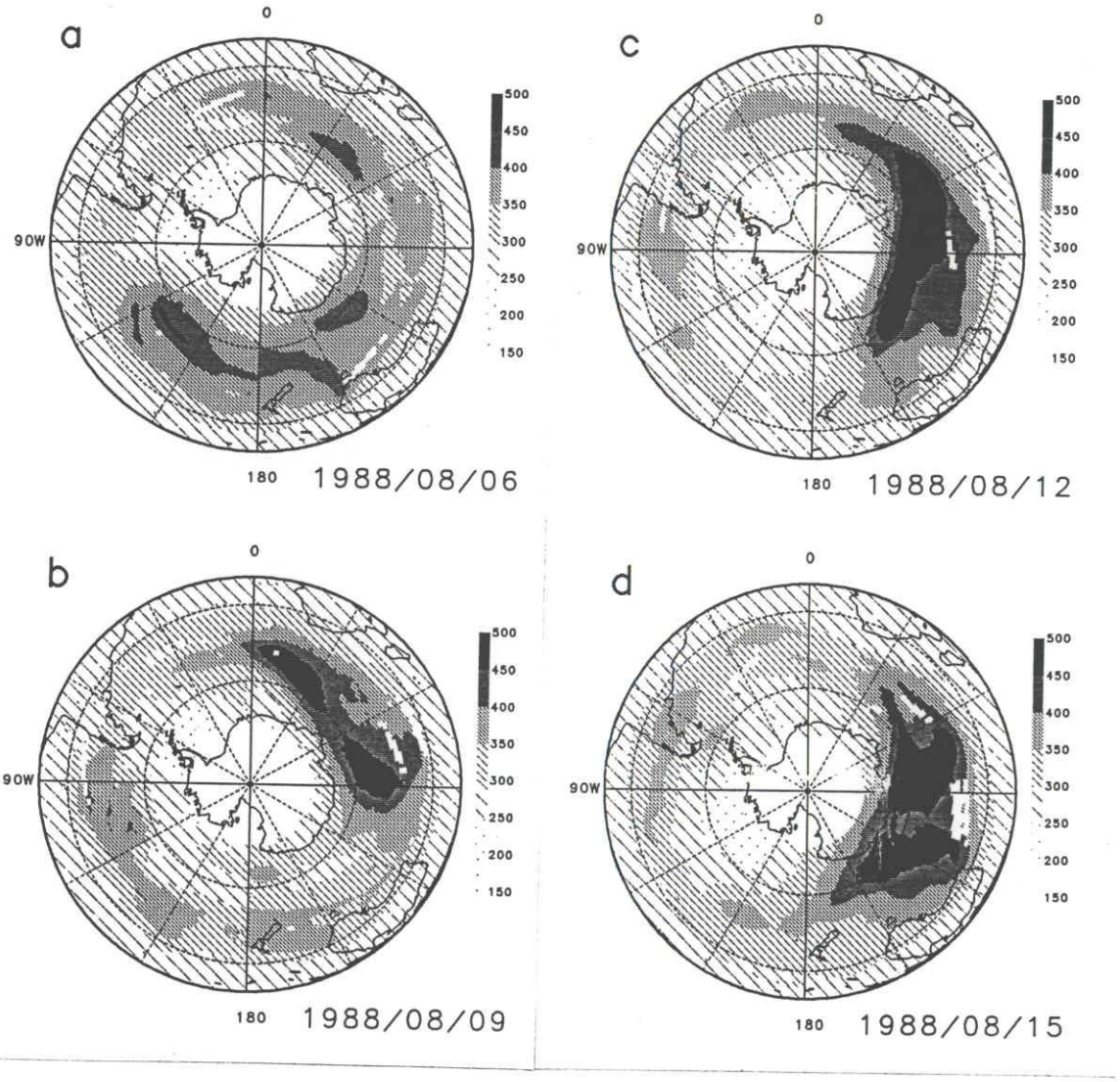

Fig.1.2: Total ozone content on 6, 9, 12, 15 August in 1988 in SH observed by NIMBUS 7, which is provided by NASA Goddard Space Fright Center. There is no data higher latitude than about 75 ° S because of no solar radiation. Since NIMBUS 7 observes the whole sphere during 1 day, the observing duration is different in each longitudinal zone.

In this year, the similar variations of horizontal pattern of the ozone distribution were observed during September and October. Total ozone content at Showa station (39° 35"E, 69° 00"S) was increased quasi-periodically during winter and early spring in 1988 (Kanzawa and Kawaguchi, 1990). When the ozone-rich region was extremely

expanded, Showa station was covered with the region.

The ozone hole in 1988 is considerably distorted by the extension of ozone rich region in midlatitude. The ozone hole in other years is also more or less distorted from a circle although the distortion is less conspicuous compared with that in 1988. The major component of planetary waves in the SH winter stratosphere is stationary wave with wavenumber 1 (Shiotani and Hirota 1985). As reviewed in following subsection, the wave activity in SH varies with the time scale of a few tens of days. The extension of the midlatitude ozone rich region is likely to be associated with the amplification of the wave 1. Therefore, amplification of the planetary wave with wavenumber 1 is remarkably important for the ozone hole dynamics. It is suggested that the poleward transport process of ozone is also strongly affected by the wave 1 amplification based on satellite data in 1992 obtained from the Microwave Limb Sounder on UARS (Upper Atmosphere Research Satellite) (Manney et al., 1993).

1.4 Amplification of planetary wave with wavenumber 1 in SH

As the amplification of planetary wave with wavenumber 1 is concerned, an eastward traveling wave with wavenumber 2 plays an important role. The quasi-stationary planetary wave with zonal wavenumber 1 and the eastward traveling wave with wavenumber 2 frequently coexists during winter and early spring in the SH stratosphere. The eastward traveling wave was first observed by Harwood (1975) and many researchers have analyzed the similar waves by use of satellite data (e.g. Hartmann, 1976; Mechoso and Hartmann, 1982; Mechoso et al., 1988). The period of eastward traveling wave has a large year-to-year variation, raging from 7 to 23 days over 6 winters of 1979-1984 (Shiotani et al., 1990, hereafter referred to as SKH) and the 10 winters of 1979-1988 (Manney et al., 1991a). The eastward traveling wave can only be obviously observed in SH stratosphere.

The generation mechanism of the eastward traveling wave with wavenumber 2 has been studied by several investigators. One candidate for the generation is baroclinic instability which is categorized as *Green mode* (Geisler and Garcia, 1977; Hartmann, 1979). The generation of eastward traveling waves is also considered to be formed as an upward cascade of synoptic scale waves. By using a GCM of dry atmosphere, Young and Houben (1989) demonstrated that eastward traveling modes having wavenumbers 1 to 3 were generated in the upper troposphere by wave-wave coupling of synoptic scale waves in the troposphere. Another candidate is associated with barotropic instability produced by horizontal wind shear in the stratosphere (Hartmann, 1983; Manney et al., 1991b). However, at present, a definite conclusion of the generation mechanism for the wave 2 has not been definite.

On the other hand, the stationary wave 1 is considered to be a forced wave through the tropopause (Hirota et al., 1990, hereafter referred to as HKS). Wave 1 is similar to its counterpart in NH except that the amplitude of the southern wave is usually weaker. Activity of wave 1 in the stratosphere is usually intensified by the poleward and downward shift of the westerly stratospheric jet (Shiotani and Hirota, 1985; Mechoso et al., 1988), in the season from late August to early September. The amplitude of wave 1 exhibits a remarkable temporal variation during wintertime. In particular, the periodic amplification of wave 1 with a period of 17 days during August to September in 1988 (HKS), has attracted considerable attention in connection with significant ozone

increase at the Showa station (Kanzawa and Kawaguchi, 1990).

The most significant finding by SKH and HKS is the clear relationship between the amplitude variation of wave 1 and the relative longitudinal location of the waves: the amplitude of wave 1 reaches its maximum when the ridge of the traveling wave 2 overlaps that of wave 1 (Fig.1.3). The same relationship can be found during August to September in 1971 (Levy and Webster, 1976) and during August in 1973 (Hartmann, 1976), although the relationship is not always well satisfied in every winter (Manney et al., 1991a).

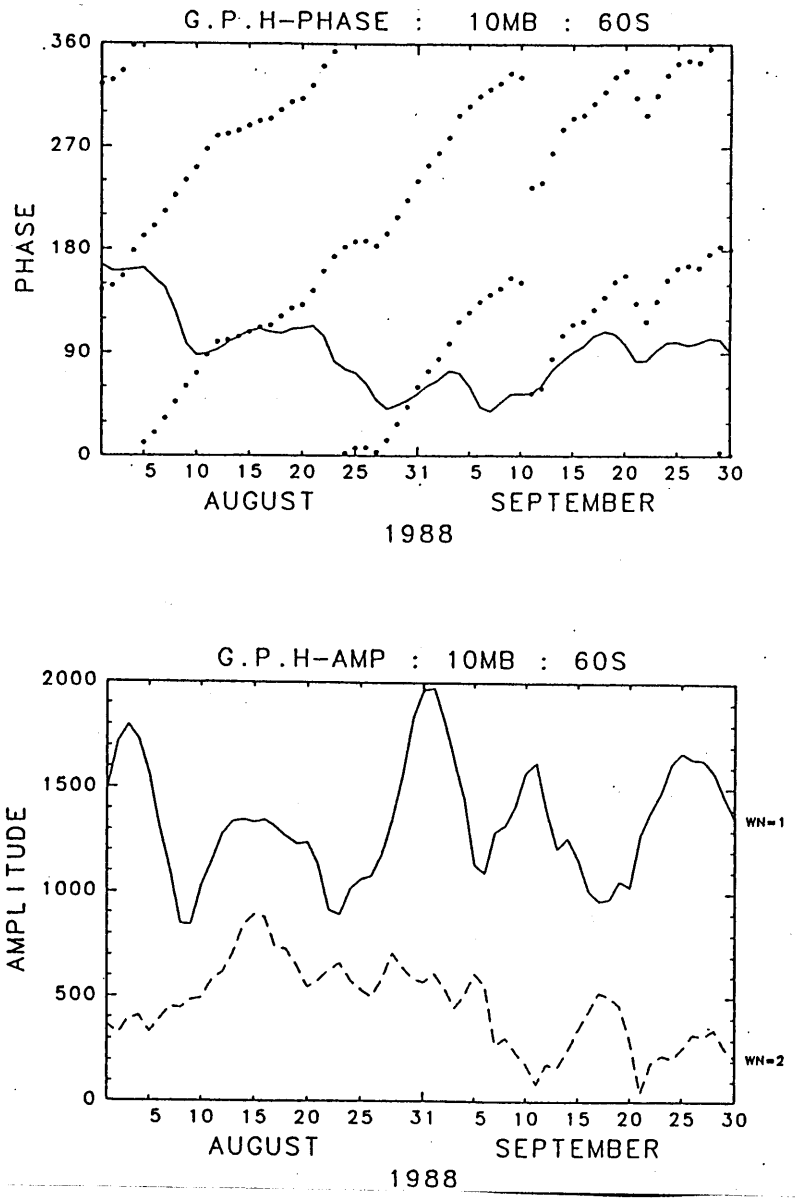

Fig.1.3: Temporal variation of phase angle of ridge (upper panel) and amplitude (lower panel) of wavenumber 1 and at 10 mb along 60° S. (After Hirota et al., 1990)

This relationship between wave 1 and wave 2 suggests that the amplitude variation of wave 1 is a result of the wave-wave interaction between wave 1 and wave 2, as stated in HKS. The incoherence of amplitude variations between the troposphere and stratosphere (Mechoso and Hartmann, 1982) also supports the idea that the wave interactions in the

stratosphere causes the variation. The mechanism of the interaction, however, has not been fully understood.

Amplitudes variations due to the interaction between eastward traveling wave and stationary wave with the same wavenumbers were studied by Hirota (1971) and Hirooka (1986). Hirota(1971) showed that superposition of upward propagating stationary wave and westward traveling wave leads to an amplitude variation of composite wave in the upper stratosphere. While, Hirooka (1986) explained a periodic amplitude variation of wave 1 in the light of linear interference between eastward traveling wave 1 and quasi-stationary wave 1. Their studies are essentially based on a linear theory, i.e., interference of the waves with the same wavenumbers. The interaction between waves with different wavenumbers is hardly explained by the linear interference.

Amplitude variations of waves 1 and 2 are frequently observed also in NH and the variations are negatively correlated each other (wave 1-wave 2 vacillation). Smith et al. (1984) showed based on an analysis of the potential enstrophy budget that the negative correlation between the amplitudes of waves 1 and 2 for the 1988/1989 winter event was generated by the interaction between wave 1 and wave 2 in the stratosphere. Robinson (1985) simulated the wave 1-wave 2 vacillation in NH using severely truncated spectral model on a β-channel. The author assumed that stationary waves 1 and 2 are generated by the surface topography and a westward traveling wave 1 is forced at the surface. The westward wave is frequently observed in NH stratosphere (Madden, 1978). The numerical experiments showed that the amplitude variation of wave 1 is a result of the variation of the interaction with the mean flow, and the interaction is controlled by the interference between the stationary wave 1 and westward traveling wave 1, while the variation of wave 2 is mainly caused by the wave 1-wave 2 interaction. The mechanism of the variations of waves 1 and 2, however, may depends on the forcing of the waves from the troposphere, which is quite different between Northern and Southern Hemispheres; westward traveling waves are dominant in the Northern Hemisphere while eastward wave 2 in the Southern Hemisphere.

1.5 Subject and purpose

As described above, zonally averaged total ozone content in SH has a maximum at midlatitude in winter, while the ozone distribution in NH are monotonously increased polewardly throughout wintertime. As the wave activity of planetary waves in SH is less strong than in NH, planetary waves cannot destroy the polar vortex. The waves can, however, distort the polar vortex quasi-periodically and can affect ozone distribution. Ozone distribution in winter is considerably different between NH and SH. The largest variation of wave amplitude has been observed in the planetary wave with wavenumber 1. Therefore, it is expected that transient processes, i.e., temporary varying wave activity in the stratosphere, are essential to consider the processes of wave-mean flow interaction and transports of materials. Firstly in this thesis, the characteristics of the interhemispheric asymmetry in ozone transport due to amplification of a single planetary wave originated and amplified from the tropopause level is explored. From the obtained characteristics, roles of planetary waves on the seasonal variation of ozone distribution in SH will be discussed there. Secondary, the amplification of quasi-stationary planetary wave with wavenumber 1 will be examined based on the interaction of eastward traveling wave with wavenumber 2 in the stratosphere in order to realize the realistic horizontal distribution of total ozone content and its temporal variation. Finally, the mechanism

of the wave 1 amplification due to the interaction with the eastward traveling wave is analyzed in detail.

To simulate explicitly the transient process and wave-wave interaction and wave-mean flow interaction, a three dimensional model is used in this study. Model experiments are performed under some idealized conditions of the stratospheric phenomena. Neverthless, this simulation could extract an essence of the dynamical processes appearing in the stratopshere. The data obtained by numerical experiments are analyzed and interpreted with the aid of presented theoretical knowledge.

The model used in this study is described in the next section. The different role of planetary waves on the zonally averaged ozone distribution between SH and NH is presented in Section 3. The results of the horizontal ozone distribution for the case of coexisting of a stationary wave with wavenumber 1 and an eastward wave with wavenumber 2 are shown in Section 4. The mechanism of amplification of wave 1 due to the interaction with wave 2 are shown in Section 5. This thesis is summarized in the last section. Furthermore, lists of symbols and related discussion are described in Appendices.

2 Model description

Semispectral models are developed to simulate the dynamical phenomena and transport process of ozone in the middle atmosphere. Two models are used in this resarch. One is a hemispherical models and the other is a sherical model. The hemispherical model covers the region from the equator to the pole in latitude, and the spherical models does the whole sphere of the earth. Both models cover the height region from 10 km to 110 km.

2.1 Governing equations

The model is based on the primitive equations including metric force; the equations are the same as those given in Holton (1976). The governing equations described in flux form are as follows. The symbols used in this paper are lisetd in Appendix A. Equation of motion in longitudinal direction

$$\frac{\partial u}{\partial t} + \frac{1}{a\cos\theta}\frac{\partial u^2}{\partial \lambda} + \frac{1}{a\cos^2\theta}\frac{\partial}{\partial \theta}(uv\cos^2\theta) - fv + \frac{1}{a\cos\theta}\frac{\partial \Phi}{\partial \lambda} = X \tag{2.1}$$

Equation of motion in latitudinal direction

$$\frac{\partial v}{\partial t} + \frac{1}{a\cos\theta}\frac{\partial uv}{\partial \lambda} + \frac{1}{a\cos\theta}\frac{\partial}{\partial \theta}(v^2\cos\theta) + \frac{1}{a}\tan\theta u^2 + fu + \frac{1}{a\cos\theta}\frac{\partial \Phi}{\partial \theta} = Y \tag{2.2}$$

Thermodaynamic equation

$$\frac{\partial T}{\partial t} + \frac{1}{a\cos\theta}\frac{\partial Tu}{\partial \lambda} + \frac{1}{a\cos\theta}\frac{\partial (Tv\cos\theta)}{\partial \theta} + \frac{RT}{C_pH}w = Q \tag{2.3}$$

Mass conservation

$$\frac{1}{a\cos\theta}\frac{\partial u}{\partial \lambda} + \frac{1}{a\cos\theta}\frac{\partial (v\cos\theta)}{\partial \theta} + \frac{1}{\rho_0}\frac{\partial \rho_0 w}{\partial z} = 0 \tag{2.4}$$

Static Equilibrium

$$\frac{\partial \Phi}{\partial z} = \frac{R}{H}T \tag{2.5}$$

Where, X and Y are dissipative terms of the momentum (eg., Rayleigh friction and vertical diffusion), and Z is a diabatic heating term.

2.2 Disipative processes

The zonal mean temperature field is forced to be restored to the standard value by Newtonian cooling. The standard values are taken as the initial temperature field which is constructed from the initial zonal wind with the aid of thermal wind relation of gradient wind balance. Accordingly, the model month is fixed as the month of the initial zonal wind during the calculation.

Newtonian cooling is incorporated to express the dissipative process which represents the dissipation of wave energy and the restoration of the zonal-mean field to a standard temperature. The coefficient of Newtonian cooling is the same as that used in Holton (1976). A sponge layer is placed near the top boundary, making use of Rayleigh friction. The vertical profiles of the Newtonian cooling coefficient (α) and Rayleigh friction (ν_{RF}) are shown in Fig.2.1. Fourth order vertical diffusion is adopted to suppress any numerical instability from both the zonal-mean and wave components. The coefficient used in the present study can be written as

$$\nu_z = 10^{-5} \exp\left\{\frac{z - 90km}{20km}\right\} \quad [\mathrm{s}^{-1}] \,. \tag{2.6}$$

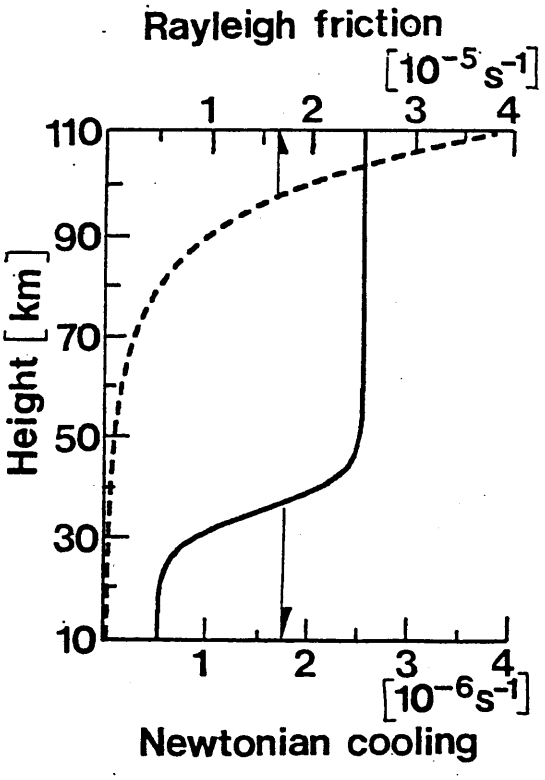

Fig.2.1: Vertical profiles of the Newtonian cooling coefficient (α, solid line) and Rayleigh friction coefficient (ν_{RF}, dashed line).

2.3 Spectral transform

All of the physical quantities are expanded into complex Fourier series in the zonal direction, as similar to Hsu(1981). Geopotential (ϕ), zonal wind (u), meridional wind (v), and temperature (T) are written as

$$\phi(\lambda,\theta,z) = \sum_{k=-N}^{N} \Psi_k(\theta,z)\, e^{ik\lambda}\, e^{\frac{z}{2H}}, \tag{2.7}$$

$$u(\lambda,\theta,z) = \sum_{k=-N}^{N} U_k(\theta,z)\, e^{ik\lambda}\, e^{\frac{z}{2H}}, \tag{2.8}$$

$$v(\lambda,\theta,z) = \sum_{k=-N}^{N} V_k(\theta,z)\, e^{ik\lambda}\, e^{\frac{z}{2H}}, \tag{2.9}$$

and

$$T(\lambda,\theta,z) = \sum_{k=-N}^{N} T_k(\theta,z)\, e^{ik\lambda}\, e^{\frac{z}{2H}}, \tag{2.10}$$

where λ,θ,z are the longitude, latitude, and altitude, respectively, N the truncation number, k the zonal wavenumber, and H the scale height (7 km). The model is formulated so that an arbitrary truncation of the expanded wavenumbers is possible.

The momentum, thermodynamic, continuity, and hydrostatic equations for the zonal-mean and wave components are written as

- zonal-mean component

$$\frac{\partial U_0}{\partial t} = f\,V_0 - \frac{e^{\frac{z}{2H}}}{a\cos^2\theta}\frac{\partial}{\partial\theta}\left\{\sum_{n=1}^{N}(U_nV_n^* + U_n^*V_n)\cos^2\theta\right\} + e^{\frac{z}{2H}}U_0V_0\frac{\tan\theta}{a}, \tag{2.11}$$

$$\frac{\partial V_0}{\partial t} = -f\,U_0 - \frac{1}{a}\frac{\partial\Psi_0}{\partial\theta} - e^{\frac{z}{2H}}U_0^2\frac{\tan\theta}{a}, \tag{2.12}$$

$$\frac{\partial T_0}{\partial t} = -\frac{H}{R}N_{BV}^2W_0 - \frac{e^{\frac{z}{2H}}}{a\cos\theta}\frac{\partial}{\partial\theta}\left\{\sum_{n=1}^{N}(T_nV_n^* + T_n^*V_n)\cos\theta\right\} - \alpha(T_0 - T_R), \tag{2.13}$$

$$\frac{1}{a\cos\theta}\frac{\partial}{\partial\theta}(V_0\cos\theta) + (\frac{\partial}{\partial z} - \frac{1}{2H})W_0 = 0, \tag{2.14}$$

$$(\frac{\partial}{\partial z} + \frac{1}{2H})\Psi_0 = \frac{R}{H}T_0, \tag{2.15}$$

- wave components ($k = 1 \sim N$)

$$\frac{\partial U_k}{\partial t} = -ik\frac{e^{\frac{z}{2H}}}{a\cos\theta}U_0U_k - \frac{e^{\frac{z}{2H}}}{a\cos\theta}V_k\frac{\partial(U_0\cos\theta)}{\partial\theta} + f\,V_k - \frac{ik}{a\cos\theta}\Psi_k + A_k - \kappa U_k - \nu\frac{\partial^4U_k}{\partial z^4}, \tag{2.16}$$

$$\frac{\partial V_k}{\partial t} = -ik\frac{e^{\frac{z}{2H}}}{a\cos\theta}U_0V_k - 2\frac{\tan\theta}{a}e^{\frac{z}{2H}}U_0U_k$$

$$-f\ U_k - \frac{1}{a}\frac{\partial \Psi_k}{\partial \theta} + B_k - \kappa V_k - \nu\frac{\partial^4 V_k}{\partial z^4}\ , \tag{2.17}$$

$$\frac{\partial T_k}{\partial t} = -ik\frac{e^{\frac{z}{2H}}}{a\cos\theta}U_0 T_k - \frac{e^{\frac{z}{2H}}}{a}\frac{\partial T_0}{\partial \theta} - \frac{H}{R}N_{BV}^2 W_k + C_k - \alpha T_k - \nu\frac{\partial^4 T_k}{\partial z^4}\ , \tag{2.18}$$

$$\frac{ik}{a\cos\theta}U_k + \frac{1}{a\cos\theta}\frac{\partial}{\partial\theta}(V_k\cos\theta) + (\frac{\partial}{\partial z} - \frac{1}{2H})W_k = 0\ , \tag{2.19}$$

$$(\frac{\partial}{\partial z} + \frac{1}{2H})\Psi_k = \frac{R}{H}T_k\ , \tag{2.20}$$

where T_R is the standard temperature which is fixed at an initial temperature. Asterisks part on the variables represent complex conjugates. A_k, B_k, and C_k denote the wave-wave interaction terms; details of which are presented in Appendix B.

2.4 Grid system and time integration

The grid system is designed with a staggered grid in the meridional direction with an interval of 5° . The grid for U_0, V_0, Ψ_k, W_k, and T_k is designed on the latitude from 5° to 85° for the hemispherical model and -85° to 85° for the spherical model. On the other hand, the grid for Ψ_0, W_0, T_0, U_k, and V_k from 2.5° to 87.5° for the hemispherical one and -87.5° to 87.5° for the spherical one. The vertical grid interval (Δz) is 2km and the grid points for all variables are constructed on the same levels. A semi-implicit method is used for the time integration with a time step of 15 minutes (Δt). The time-averaged variable ($\hat{F}^n$) at n-th time step is defined as

$$\hat{F}^n = F^{n+1} - F^n + F^{n-1}\ .$$

Then, the time derivative with a centered-difference of F is written as

$$\frac{\partial F}{\partial t} = \frac{\hat{F}^n + F^n - 2F^{n-1}}{2\Delta t}\ .$$

The time-averaged variable is substituting into the Coriolis, pressure gradient and adiabatic terms in the momentum and thermodynamic equations. While, for the variables in the nonlinear terms (wave-wave interaction terms), the variables of n-th step (F^n) are used. The variables of (n-1)th step (F^{n-1}) are used for the variables in the dissipation term (Rayleigh friction, Newtonian cooling, and the vertical viscosity). This method of time integration is the same as in Hsu (1981). Consequently, the equations becomes two dimensional Poisson equations for variable $\hat{F}$. The equations are solved by the dimension reduction method.

2.4.1 Boundary conditions

The bottom and top boundaries of the models are set at 10 km and 110 km, respectively. The lateral boundaries for the spherical model are at the north and south poles, while those for the hemispherical model are at the pole and equator.

Zonal-mean zonal wind is fixed at the initial value and zonal-mean meridional wind is assumed zero at the bottom boundary. The latter condition is required to statify the former condition. We assume that the geopstrophic relation is sataified at

the boundaries, which requires that the zonal-mean component of geopotential is also fixed at the initial value.

All the wave components except for forced waves have no value at the lower boundary. Geopotential of the fundamental wave is externally specified and the meridional and zonal winds of the component are determined from the geostrophic relation. Every wave component can be assumed to be zero at the top boundary since all waves are absorbed in the sponge layer near the top boundary.

The vetical and lateral bounday conditions are as follows;

- Bottom boundary ($z = z_B$)

$$\frac{\partial U_0}{\partial t} = V_0 = \frac{\partial \Psi_0}{\partial t} = 0 \tag{2.21}$$

$$\Psi_r = f(t, \theta) \qquad (r; \text{wavenumber of forced wave}) \tag{2.22}$$

$$\Psi_k = 0 (k = 1 \sim M, k \neq r) \tag{2.23}$$

- Top boundary ($z = z_T$)

$$\frac{\partial U_0}{\partial t} = V_0 = \frac{\partial \Psi_0}{\partial t} = 0 \tag{2.24}$$

$$\Psi_k = T_k = U_k = V_k = W_k = 0 \quad (k = 1 \sim M) \tag{2.25}$$

- Polar Boundary ($\theta = \pm 90^o$)

$$U_0 = V_0 = \frac{\partial \Psi_0}{\partial \theta} = \frac{\partial W_0}{\partial \theta} = \frac{\partial}{\partial \theta} \left(\frac{U_0}{\cos \theta} \right) = 0 \tag{2.26}$$

$$\frac{\partial U_1}{\partial \theta} = \frac{\partial V_1}{\partial \theta} = \Psi_1 = W_1 = 0 \tag{2.27}$$

- Equatorial Boundary ($\theta = 0^o$) (only for hemisperical model)

$$\frac{\partial U_0}{\partial t} = V_0 = \frac{\partial W_0}{\partial \theta} = \frac{\partial \Psi_0}{\partial \theta} = 0 \tag{2.28}$$

$$\frac{\partial U_k}{\partial \theta} = V_k = W_k = \Psi_k = T_k = 0 \quad (k = 1 \sim M) \tag{2.29}$$

2.4.2 Initial zonal-mean zonal wind

Climatological monthly averaged zonal-mean winds from late autumn to early spring are used as the initial zonal-mean winds for experiments, which are shown in Fig.2.2. The monthly averaged zonal-mean winds in the stratosphere and the mesosphere are obtained from composites of satellite data of 5 years from 1973 to 1978 (Fleming et al. 1988).

For the experiments using the hemispherical model, the winds in SH from July to October are adopted as initial winds . On the other hand, all the winds shown in Fig.2.2 are used for the experments using the spherical model.

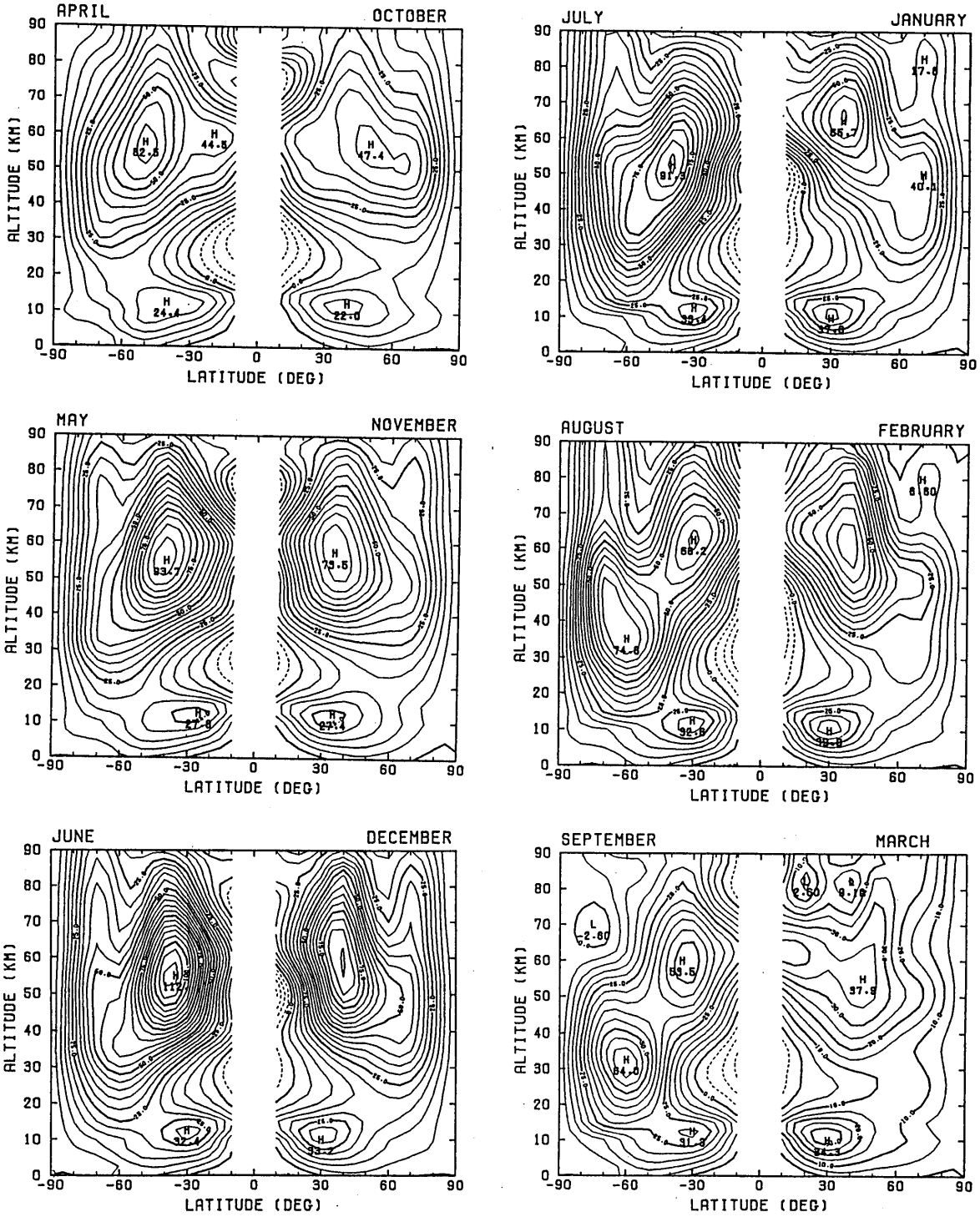

Fig.2.2: Monthly averaged zonal-mean zonal wind from late autumn to early spring. Left-hand side in each panel shows that in SH and right-hand side in NH. The month of each hemisphere is shifted for six months to show the wind in same season. Contour interval is 5 m^{-1} and negative value is indicated by dashed line.

3 Interhemispheric asymmetry of the total ozone

In this section, results and discussion concerned with roles of the planetary waves on the interhemispheric asymmetry of the ozone are presented. The spherical model is used to simulate to the wave-mean flow interaction and transport process of the ozone associated with the planetary wave amplification.

A series of numerical experiments using a truncated semi-spectral model is conducted under the following experimental conditions; monthly averaged zonal-mean winds are used as initial conditions, and the amplification of planetary waves is represented by the growth of geopotential undulation of the lower boundary. Characteristics of seasonal variation of the ozone distribution is overviewed by connecting the short-range simulation, i.e., one month prediction. Then, it will be indicated that wave amplification in the middle atmosphere is substantial for formation of the subpolar ozone maximum in SH and essential for subsequent poleward shift toward early spring.

In order to simulate seasonal variations of the stratospheric circulation and ozone distribution, the models must contain all the effects of chemical, radiative and dynamical processes which contribute to these variations. Then they can precisely reproduce the seasonal variation of the mean zonal fields. Experiments using GCM and two-dimensional interactive models include these processes. The seasonal variation of zonal-mean fields, however, is still difficult to be correctly simulated even in GCM. The seasonal variations reproduced in two-dimensional models have large discrepancies from the observation. Then, instead of calculating the seasonal variations of zonal-mean fields, observed monthly averaged zonal-mean winds are used as initial conditions for one month (or shorter) predictions. Furthermore, the model does not include the processes which contribute to form symmetric latitudinal ozone distributions; chemical reactions, solar and infrared heating/cooling and equatorial convections. They do not make substantial interhemispheric asymmetry without difference in planetary wave activities as shown by Hou et al.(1991).

The experimental configuration in this section is briefly described in next subsection. Residual circulations and variations of total ozone content for various months are presented in Section 3.2, and the circulations are diagnosed in Section 3.3. Section 3.4 describes dependency of the residual circulation on wave forcing. Results in this study are summarized and discussed in Section 3.5.

3.1 Configuration of experiments

3.1.1 Wave forcing

A planetary wave with wavenumber 1 or 2 is the fundamental wave which is forced at the lower boundary in the form of geopotential height field. The amplitude is distributed over the latitudes of 30°–90° only in winter hemisphere and the maximum perturbation is located at 60° (Fig.3.1a). The wave amplitude increases and keeps constant till day 15, and then decays rapidly (Fig.3.1b). The functional form is as follows.

- From April to September

$$\Psi_r/g = \begin{cases} 0 & (-\pi/6 \leq \theta \leq \pi/2) \\ \Psi_{max} \sin^2(3\theta - \pi/2)\,[1 - \exp(-\frac{t}{\tau})] \exp(-\frac{z_B}{2H}) & (-\pi/2 \leq \theta \leq -\pi/6) \end{cases}$$

- From October to March

$$\Psi_r/g = \begin{cases} 0 & (-\pi/2 \leq \theta \leq \pi/6) \\ \Psi_{max} \sin^2(3\theta - \pi/2)\,[1 - \exp(-\frac{t}{\tau})] \exp(-\frac{z_B}{2H}) & (\pi/6 \leq \theta \leq \pi/2) \end{cases}$$

For the standard case, the forced wave is a stationary wave ($c = 0$) with zonal wavenumber 1 whose amplitude is 200 gpm without horizontal phase tilt; this forcing is termed as *standard forcing.*

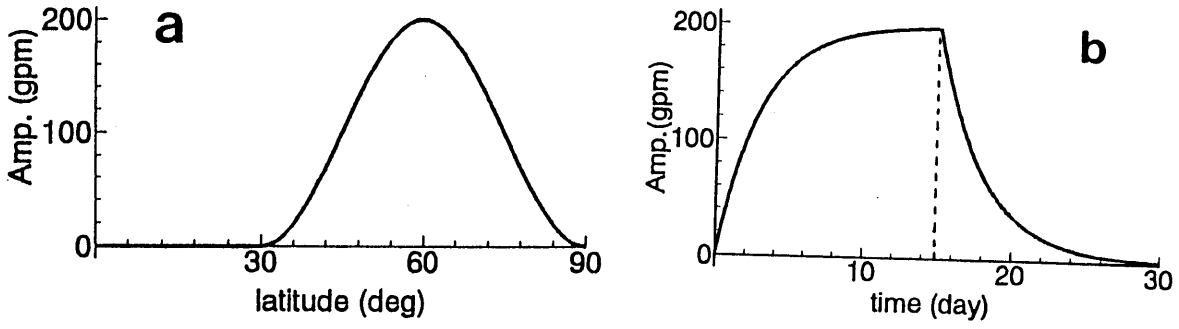

Fig.3.1: (a) latitudinal and (b) temporal variations of wave amplitude at the bottom boundary for a standard wave forcing.

3.1.2 Initial zonal-mean wind

The winds shown in Fig.2.2 are used for the experiments as initial winds in this section.

Looking at the zonal-mean winds in SH and NH in Fig.2.2, the stratospheric westerly jet in SH is significantly stronger than that in NH during wintertime. During late

winter to early spring in SH, the westerly in the highlatitude stratosphere is intensified and a separation of westerly jet occurs (*e.g.*, Shiotani and Hirota 1985).

3.1.3 Material transport and residual circulation

Ozone transports associated with planetary waves are calculated based on following mass conservation equation.

$$\frac{\partial \chi}{\partial t} = -\left[\frac{1}{a\cos\theta}\frac{\partial}{\partial \lambda}(\chi\, u) + \frac{1}{a\cos\theta}\frac{\partial}{\partial \theta}(\chi\, v\cos\theta) + \frac{1}{\rho_0}\frac{\partial}{\partial z}(\rho_0 \chi\, w)\right] \quad . \tag{3.1}$$

The initial distribution of ozone concentration, which is close to the monthly averaged distribution in June in SH, is shown in Fig.3.2. The ozone concentrations at the upper and lower boundaries are fixed at the initial values. Variation of total ozone contents is obtained by vertical integration of the zonally averaged ozone concentration which is products of zonal-mean mixing ratio and air density.

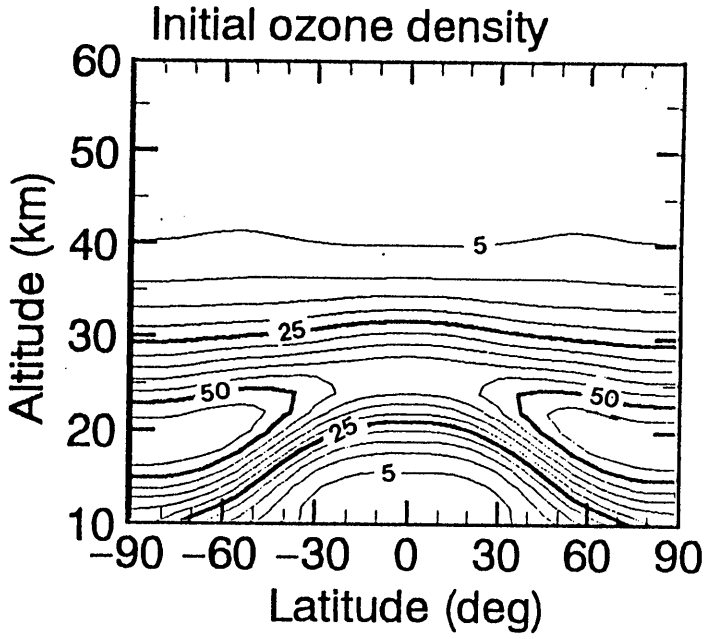

Fig.3.2: Initial distribution of ozone density in the meridional plane. Contour interval is 0.5×10^{12} molec m^{-3}. Left-hand side in the panel indicates Southern Hemisphere and right-hand side Northern hemisphere.

A meridional circulation related with material transport is approximately represented by residual circulation derived from TEM theory (Andrews and McIntyre 1976). Zonal mean meridional and vertical velocities of residual circulation, $(\overline{v}^*, \overline{w}^*)$, are defined as follows.

$$\overline{v}^* \equiv \overline{v} - \frac{1}{af\rho_0}\frac{\partial F_z}{\partial z} \quad , \tag{3.2}$$

$$\overline{w}^* \equiv \overline{w} + \frac{1}{a^2 f \rho_0 \cos\theta}\frac{\partial F_z}{\partial \theta} \quad , \tag{3.3}$$

where the meridional and vertical components of EP flux are

$$\mathbf{F} = (F_y, F_z) \equiv a\rho_0 \cos\theta \left(-\overline{u'v'} \ , \ \frac{f}{N^2} v' \overline{\frac{\partial \phi'}{\partial z}} \right) \quad . \tag{3.4}$$

A relationship between residual circulation and material transport will be discussed in Appendix C.

3.2 Dependency on initial zonal-mean wind

Dependency of meridional circulations on initial zonal-mean wind for the standard forcing is first examined. A planetary wave with wavenumber 1 and maximum amplitude of 200 gpm is forced commonly throughout a series of experiments in this section. The amplitude is closer to that of amplified planetary waves in SH rather than NH.

Residual circulations at day 15 in SH and NH are shown in Figs.3.3 and 3.4, respectively. All of the circulations are restricted below 40 km with an exception that a little part of circulation in July reaches the stratopause. Every circulation crosses the equator and originates at midlatitudes in the opposite hemisphere of the forcing. In the equatorial lower stratosphere, upward motions are predominant, whereas meridional motions become predominant with increasing height.

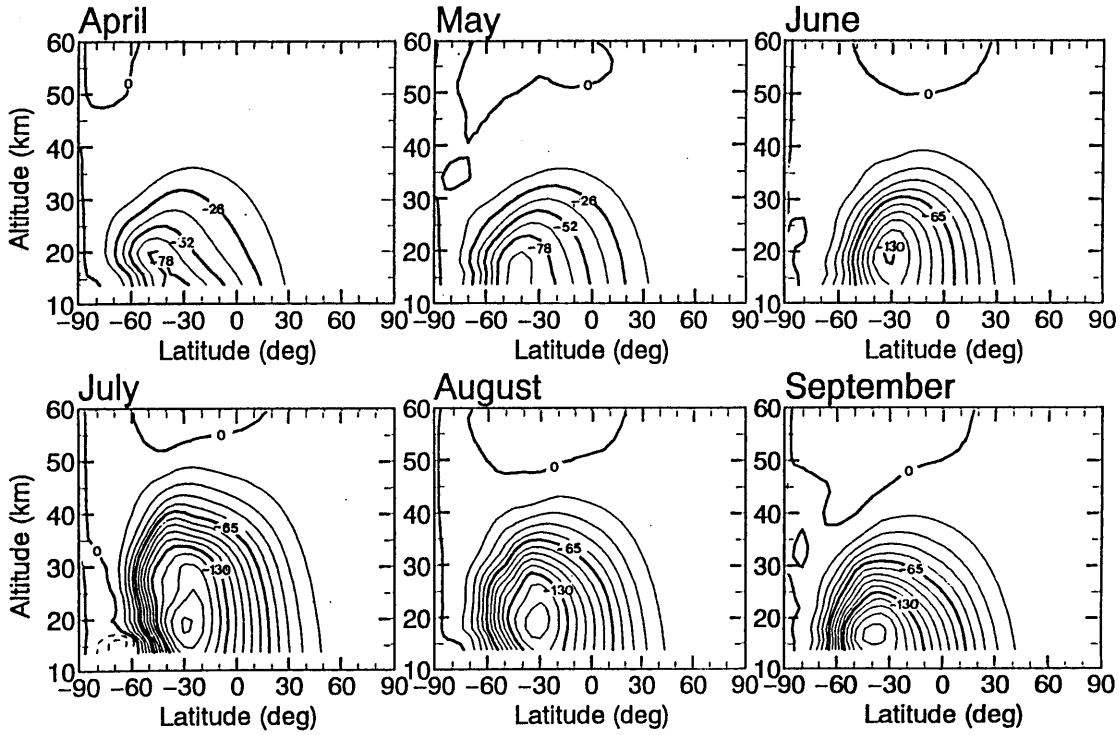

Fig.3.3: Stream functions at day 15 for standard wave forcing in SH from April to September. Contour interval is 13 $\mathrm{kg\,m^{-1}s^{-1}}$. Negative area is shaded.

In SH, intensity of the circulation develops as the season progresses. The circulations are weak in the late autumn (April and May in Fig.3.3). The circulations in midwinter (June and July in Fig.3.3) are intensified and the downward motions are concentrated around 35° S– 50° S. After midwinter, they extend to higher latitudes and

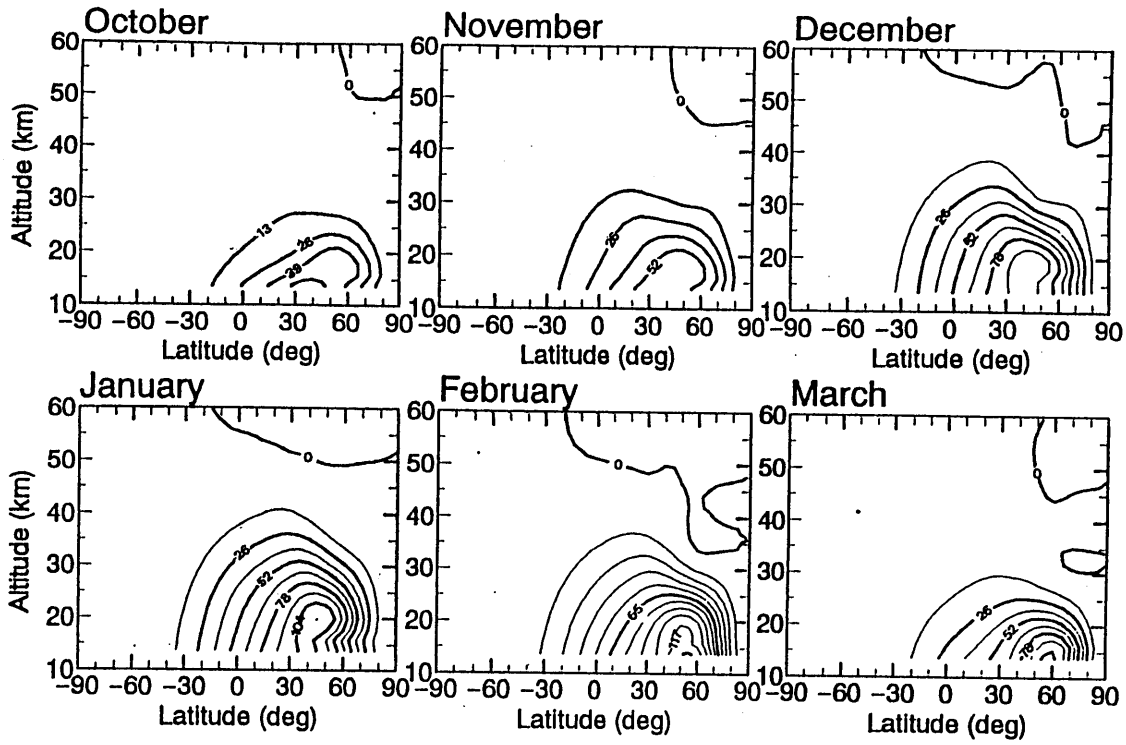

Fig.3.4: Same in Fig.3.3, but in NH from October to March.

the position of the downward motions shift poleward; ~55° for August and ~65° for September.

The intensification of the circulation in midwinter (June and July) is mainly caused by magnification of EP flux at the lower boundary. In our experiments, the wave amplitude at the lower boundary is the same in every calculation but EP flux is not the same because the magnitude of EP flux depends on the zonal-mean wind and its vertical shear at the lower boundary. Whereas, the intensification of meridional circulation in late winter (August and September) is associated with the poleward shift of the stratospheric westerly jet as discussed in next subsection. Equatorward propagation of planetary waves in late winter is suppressed by the poleward shift of the jet axis. The suppression causes the amplification of wave amplitude and intensification of the circulation in highlatitudes compared with those before June.

The induced circulations in NH (Fig.3.4) extend to higher latitude than those in SH and regions of the downward motions in the lower stratosphere shifts poleward as the season progresses from midwinter and confined in higher latitudes than 60° N in February and March. The zonal-mean winds in highlatitudes in those months are weakened and minor warming takes place. The concentration of the downward motion in the polar region is consistent with theoretical studies by Matsuno and Nakamura (1979) and Rood and Schoeberl (1983).

Intensity of the residual circulations in NH is relatively weaker than that in SH for corresponding months. EP flux at the lower boundary in NH is smaller than that in SH ($\sim$ 2/3 for the corresponding month) because of the weak vertical shear in the lower stratosphere. As residual circulation is driven by convergence of EP flux, intensity of the circulation is also weaker in NH than in SH.

Deviations of the total ozone content from the initial values are shown in Figs.3.5 and 3.6 for SH and NH, respectively. The ozone maxima in SH are formed in mid-latitudes except for the case of April (Fig.3.5). The location of the maxima shifts equatorward during midwinter and reaches 40° S in June. Then it gradually shifts poleward during early spring and reaches 60° S in September. The total ozone content largely increases in late winter and early spring, whose value exceeds 20 DU. It hardly increases in polar region during June to August. In particular, the total ozone content in July actually decreases in the polar region. The total ozone content in lower latitudes than 30° decreases every month.

The location of maximum ozone increase and poleward shifts in early spring correspond to the latitude of concentrated downward motion (compare Fig.3.5 with Fig.3.3). The poleward shift of the location is well correlated with the observed characteristics of the subpolar maximum in SH as shown in Fig.3.5. The total ozone content in subpolar maximum is comparable with the monthly increasing rate obtained by observation; the calculated increasing rate is about 15 DU a month in early winter and 25 DU a month in late winter whereas the observed one is about 20 DU. This suggests that seasonal change of the subpolar maximum is controlled by the planetary wave amplification.

The experiments of standard forcing, however, do not simulate a minimum of the planetary wave amplitude in midwinter. The calculated maximum amplitude at day 15 are about 630 m in April, 720 m in May, 830 m in June, 1120 m in July, 1360 m in August, and 1300 m in September. The reason of discrepancy in seasonal evolution of the wave activity is resulted from adopted simple boundary conditions in this experiment. Consequently, calculated amount of ozone variation contains ambiguity for the quantitative comparison of the observed variation.

The maximum increase of total ozone content in NH is formed at the pole (Fig.3.6). The polar maximum is enhanced as the season progresses from midwinter. The amount of ozone increases in February and March exceeds 26 DU. As mentioned previously, minor warmings take place in those months. Remarkable increase of the ozone during warming event has been captured in observations (*e.g.*, Geller and Wu 1987). However, the amount of increase is less than that of observation, which is resulted from weaker amplification of the forced planetary waves than observed one in NH. Dependency of the forcing amplitude will be examined in Section 3.4.

A series of experiment, using climatological zonal-mean winds in SH and NH as initial values, extracts a different role of the planetary wave amplification on meridional circulation and ozone distribution between NH and SH. In NH winter, the induced circulation extends to highlatitudes which results in the increase of ozone content in the polar region throughout late autumn to early spring. In SH winter, however, the induced downward motion concentrates in midlatitudes and enhances the subpolar ozone maximum in midlatitudes.

The ozone concentration is primarily increased below 35 km in midlatitudes and/or highlatitudes. The timescale of photochemical reaction associated with HO_x chemistry (Hou et al. 1991) is about 100 days at 30km and 300 days at 20 km. Consequently, the temporal variation of ozone content may not be significantly modified by inclusion of the photochemical reaction in a short-range calculation in each month.

Same initial ozone distribution is adopted here, although the observed monthly mean ozone distribution is different between NH and SH and varies seasonally. This experimental condition causes ambiguity in amount of calculated ozone variation but does not change qualitative characteristics of latitudinal ozone variations. The latitude

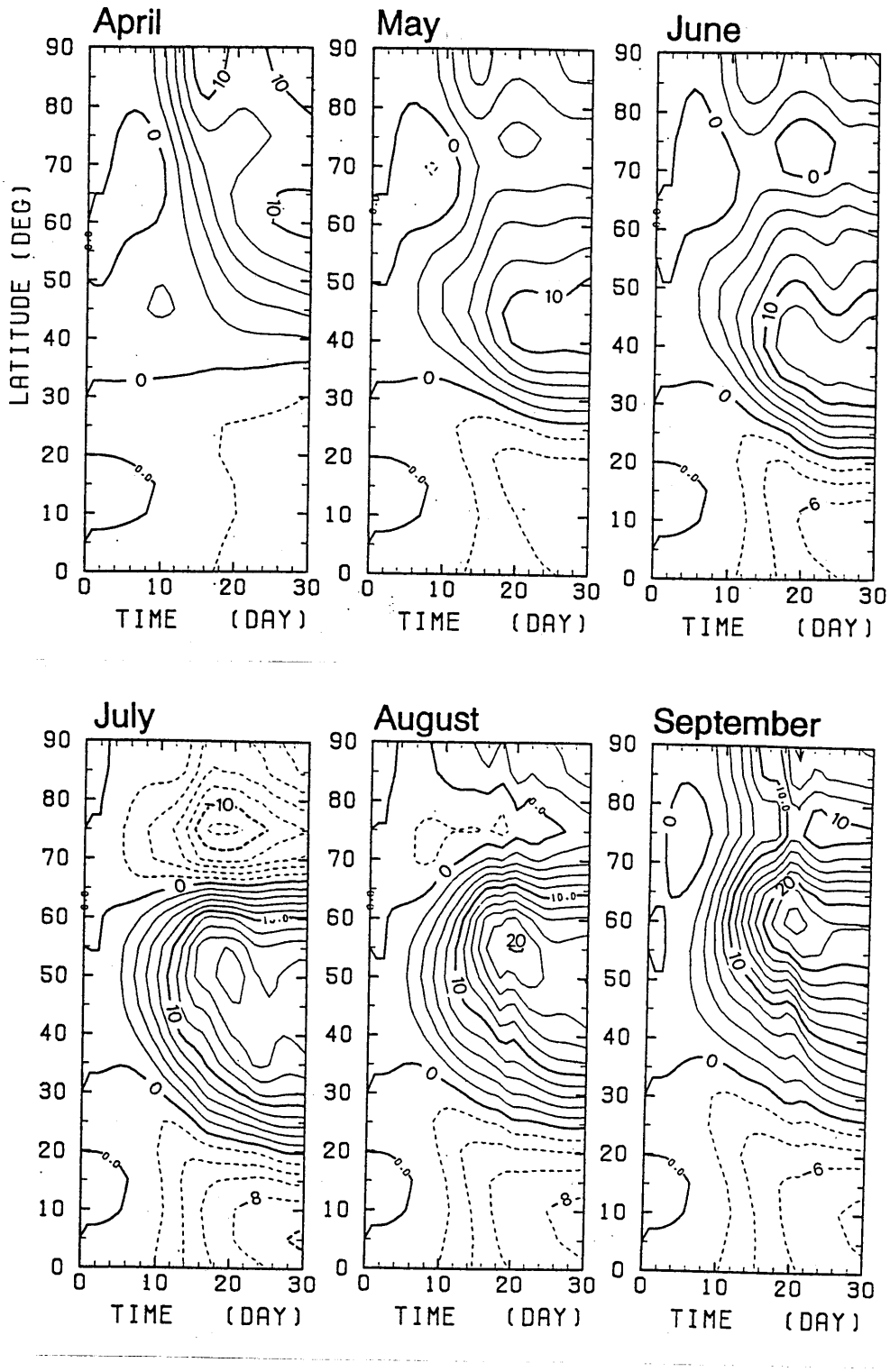

Fig.3.5: Deviation of ozone content from its initial value in SH from April to September. Contour interval is 2 DU.

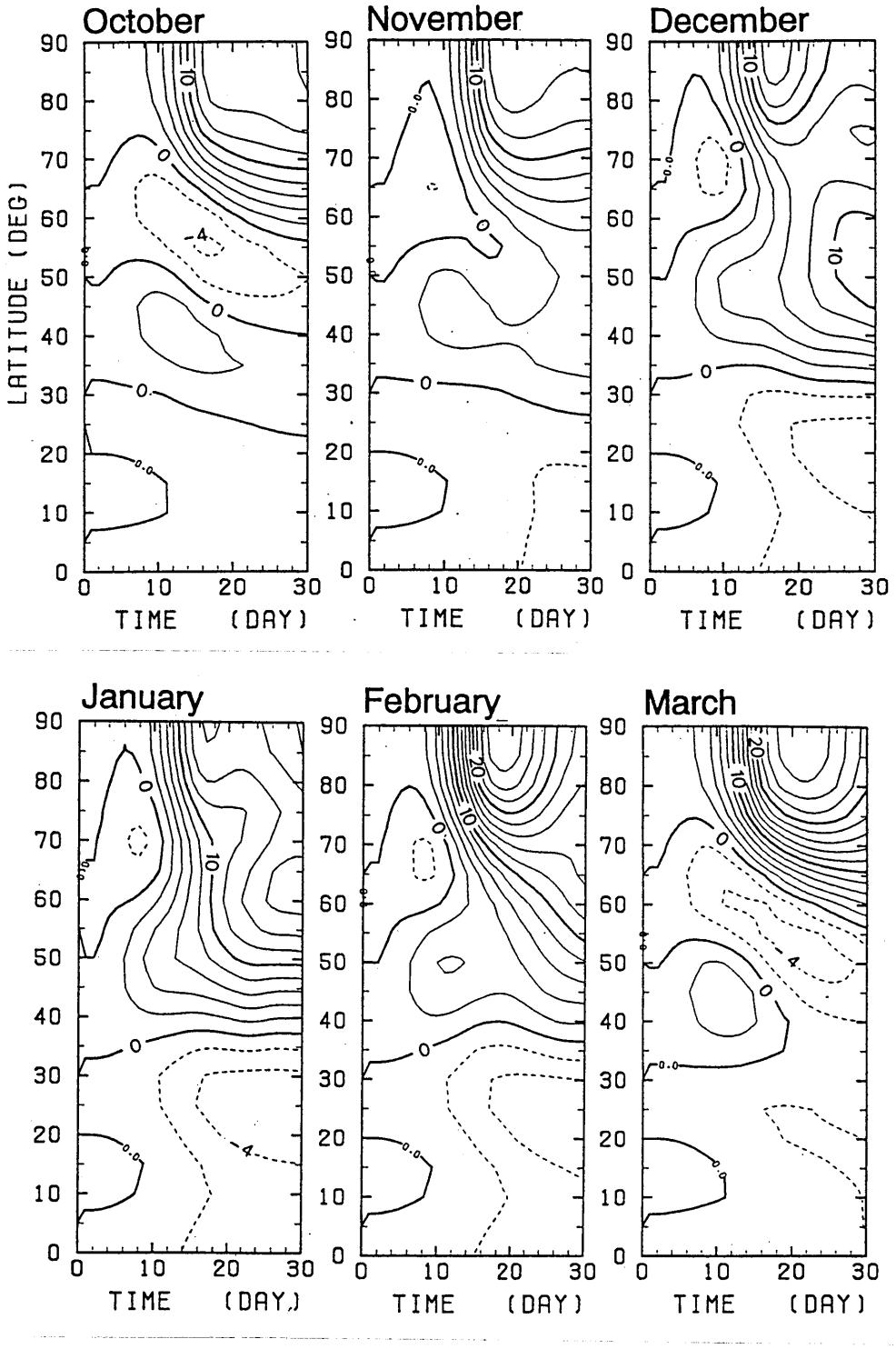

Fig.3.6: Same in Fig.3.5, but in NH from October to March.

of ozone increase corresponds to that of downward motion because of the monotonous increase of ozone mixing ratio below 40 km in midlatitudes and highlatitudes. Observed ozone mixing ratio maintains the monotonous increase below 40 km through a winter season (e.g., Krueger et al., 1973). Hence, the calculated latitudinal variation of ozone may have similar characteristics with those using a variable initial ozone distribution.

3.3 Diagnosis of the residual circulation

For only the cases of July in SH and January in NH, the time evolution of the meridional circulation is examined and diagnostics how the difference of circulation arises depending on the initial zonal-mean wind. These two months for interhemispheric comparison are adopted for experiments because the contrast in ozone distribution between SH and NH is most clear.

Figure 3.7 shows the time evolution of the residual circulation in July in SH and in January in NH. During growing phase of the planetary waves both in July and January (day 9 in Figs.3.7a,b), the meridional circulations reach near to the pole. As seen in Figs.3.3 and 3.4, the position of downward motion in the lower stratosphere shifts equatorward in SH but keeps in the polar region in NH. Weak upward motion appears in the polar region in the SH lower stratosphere (day 15 in Fig.3.3) and is intensified just after the wave forcing is removed (day 18 in Fig.3.7a), which causes ozone decrease in polar region. The weak upward motion is also induced in the NH polar stratosphere at day 18 although the intensity is very weak. The intensified circulation is kept for a while in SH but in NH it rapidly decays (day 27).

The zonal-mean wind and refractive index squared for wavenumber 1 at day 12, and EP flux of wavenumber 1 and its divergence at day 15 are shown in Fig.3.8. The refractive index squared (hereafter termed as refractive index) for a stationary wave with wavenumber k is defined

$$Q_k \equiv \frac{a}{\overline{u}}\frac{\partial \overline{q}}{\partial \theta} - \frac{k^2}{\cos^2\theta} - \frac{f^2}{N^2}\frac{a^2}{4H^2} \quad . \tag{3.5}$$

In the case of July in SH (Fig.3.8a), the westerly jet in the upper stratosphere is slightly decelerated by the intrusion of planetary waves. A maximum line (a ridge) of the refractive index extends from the midlatitude lower stratosphere to the subtropical upper stratosphere. The EP flux vector, which represents the direction of wave propagation, in the lower stratosphere is oriented upward with a little tilt toward the equator. The direction of the vectors gradually changes equatorward with increase of height. Inspecting these characteristics of the refractive index and EP flux, the planetary wave is likely to propagate along the maximum line of the refractive index in the stratosphere as expected by WKB theory. The equatorward propagation of the wave shifts the convergence region of EP flux to subtropics. As a result of this, a strong convergence region of EP flux is located in the subtropical middle stratosphere while a divergence region is located in the midlatitude lower stratosphere. The EP flux convergence induces the poleward meridional flow. In turn, the equatorward acceleration of the meridional flow due to the EP flux divergence in highlatitude prevents a poleward extension of the meridional flow, which results in formation of downward flow in midlatitudes.

At the decaying stage of the forced wave, the tail of the wave packet accelerates the zonal-mean wind and drives the equatorward flow. As a result, the upward motion is induced in the polar lower stratosphere.

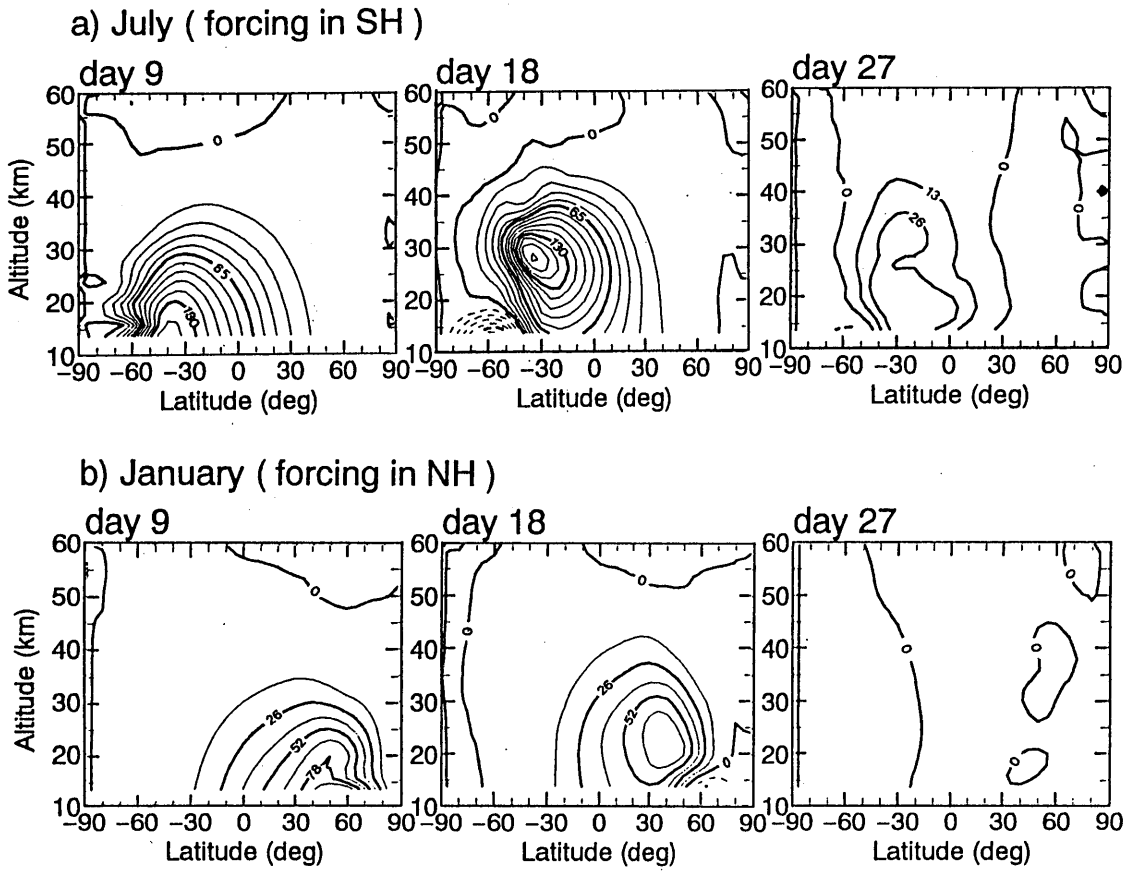

Fig.3.7: Evolution of stream functions in the case of July with standard forcing in SH (a) and in the case of January with forcing in NH (b). Contour interval is $13\,\mathrm{kg\,m^{-1}s^{-1}}$.

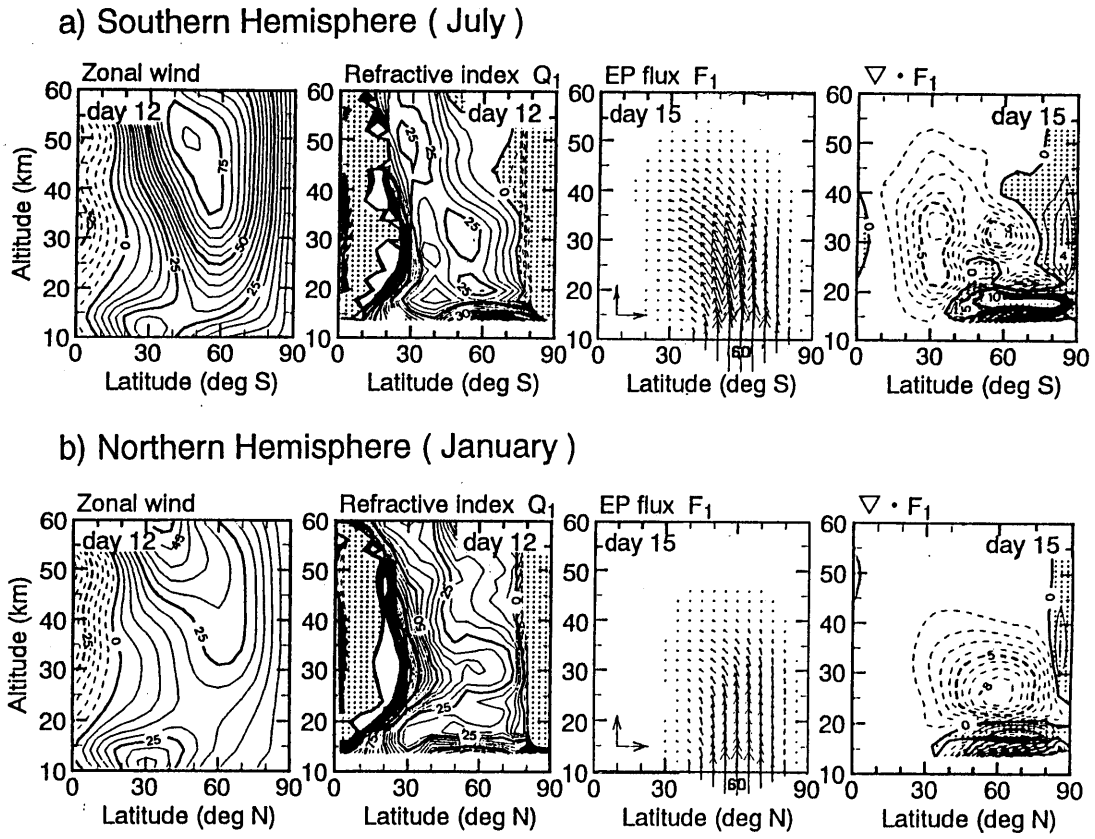

Fig.3.8: Mean zonal wind ($m\,s^{-1}$) at day 12, squared refractive index for wavenumber 1 (non-dimensional) at day 12, (c) EP flux for wavenumber 1 at day 15, and its divergence ($10\ m\,s^{-1}day^{-1}$) at day 15. Upper panels (a) show SH in the case of July with standard forcing and lower panels (b) show NH in the case of January. Negative regions in the refractive index are shaded. The meridional arrow at left bottom corner in the panels of EP flux represents a value of F_y equal to 1.2×10^8 kg s^{-2} and the vertical arrow a value of F_z equal to 5.2×10^5 kg s^{-2}.

In the case of January in NH (Fig.3.8b), the westerly wind in the stratosphere is substantially decelerated from its initial zonal-mean wind. There is no significant maximum line of refractive index in the stratosphere. EP flux vectors gradually change from upward direction to equatorward direction through the wave propagation. The tilt of vector, however, is much smaller, and the intrusion of planetary waves into the subtropical region is also weaker than the case of July in SH. Consequently, the convergence region of the EP flux appears in higher latitude than that in the case of July.

The refractive index and EP flux for wavenumber 1 after midwinter in SH are shown in Fig.3.9. The refractive index field in June is relatively homogeneous in the middle stratosphere than other months. For the index fields after July, maximum regions (ridge) are formed at 50-60°S below the middle stratosphere. The maximum region in July tilts equatorward with altitudes. In August and September, clearer ridges without equatorward tilt are formed along the highlatitude jet axis (Fig.2.2). The maximum region is most emphasized in September. The refractive indexes in the upper stratosphere and lower mesosphere in highlatitudes have negative value in June and September, and small positive value in July and August. Negative regions exist also in lowlatitudes and expand into subtropics in early spring.

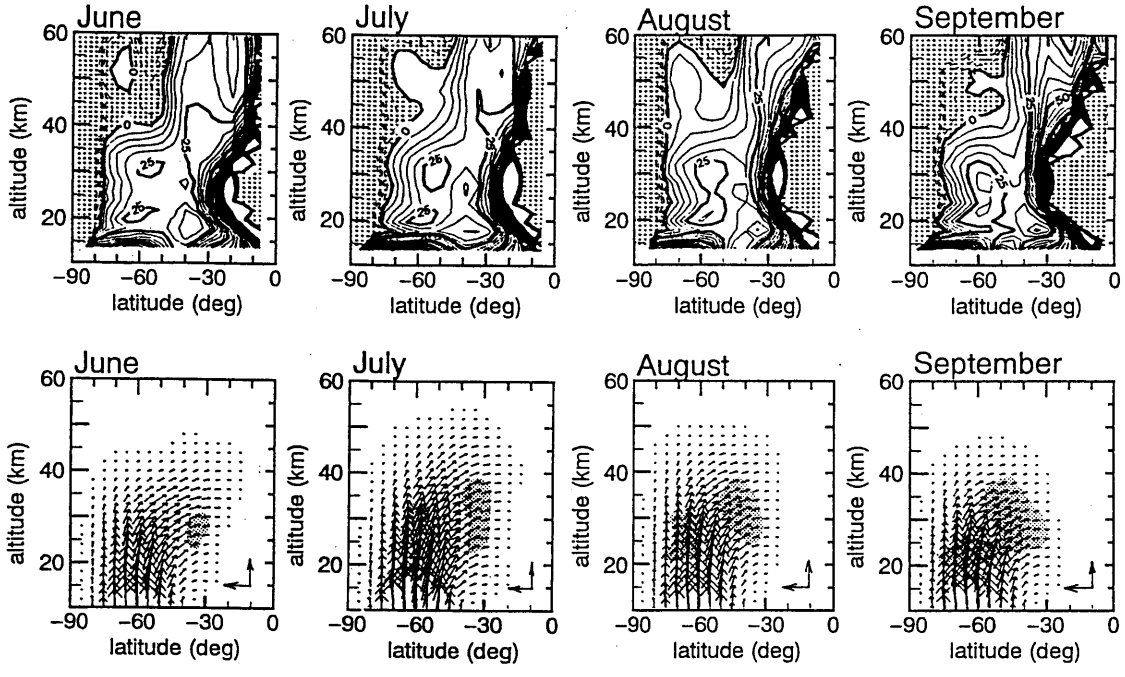

Fig.3.9: Squared refractive index and EP flux for wavenumber 1 in SH from June to September. Upper panels show the refractive index at day 10 and lower panels do EP flux at day 15. Negative regions in the refractive index are shaded. The meridional and vertical arrows at right bottom corner in the lower panels represent a magnitude of EP flux which is the same as in Fig.3.8. Convergence regions of EP flux having a grater value than 3 kg $m^{-1}s^{-2}$ are shaded.

Upward propagation in the lower stratosphere and equatorward refraction in the middle stratospheres are common features for the wavenumber 1 during June to September (lower panels in Fig.3.9). However, the convergence regions of the EP flux, which are indicated by shade, are located in different position depending on the way of the refraction of the flux. EP flux in June changes its direction toward equator in the middle stratosphere and a core of the convergence region is formed at the subtropical region. Little flux intrudes into the highlatitude upper stratosphere because of the negative refractive index there. Equatorward refraction of the flux in July occurs more gradually than that in June and the wave propagates into the upper stratosphere. The planetary wave is likely to propagate along the ridge of the index field as discussed in this subsection. Accordingly, the convergence region is distributed in broader altitudes around 30°S.

There are two cores of the convergence region in August and September; one is located at the highlatitude lower stratosphere and the other is at the midlatitude middle stratosphere. The highlatitude convergence region is formed by the upward propagation of the wave along the clear ridge of the refractive index. The midlatitude one is located around 45°, i.e., 15° poleward than that in July. It is considered that the poleward shift of the subtropical convergence region is associated with both the expansion of the negative index field in lowlatitudes and the small equatorward refraction in the lower stratosphere. Formation of the highlatitude convergence region and poleward shift of the midlatitude one result in the poleward movement of the downward motion of the meridional circulation (Fig.3.3).

3.4 Ozone variation for different wave forcing

The induced meridional circulation and resulting ozone variation depend on the amplitude, wavenumber and phase velocity of the forced planetary waves. To examine the dependency, parameters of the forced wave (*e.g.,* wave amplitude) are replaced from the standard forcing. Figure 3.10 shows the deviations of total ozone content from its initial values in the cases of July in SH and January in NH.

The variation of total ozone content caused by the wave forcing with wavenumber 2 whose amplitude is 200 gpm is shown in Figs.3.10a,d. The ozone variation in the case of July (Fig.3.10a) is basically similar to that in the case of standard forcing. In the case of January, however, wavenumber 2 forcing enhances the ozone increase in midlatitude and slightly weakens increase in polar region (Fig.3.10d) compared with standard forcing. Planetary waves with wavenumber 2 propagates more equatorward than that with wavenumber 1, which causes the enhancement of midlatitude maximum.

Wave forcing is usually stronger in NH than in SH (*e.g.*, Shiotani and Hirota 1985). Here, the forcing amplitude of wavenumber 1 is set as 100 gpm in SH and as 300 gpm in NH. The variation of ozone content are shown in Figs.3.10b,e. In the case of weak forcing in SH, the peak of ozone increase is formed at 40 ° S but the amount of increased ozone content is considerably smaller than that for the standard forcing. Also, the ozone decrease in highlatitude does not appear in this case.

The strong forcing in January in NH, in turn, leads to a remarkable increase of ozone content in the polar region, whose amount reaches 58 DU at day 24. In this case, stratospheric major warming takes place around day 18. As mentioned in Section 3.2, the downward motion is intensified at the polar region during the sudden warming, and total ozone content drastically increases.

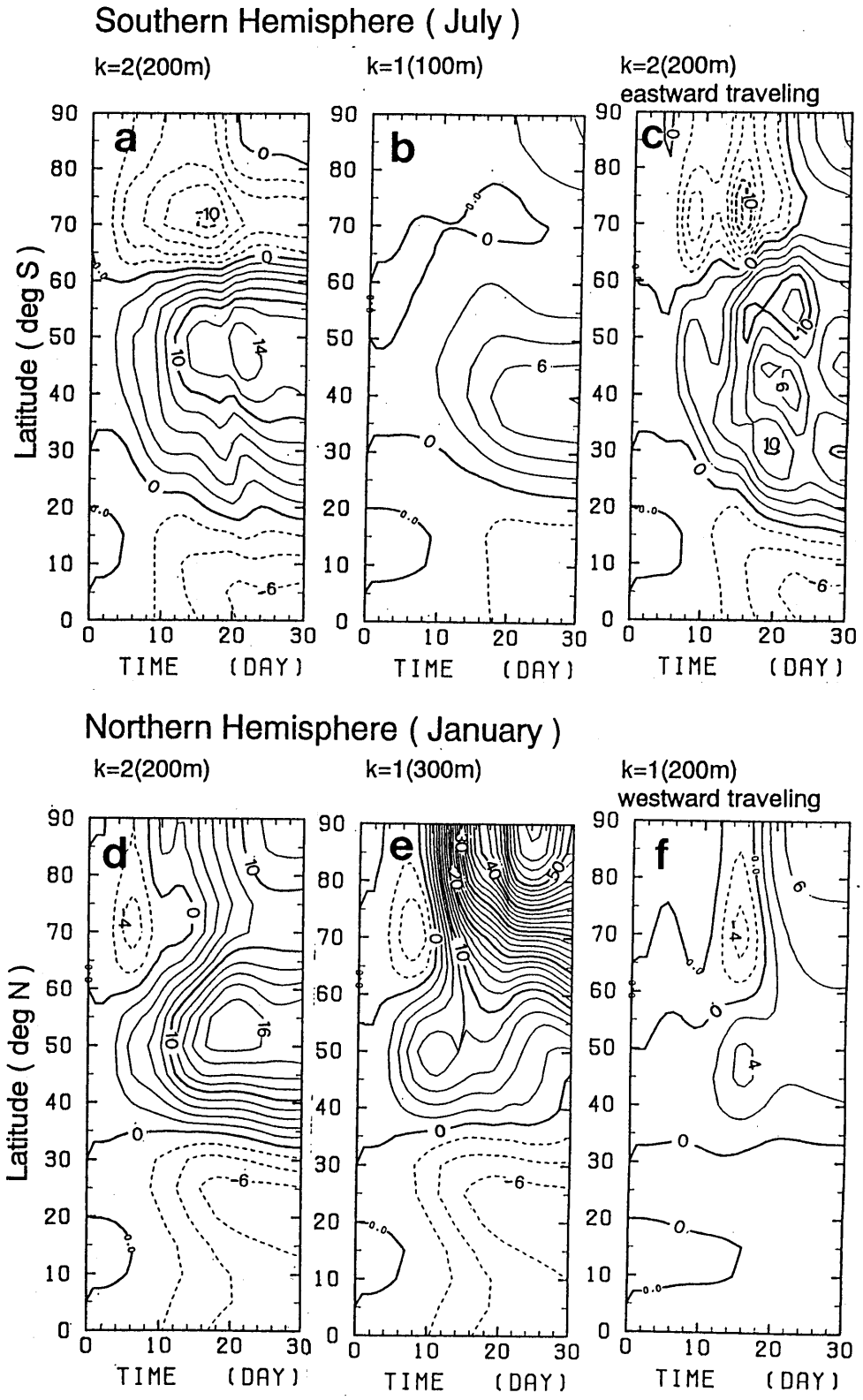

Fig.3.10: Deviation of ozone content from its initial value for various wave forcings (see text). The upper panels (a~c) show that in the case of July in SH and the lower panels (d~f) show that of January in NH. Contour intervals are 2 DU.

The observation shows that an eastward traveling wave with wavenumber 2 is frequently amplified during winter and early spring (*e.g.*, Shiotani *et al.* 1990, Manney *et al.* 1991). When an eastward traveling wave with wavenumber 2, whose period is 20 days and amplitude is 200 gpm, is forced in SH, the result is shown in Fig.3.10c. Increase in midlatitudes and decrease in highlatitudes of total ozone content occur until day 15 in a similar way as standard forcing. The ozone distribution in midlatitude, however, is noisy and that in highlatitude is increased from day 16.

The westward traveling waves are common in NH winter. Fig.3.10f shows the distribution of total ozone content when a westward traveling wave with wavenumber 1 and 40 day period is forced. The increasing region in midlatitude and decreasing region in highlatitude formed at the end of amplification stage, but the deviation is very small. Fast westward traveling wave hardly propagates into the highlatitude stratosphere and the induced circulation is weak.

Ozone distribution to other forcing are also examined (not shown here). When the duration period of amplification is taken to be 20 days (5 days longer than the standard forcing), the maximum of ozone increase in midlatitude in SH and the polar maximum in NH are intensified about 50% . When the planetary waves with wavenumbers 1 and 2 coexist in SH, the ozone maximum is formed about at 55° S, which is located 5° poleward than that in the case of standard forcing.

The characteristics of latitudinal distribution of ozone variation, *i.e.*, increases in midlatitude for SH and in polar region for NH, are basically maintained for the various wave forcing as presented in this section. Interhemispheric asymmetry of the total ozone content is considerably depending on the forcing and is most typical when the stationary wave with wavenumber 1 is forced. The amounts of ozone variation in SH are comparable with the observed ozone increase within a month, when the amplitude of forced waves is 200 gpm at the tropopause level. In NH, the forced planetary wave with 300 gpm causes the reasonable ozone increase at the north pole compared with observations.

3.5 Summary and discussion

A series of experiments by a spherical semi-spectral model shows that planetary waves play different roles for the formation of meridional circulation and the latitudinal distribution of total ozone content between SH and NH. The planetary waves in SH enhance the subpolar ozone maximum and make realistic seasonal movement of the latitudinal location of the subpolar maximum, whereas, in NH, they transport ozone to the polar region and produce the ozone maximum region at the pole.

The amount of increased total ozone content by planetary wave amplification depends on the amplitude of the forced wave. The interhemispheric asymmetry of the ozone distribution is achieved for various wave forcing, and typical asymmetry appears when the stationary wave with wavenumber 1 is applied. When the stationary wave with wavenumber 1 having the amplitude of 200 gpm is applied at the tropopause level, the increased amount throughout an event of wave amplification is comparable with the observed monthly increase around the subpolar ozone maximum in SH. The increase of total ozone content in the north polar region is most predominant when stratospheric sudden warmings take place. They occur in midwinter and early spring, when planetary waves are strongly amplified.

The seasonal variation of latitudinal distribution of ozone content due to planetary

waves discussed by linking the short-range ozone variation. The calculated variation of total ozone content exhibits similar characteristics with observations. Total ozone content in SH winter increases mostly in midlatitudes around 40° -50° while that in NH winter increases in the polar region. In SH, the location of midlatitude peak of ozone increase shifts poleward as the season progresses from midwinter to early spring. This seasonal variation of total ozone content highly depends on the meridional circulation induced by planetary waves. Covariance of the calculated ozone variations with observations suggests that the seasonal variation of the subpolar maximum is controlled by the planetary wave amplification.

In SH winter, the circulation does not reach the polar region and its downward motion is concentrated in midlatitudes. The location of downward motion shifts to higher latitude as the season progresses from midwinter to early spring. While in NH during late autumn to early spring, the circulation extends to highlatitudes and the downward motion is broadly distributed from midlatitudes to highlatitudes.

It is also found that the upward motion appears in the polar region in SH just after the wave forcing turns off and lasts for a while. The upward motion results in the ozone depletion in the polar region and enhances the midlatitude maximum.

The difference of the meridional circulation depends on the structure of initial zonal-mean wind in each hemisphere. The zonal-mean wind in SH midwinter (before the formation of highlatitude jet) forms equatorward tilt of refractive index and then prevents the propagation of planetary waves to higher latitude. Whereas, planetary waves in NH propagate into the weaker jet in the highlatitude stratosphere. The difference of the zonal-mean wind causes the asymmetry in convergence region of EP flux and location of downward motion. The poleward shift of the downward motion in SH late winter is caused by the poleward movement of convergence region of EP flux and formation of the convergence region in highlatitudes. It is indicated that these seasonal variations correspond to the change of the wave propagation field (i.e., refractive index filed).

Calculated amount of ozone variation in SH due to an amplification of the planetary wave is comparable with the observed one: both are about 20 DU a month in midlatitudes during wintertime. The coincidence of the variation indicates that planetary waves have substantial roles to form the subpolar maximum in SH. This experiment, however, has uncertainty to evaluate quantitative comparison with the observation. Our experiments did not reproduce the observed midwinter minimum of planetary wave amplitude in SH. The magnitude of EP flux in the experiments was larger in midwinter than that in early winter because of the strong vertical shear of the zonal-mean wind in the lower stratosphere. More realistic wave forcing must be used for the accurate quantitative comparison of the ozone variation. Monthly averaged ozone distribution in June as initial values for all months is used. This artificial condition also causes ambiguity for the amount of increased ozone although it does not change the latitudinal characteristics of the ozone variation.

Since objective of the present study is to reveal a role of planetary wave amplification on the formation of the ozone distribution, effects of gravity waves, tropospheric forcing due to cumulus convections which drives Hadley circulation in the equatorial region, and chemical reactions were omitted through the experiments. It is considered that tropospheric forcing and chemical reaction play essential roles for the symmetric ozone distribution but do not contribute substantially to the formation of the asymmetry. On the other hand, interhemispheric asymmetry of gravity wave activity may

cause the asymmetry of the ozone distribution as well as planetary wave activity. Gravity wave breaking induces a poleward circulations in the lower stratosphere (Tanaka and Yamanaka 1985, Tanaka 1986). Evidencce of the existence of saturated gravity wave has been presented by many obsevation; Ushimaru and Tanaka (1990) shows the saturated internal inertial gravity waves are constantly observed just above the tropopause from MU radar observatin with about 1 month priod. The meridional circulations are enhanced more in NH than in SH because of the predominance of gravity wave activity in NH. However, the quantitative study of the circulation driven by the gravity waves has not been progressed due to lack of knowledge about the climatological distribution of the gravity wave activity.

4 Effects of traveling wave 2 in ozone distribution

In the previous section, the basic roles of planetary waves on the latitudinal distribution of zonally averaged total ozone content with 1 month time scale were explored. This section shows that a more realistic variation of the horizontal distribution of total ozone content by adding the interaction with an eastward traveling wave with wavenumber 2.

As discussed in Introduction, the horizontal distribution of the total ozone content in SH varies with time scale of a few tens of days. The variation is characterized by quasi-periodic growth of the wave-1 like ozone-rich region. This is expected to be a reflection of planetary wave amplification through the nonlinear interactions with wavenumber 2. Analysis by HKS (1990) suggested that the amplification of wave 1 may be caused by eastward traveling wave, which frequently exists during winter and early spring in SH (e.g. Hartmann, 1976).

4.1 Configuration of experiments

Model used in this section is the same as described in the previous section. Ozone chemistry is neglected in this experiment and the initial condition of the ozone density is the same as Fig.3.2. The difference is only planetary waves forced at lower boundary. It is assumed that stationary wave 1 and traveling wave 2 are forced at the tropopause level and their amplitudes are kept constant after a short initial transient period. Amplification of the wave 1 in this case occurs in the stratosphere through the interaction with wave 2 expect for during the transient period.

By making use of changes in the geopotential height, waves with wavenumbers 1 and 2 are forced at the lower boundary (10km). The maximum forcings are located at the latitude of 60° S, and is gradually increased over about 3 days and then kept constant. Both waves have no phase tilt in the horizontal plane at the bottom boundary. The function forms of the geopotential forcing at the bottom boundary are written as

- Wave 1

$$\Psi_1 = \begin{cases} \mid \Psi_1 \mid (1 - e^{-\frac{t}{\tau_s}}) \sin^2(3\theta - \frac{\pi}{2}) & -\frac{\pi}{2} \leq \theta \leq -\frac{\pi}{6} \\ 0 & -\frac{\pi}{6} \leq \theta \leq \frac{\pi}{2}, \end{cases}$$

• Wave 2

$$\Psi_2 = \begin{cases} |\Psi_2|\,(1-e^{-\frac{t}{\tau_s}})\,\sin^2(3\theta-\frac{\pi}{2}) & \\ \qquad [\cos(2\pi t/\tau_2) - i\,\sin(2\pi t/\tau_2)] & -\frac{\pi}{2} \le \theta \le -\frac{\pi}{6}\ , \\ 0 & -\frac{\pi}{6} \le \theta \le \frac{\pi}{2}\ , \end{cases}$$

where $|\Psi_1|$ and $|\Psi_2|$ are the forcing amplitudes of wave 1 and wave 2, respectively. τ_2 is the oscillation period of wave 2 and τ_s the growing time factor of the waves with a value of 3 days. The amplitude of the waves at the lower boundary is constant after the initial transient period. This assumption of constant amplitude of the waves at the lower boundary is idealized. The wave amplitudes more or less vary temporary at the tropopause level in the real atmosphere.

Geopotential heights of the waves with wavenumbers 1 and 2 are both 100 m at the lower boundary ($|\Psi_1|/g = |\Psi_2|/g = 100$ m). The oscillation period of eastward traveling wave with wavenumber 2 is 20 days. The initial zonal-mean wind used in this experiment is the climatological zonal wind in August (Fig.2.2).

4.2 Results and discussion

The polar stereographs of the total ozone content are shown in Fig.4.1. At day 21 (Fig.4.1a), the region with the ozone content exceeding 400 DU (ozone-rich region) has the structure of wave 2; the cores are located at 25° E and 180° E/W. Longitude in the model is arbitrary. The longitude (λ) in Fig.4.1 corresponds to the geopotential forcing giving "$-\sin\lambda$" for the stationary wave 1 at lower boundary. At day 24 (Fig.4.1b), the ozone-rich region around 70° E expands while the region around 150° W shrinks. The ozone content at 65° E exceeds 450 DU. The ozone rich region in the Western Hemisphere continues to reduce its area. The area of ozone-rich region in Eastern Hemisphere becomes largest at day 27 and gradually shrinks after then. The total ozone content at the center of the ozone-rich region reaches near 500DU at days 27 and 30. The structure is moving eastward, whose speed is about 15° day^{-1} during days 21-24 and about 10° day^{-1} during days 27-30.

The characteristics of the horizontal distribution and its temporal variation of total ozone content is quite similar to the observed distribution, especially during 6th to 15th in August in 1988 (see Fig.1.2) except for the polar region. The total ozone content in higher latitude than 70° observed by NIMBUS 7 is less than 300 DU but the calculated value exceeds 400 DU. This disagreement depends on the initial ozone concentration based on the climate value in NH. The seasonally averaged total ozone content during winter in NH is about 400 DU. On the other hand, the ozone content in SH is about 300 DU in August (Fig.1.1).

The similarity between observation and the present experiments suggests that quasi-periodic expansion of the ozone-rich region can be understood in the framework of the amplification of planetary wave with wavenumber 1 through the interaction with eastward traveling planetary wave with wavenumber 2.

Fig.4.2 shows the deviation of zonally averaged total ozone content from its initial value. The major increase of the total ozone content occurs in midlatitudes around 60° S. The characteristics of ozone increase is basically similar to the case of wave 1 amplification in August and September shown in the previous section (Fig.3.5) although

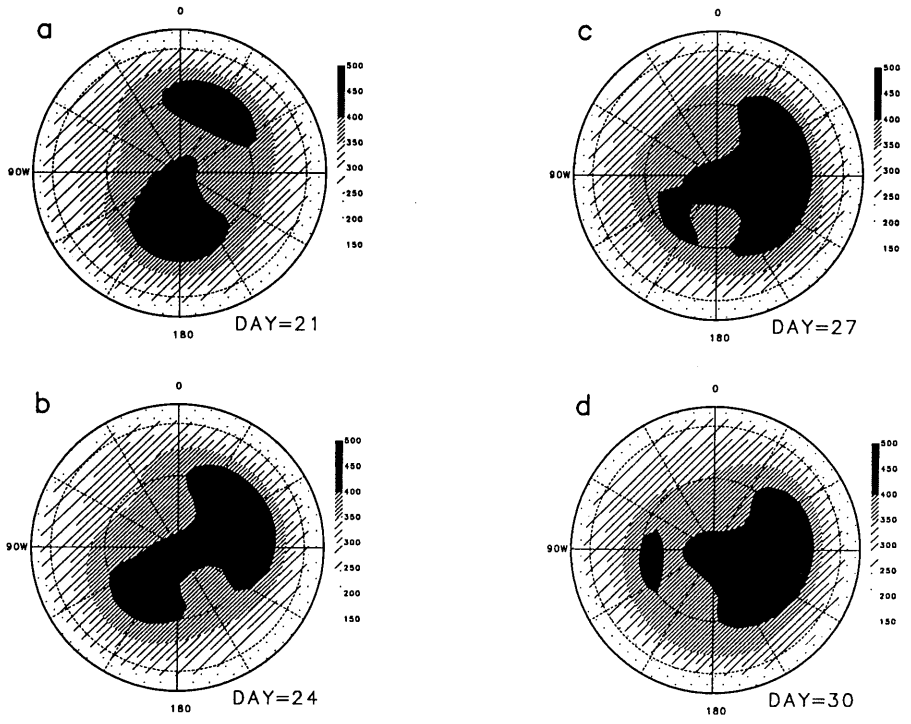

Fig.4.1: Total ozone distributions at model days 21, 24, 27, and 30. The center of the circle is south pole and the fringe is equator.

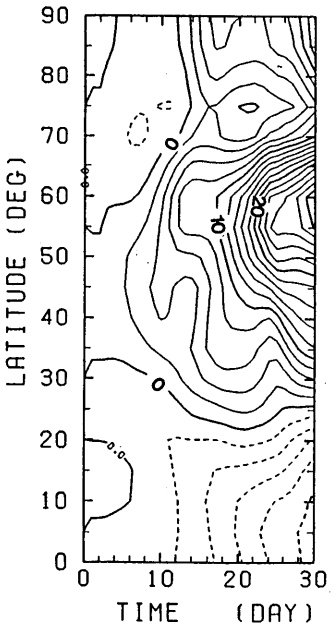

Fig.4.2: Deviation of ozone content from its initial value in August Contour interval is 2 DU. Dashed line means negative contour.

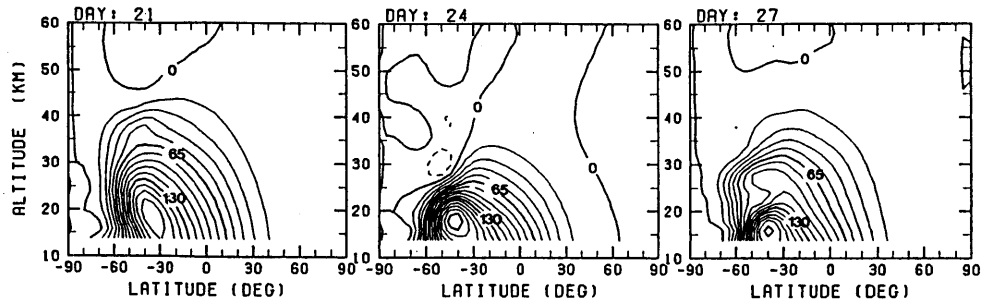

Fig.4.3: Mass stream function at days 18, 24, 30.

the mechanism of the amplification is quite different. This suggests that amplification of wave 1 enhances the subpolar maximum of total ozone content independently on mechanism of the amplification.

Fig.4.3 shows the residual circulation at days 21, 24, and 27 obtained from this experiment. The downward motion is significantly enhanced in the lower stratosphere at day 24. The period during days 21-27 is an expansion stage of the ozone-rich region (i.e., amplification stage of planetary wave with wavenumber 1). The downward flow in the midlatitude stratosphere is intensified during this period. The ozone content at 55° (Fig.4.2) remarkably increases due to the enhanced downward flow (Fig.4.3).

Planetary wave with wavenumber 1 is extraordinaly amplified when eastward travelling wave with wavenumber 2 is additionally enforced from the troposphere. In the case that no eastward travelling wave is incorporated, 200 m of geopotential height is necessary to be put at the lower boundary, in order to obtain reasonable values of total ozone concentration. Incorporation of eastward travelling wave leads to wave-wave interaction between the two waves (as will be described in Section 5 in detail) and associated enormous amplification of the planetary wave with wavenumber 1. Wave 1 reaches almost the same order of amplitude as that given in Section 3 even if enforced geopotential height is only 100m at the tropopause. Both cases have the same kind of effects to form the subpolar maximum of total ozone content. It should be noted that unusual wave amplifications described in this chapter sometimes occur in SH stratosphere.

5 Mechanism of wave 1 amplification due to traveling wave 2

The subjects in this section are to simulate the wave-mean flow and wave-wave interactions in the Southern Hemisphere and to clarify the mechanism of wave 1 amplification. The hemispherical model is used for the numerical experiments. The results are essentially same with those when the spherical model is used. The climatological zonal-mean winds in SH from July to October shown in Fig.2.2 are adopted as initial winds in this section.

The results are given in Section 5.1. In Section 5.2, the analysis of energy and potential enstrophy budget of the waves for the most typical case is presented. The amplification mechanism of wave 1 is described in Section 5.3 and roles of the wave-wave interaction on the amplitude variation are discussed in Section 5.4. Some related discussion is presented in Section 5.5.

5.1 Amplitude variation

5.1.1 Amplitude variation under August wind condition

First of all, the results are shown for the experiment using the monthly mean zonal wind of August (termed Case A1) as the initial zonal wind. The maximum forcing amplitude of stationary wave 1 from the troposphere is 100 m in geopotential height. The forcing amplitude of the eastward traveling wave 2 is also 100 m with a period of 20 days. No wave is given for wavenumber 3 component initially. Fig.5.1 shows the temporal variation of amplitude (a) and the location of the ridge (b) of the waves at the 40 km level and 60° S . In this figure the amplitude of wave 1 (thick solid line) reaches the maximum value ($\sim$ 2000 m), when the ridge of wave 2 (dashed line) overlaps that of wave 1. At this time the amplitude of wave 2 takes the minimum value. That is, the amplitude of wave 2 is negatively correlated with wave 1. The large amplification of wave 1 occurs only once for every two passages of wave 2. This variation is termed *subharmonic variation.* The amplitude of wave 3 (thin solid line) is very small compared with wave 1 and 2, and its eastward phase speed is 2/3 that of wave 2. The characteristics of waves 1 and 2 are similar to those of observed variations: August to September 1971 (Leovy and Webster, 1976), August 1973 (Hartmann, 1976), October 1983 (SKH), and the latter half of August to the first half of September 1988 (HKS).

The amplitude distributions in latitude-height cross-section for waves 1 and 2 are shown in Fig.5.2. Day 72 corresponds to the time of the amplitude minimum of wave 1 while day 87 is the time of its maximum. The positions of the wave 1 amplitude maxima are located at 70° S and 42 km on both days. The amplitude of wave 2 maximum is located slightly equatorward and slightly lower than that of wave 1: 65° S and 32 km,

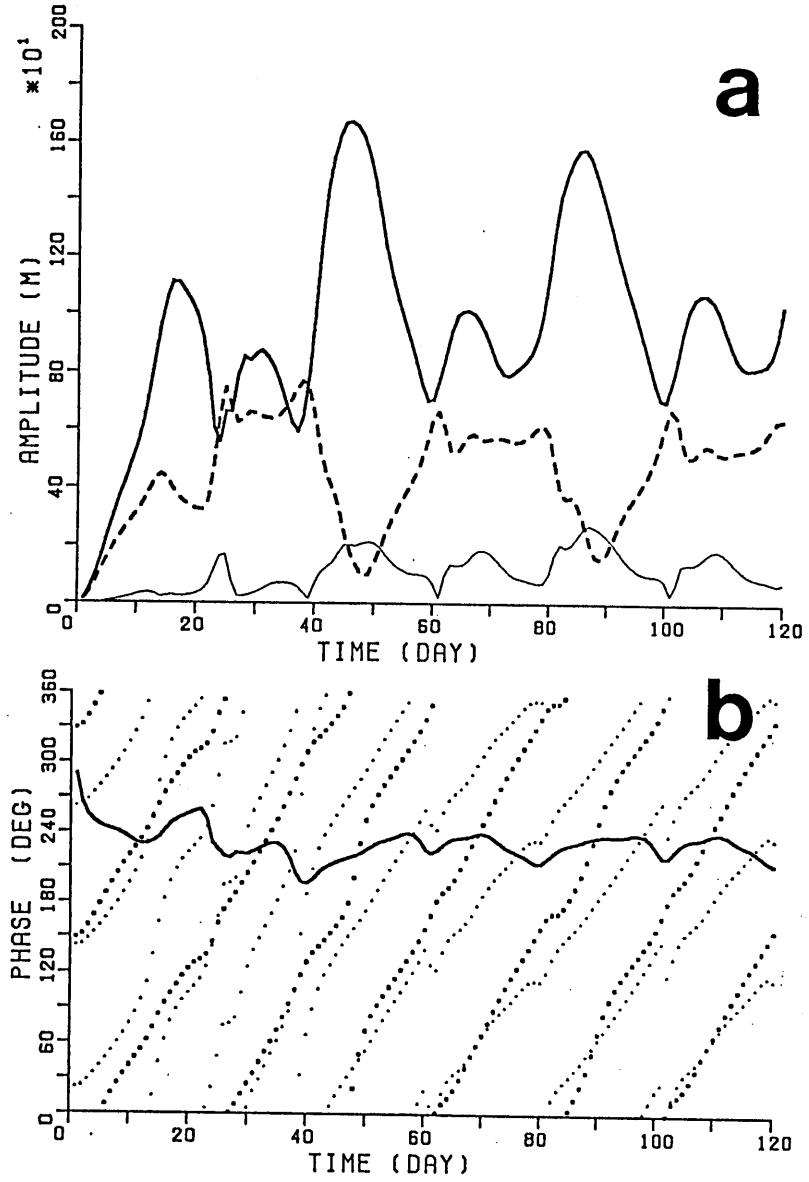

Fig.5.1: Temporal variation of (a)wave amplitude and (b)ridge location in longitude at 60° and 40 km for the zonal-mean wind of August as a initial wind. (a)Thick solid line denotes wave 1 amplitude, the dashed line wave 2, and the thin solid line wave 3. (b) Solid line denotes the ridge location of wave 1, the thick dotted line wave 2, and the thick dotted line wave 3.

respectively. The amplitude of wave 1 extends to the lower mesosphere, while that of wave 2 is confined to the stratosphere. The location and meridional extent of the waves are quite similar to these of observed waves during October 1983 (SKH).

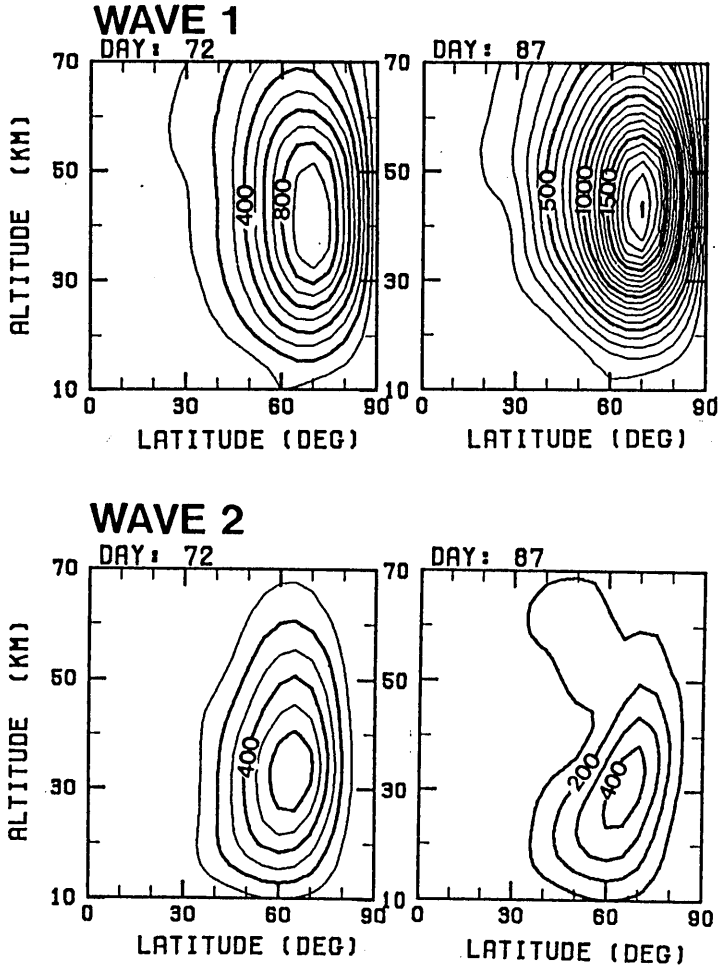

Fig.5.2: Amplitude distribution in a meridional plane at day 72 (left) and 87 (right). Upper panels show that of wave 1 and lower panels wave 2. Contour interval is 100 m.

The vertical profile of the phase of the geopotential height at 60° S is presented in Fig.5.3. The phase of wave 1 is tilted westward with increasing height in the lower stratosphere (below 25 km) with the tilt being very small above the midstratosphere. During the period of one passage of the phase of wave 2 over wave 1, the phase tilt of wave 1 exhibits little change while the tilt in the lower stratosphere varies somewhat. On the other hand, the eastward traveling wave 2 has small phase tilt in the stratosphere during this period. The phase of wave 2 is tilted slightly westward with increasing height before the passage and turns eastward during the passage. This change in the wave 2 phase tilt is analogous to that observed in October 1983.

Figure 5.5 shows the temporal variation of the geopotential height field at the

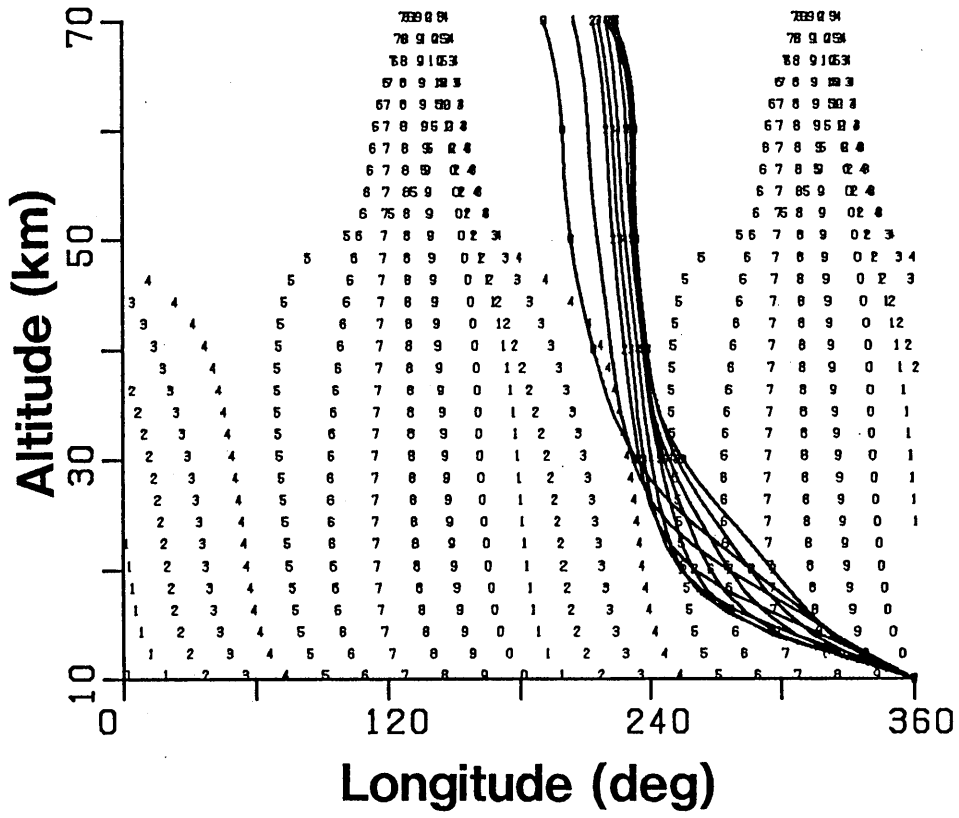

Fig.5.3: Ridge location in a longitude-altitude cross section at 60°S during day 80-98 with 2 day interval. Solid line indicates the ridge location of wave 1. The ridge location of wave 2 is shown by numbers. The numbers (n) indicate the day $2n + 80$.

km level over the Southern Hemisphere. Two ridges exist on the opposite sides of the pole, moving eastward at a speed of about 10 degrees a day during day 72 to 78. The prominent pattern in this period can be characterized by wave 2. During the next period, one ridge is intensified while the other is weakened. As a result, the wave 1 pattern dominates during day 84 to 90. This pattern moves at a speed of 5-10 degrees a day. The amplified ridge decays with time and the pattern of day 93 returns to that of day 72. This temporal variation of the geopotential height field is also very similar to that observed during October 1983 (Fig.5.4), but the observed pattern moves about as twice as the simulated pattern.

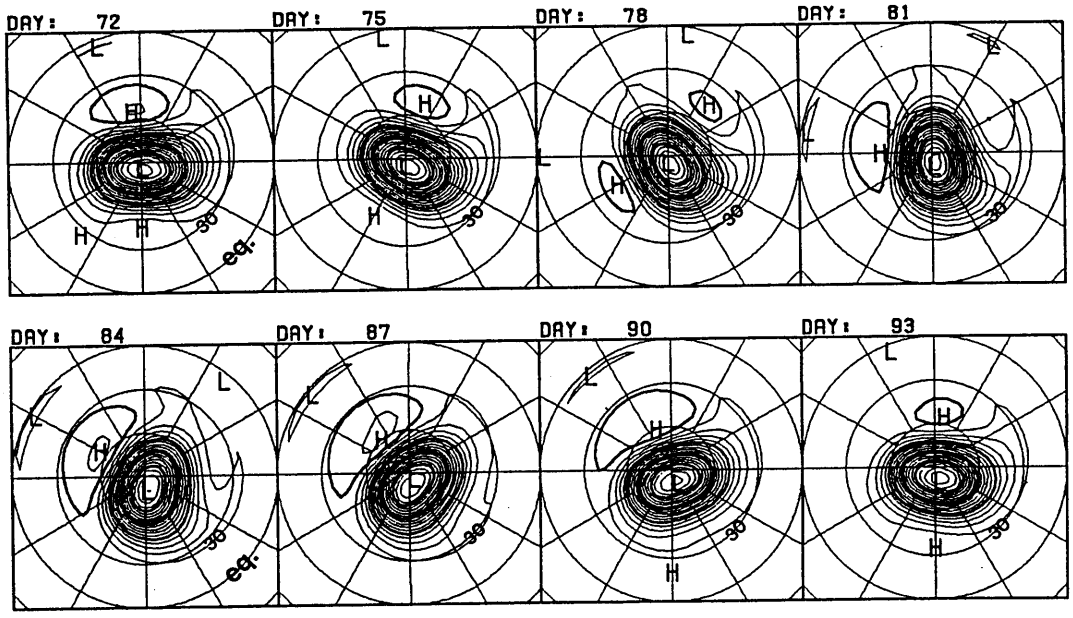

Fig.5.4: Geopotential height field from day 72 to 91 at the 30 km level in the Southern Hemisphere. Contour interval is 200 m.

5.1.2 Results for various initial zonal-mean winds and wave forcing

Calculations are carried out under various conditions in order to clarify how the variation in wave amplitude depends on the initial wind and wave forcing. The initial conditions are listed in Table 5.1 and the individual monthly mean zonal winds from July to October, each of which was used as initial wind, are shown in Fig.5.6. The monthly mean zonal winds are actually composites of satellite data over 5 years from 1973 to 1978 (Fleming et al. 1988). The calculated variations of the amplitude of wave 1 for the individual zonal winds and various forcing are shown in Fig.5.7. Here, a brief description of the results when compared with Case A1 (defined in the above subsection) is presented.

1) DEPENDENCY ON INITIAL ZONAL WIND

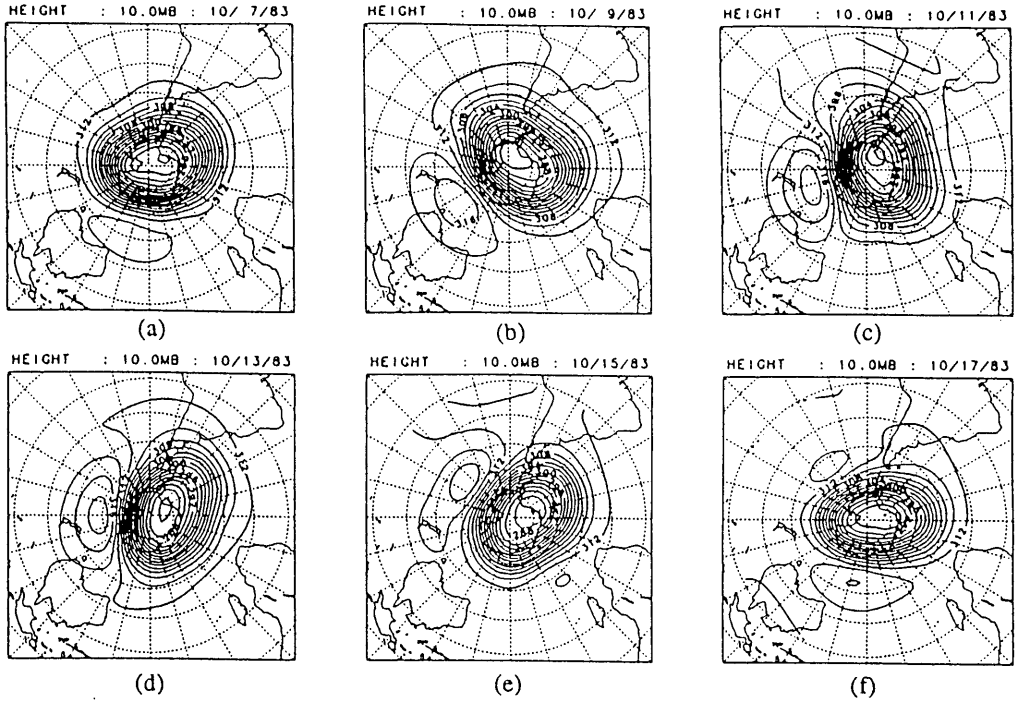

Fig.5.5: Observed geopotential height field from October 10 to October 17 in 1983 at the 30 km level in the Southern Hemisphere. Contour interval is 200 m. (from Siotani et al., 1990)

Table 5.1: Parameters of the calculations

Case	*Month of initial zonal wind*	Wave 1 amplitude	Wave 2 amplitude	Wave 2 period	Wave 3 amplitude	Wave 3 period
J1	JULY	100 m	100 m	20 day	0 m	–
A1	AUGUST	100 m	100 m	20 day	0 m	–
S1	SEPTEMBER	100 m	100 m	20 day	0 m	–
O1	OCTOBER	100 m	100 m	20 day	0 m	–
A2	AUGUST	100 m	100 m	15 day	0 m	–
A3	AUGUST	100 m	100 m	10 day	0 m	–
A4	AUGUST	100 m	50 m	20 day	0 m	–
A5	AUGUST	150 m	100 m	20 day	0 m	–
A6	AUGUST	100 m	100 m	20 day	70 m	13.3 day

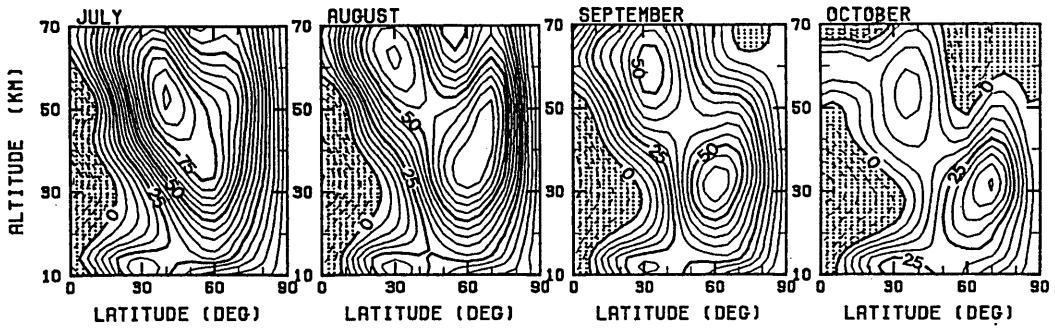

Fig.5.6: Monthly mean zonal wind for July to October in a meridional plane. Solid contour lines with the interval of 5 ms^{-1} denote positive values and dashed lines negative values. Negative region is also shaded.

Figure 5.7a shows the amplitude variations of wave 1 for initial zonal-mean winds of July (J1), August (A1), September (S1), and October (O1). The forcing amplitude of the waves and the period of wave 2 at the tropopause are the same as those in Case A1.

The July westerly jet is located at 40° S and a level of 53 km, which is shifted about 10° equatorward and 10 km upward from that of August. In this case (J1), the wave 1 amplitude varies with the period of 20 days and reaches a maximum when the phase of wave 2 overlaps that of wave 1. This feature is similar to Case A1. In Case J1 amplifications of the wave 1 are a little larger before day 60 but reach almost the same magnitude.

The jet core in September is shifted 10° poleward and 10 km downward from that of August, and the maximum wind speed is 10 ms^{-1} less than that of August. In this case (S1), a subharmonic variation similar to Case A1 can be seen after day 20, even though the amplitude variations of the waves are about 40% less than in Case A1. When the October wind (O1) is used, the variation of wave 1 is quite different from previous calculations. The amplitude of wave 1 reaches a maximum at day 30 and then gradually decays. The amplitude is slightly restored after day 60, but the amplitude is very small compared with the previous cases. The periodic variation is hardly seen. In this case, since the high latitude zonal wind from the midstratosphere to mesosphere is replaced by easterlies due to the wave forcing (see Fig.5.8), the planetary waves propagation is severely restricted in the easterly region.

2) DEPENDENCY ON PERIOD OF WAVE 2

The results of calculation are shown in Fig.5.7b for the same conditions as Case A1 except that the period of wave 2 is replaced by 15 days (Case A2) and 10 days (Case A3). For Case A2 the wave 1 amplitude varies periodically with a period of 15 days. The values of maxima, however, differ for every amplification and the subharmonic variation

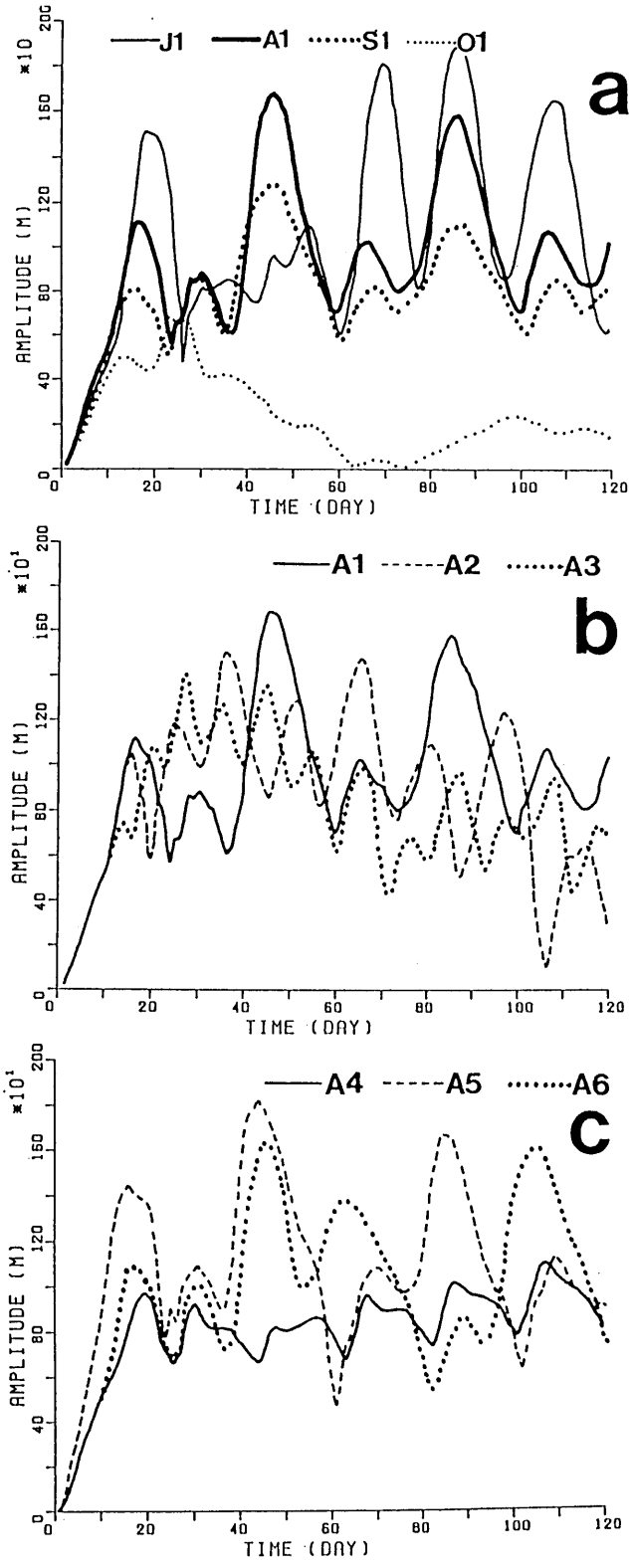

Fig.5.7: Temporal variation of wave 1 amplitude at 60°S and 40 km under various conditions (see Table 5.1). (a)Case J1 (thin solid line), Case A1 (thick solid line), Case S1 (thick dotted line), Case O1 (thin dotted line). (b) Case A1 (thick solid line), Case A2 (thin solid line), Case A3 (dash-solid line). (c) Case A4 (thick dotted line), Case A5 (thin dotted line), Case A6 (dashed line).

does not appear. In Case A3 the wave 1 amplitude displays the maxima with a 10 day interval. The subharmonic variation appears after day 60, but the amplitude of the variation is very small compared with Case A1.

3) DEPENDENCY ON FORCING AMPLITUDE

The forcing amplitude of wave 1 or wave 2 is changed at the bottom boundary. When the amplitude of wave 2 is reduced from 100 m to 50 m (Case A4), the large amplification does not occur and the amplitude varies regularly with a period of 20 days. Next, the forcing amplitude of wave 1 is set to be 150 m (Case A5). The variation of the pattern is very similar to that of Case A1, differing only in the magnitude of the variation being slightly larger than A1.

Finally, it is examined that the effects of the wave 3 forcing because the eastward traveling wave with wavenumber 3 also has the amplitude at the tropopause level (Hartmann, 1976). Wavenumber 3 forcing was added with an amplitude of 70 m in geopotential height and 13.3 days in period so as to have the same phase speed as wavenumber 2. Under these conditions (A4), the amplitude variation of wave 1 is similar to Case A1 before day 50. Then a large amplification begins to appear with a period of 40 days, although the phase of the large amplification is opposite to that in Case A1. The reason of unchanged results is that wave 3 at the tropopause level is difficult to propagate into the stratosphere because of strong westerly wind.

Using different zonal-mean winds and forcing for initial conditions, it is recognized that amplitude variations of waves 1 and 2 must occur during the late winter to early spring in the Southern Hemisphere stratosphere whenever the stationary wave 1 and eastward traveling wave 2 coexist and both waves amplitudes are more than several decameters at the tropopause level.

5.1.3 Comparison of zonal winds

The zonal-mean winds at day 100 are shown in Fig.5.8 for the various calculations stated above. In general, all the stratospheric westerly jets shift poleward from the initial position (Fig.5.6) except for Case O1. It is recognized that some patterns in Fig.5.8 are rather similar to that of the following month of initially specified month, i.e., J1 compared with August, A1 and A4 with September, S1 with October. In particular, the zonal-mean wind at day 100 of Case S1 is very similar to that of October shown in Fig.5.6. It is considered that the simulated variations occur not in the initially specified month but in the following month since the observed monthly mean winds are also under the influence of the wave forcing. Moreover, this suggests that the seasonal evolution during late winter to early spring (i.e., poleward and downward shift of the polar night jet) is due to mainly the wave forcing, which has already been noted through analytical studies (Hartmann et al., 1984; Shiotani and Hirota, 1985; Mechoso et al., 1988).

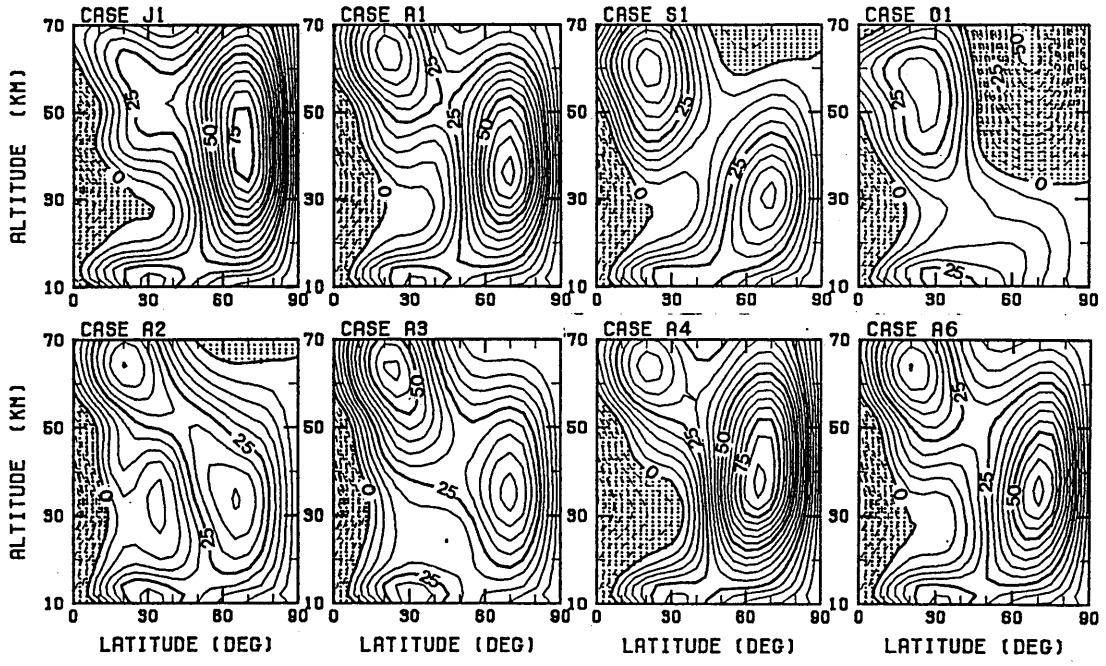

Fig.5.8: Zonal mean wind at day 100 for Case J1, A1, S1, O1, A2, A3, A4, and A5. Contour interval is 5 ms^{-1} and negative regions are shaded.

5.2 Analysis of energy and enstrophy budget

The amplitude variation obtained in Case A1 exhibits the most typical characteristics among the calculations; the amplitude of the stationary wave 1 varies remarkably and the subharmonic variation clearly appears. This subsection shows results of the analysis of the energy and potential enstrophy budgets for Case A1.

5.2.1 Energy conversion

Temporal variations of kinetic and available potential energy of the three waves, integrated over the regions from the equator to pole of between 10 and 30km (lower region) and between 30 and 110km (upper region), are shown in Figs.5.9a and 5.9b, respectively. In the lower region, the potential energy of wave 1 is about twice as large as the kinetic energy. The kinetic energy of wave 1 dominates over the potential energy in the upper region, being about 4 times larger than the potential energy. This means that wave 1 has a baroclinic structure in the lower region and a barotropic structure in the upper region, as seen in Fig.5.3. The kinetic energy and potential energy of wave 2 have the same magnitude in the lower region. The kinetic energy of wave 2 strongly dominates over the potential energy in the upper region. The dominance corresponds to a barotropic structure of wave 2 in the upper region (Fig.5.3). The kinetic and potential energy of wave 3 are very small compared with waves 1 and 2 over both regions. Wave 3 also has a barotropic structure in the upper region since kinetic energy dominates over potential energy. The temporal variation of the kinetic energies of the waves in the upper region are quite similar to those of the wave amplitudes at 60° S and 40 km (Fig.5.1a). The discussion is focused on the kinetic energy conversion in the upper region since the temporal variations are more remarkable than those in the lower region. Also the kinetic energy component is dominant overall.

The rate of change of kinetic energy for a given wavenumber m can be expressed by the sum of five energy conversion terms as

$$\frac{\partial K_m}{\partial t} = C(K_n, K_m) + C(K_z, K_m) + C(E_m) + C(A_m, K_m) + D(K_m) \ . \qquad (5.1)$$

The first term on the right-hand side of the equation, $C(K_n, K_m)$, represents the conversion of kinetic energy to wavenumber m from other wavenumbers. This term is called the wave-wave interaction term. The second term $C(K_z, K_m)$ is the conversion of kinetic energy from the zonal-mean flow to wavenumber m. The third term $C(E_m)$ represents the convergence of the wave energy flux and the fourth term $C(A_m, K_m)$ the conversion from the wave's potential energy to the wave's kinetic energy. The last term $D(K_m)$ is the dissipation of kinetic energy due to Rayleigh friction and vertical viscosity. The convergence term $C(E_m)$ integrated over the upper region is equivalent to the meridionally integrated vertical energy flux at a height of 30 km (see Appendix D).

Figure 5.10 displays the temporal variation of the kinetic energy conversion terms averaged over the upper region. The wave-wave interaction term (thick solid line) of wave 1 oscillates with a period of 20 days; the values remaining almost always negative during the period of the calculation (Fig.5.10a). This indicates that on the time average wave 1 supplies kinetic energy to waves 2 and 3. The wave-wave interaction term of wave 2 also oscillates with a period of 20 days (Fig.5.10b). Here the value of $C(K_n, K_2)$ is positive when the interaction term of wave 1 has a large negative value, while $C(K_n, K_2)$

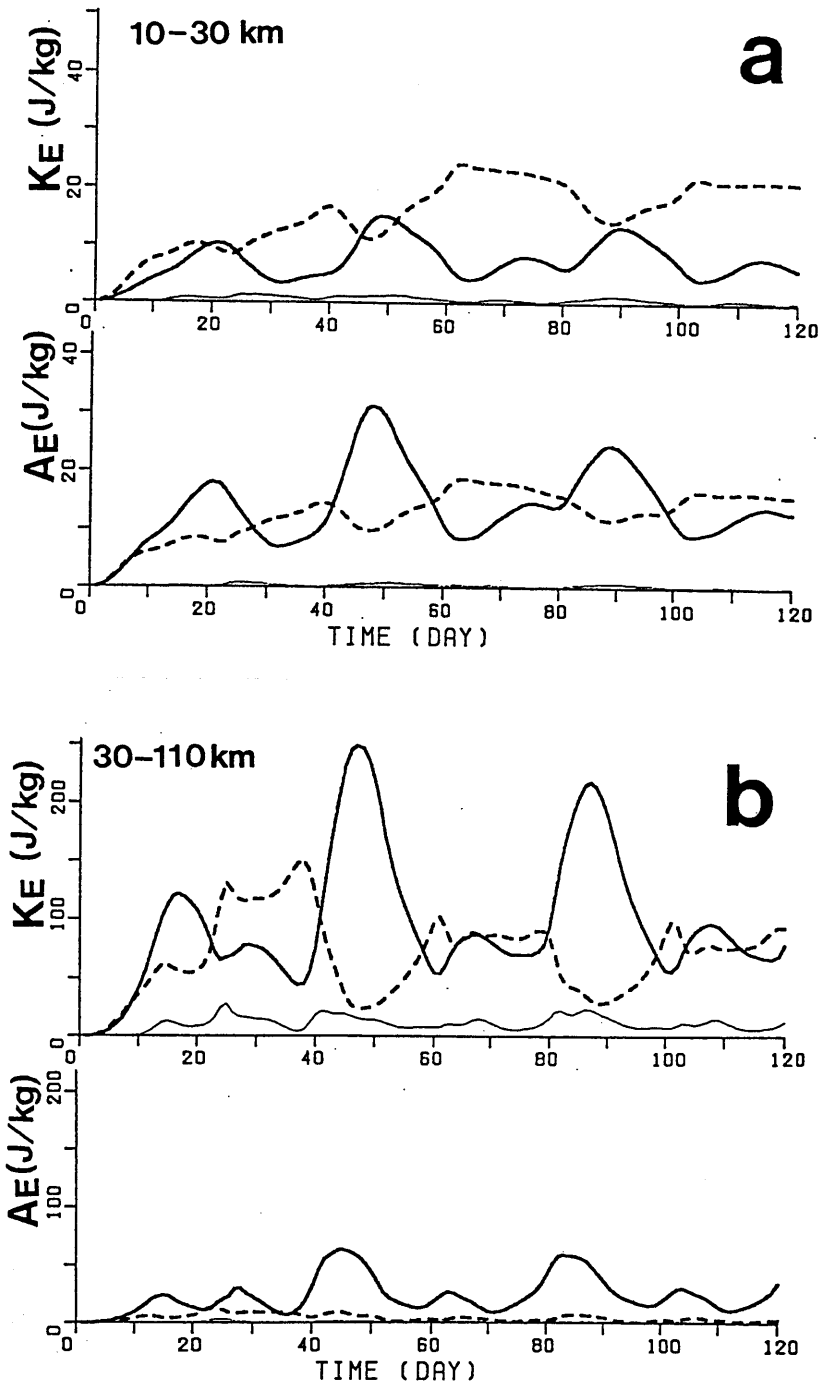

Fig.5.9: Temporal variation of kinetic and potential energy for wave 1 to 3 of Case A1. (a) The energies averaged over the lower region: 10-30 km in height and from the equator to pole. (b) The energies averaged over the upper region: 30-110 km and from the equator to pole. Upper panels are the variations of kinetic energy and lower panels potential energy. Thick solid line represents a wave 1, dotted line wave 2, and thin solid line wave 3.

2 receives kinetic energy from wave 1 and supplies it to wave 3. Contrary to wave 1, the interaction term of wave 3 is almost always positive, the value being large when the $C(K_n, K_m)$ term of wave 1 or wave 2 has large negative values. This indicates that wave 3 receives kinetic energy from waves 1 and 2.

The $C(K_z, K_1)$ and $C(E_1)$ terms have almost the same magnitude but opposite signs. This indicates that the energy flux from the 30 km level is mainly consumed by the conversion of kinetic energy to the zonal-mean flow. The same relationship also appears in wave 2. For wave 3, $C(E_3)$ is very small and $C(K_z, K_3)$ is almost balanced by $C(K_n, K_3)$. This balance means that the wave 3 energy supplied from waves 1 and 2 is consumed by the conversion to the zonal mean flow. Conversion from potential energy to kinetic energy $C(A_m, K_m)$ for all three waves is quite small compared with first three terms in Eq.(5.1), due to the barotropic structure of the waves, as previously mentioned. The last dissipation term $D(K_m)$ is negligible when compared with the other terms.

After day 30, the rate of change of kinetic energy of wave 1, $\partial K_1/\partial t$, displays two large positive peaks at days 42 and 83, and two small positive peaks at days 63 and 103. Namely, large amplification occurs with a period of 40 days as seen in the amplitude variation (Fig.5.1a). The wave-wave interaction term of wave 1 remains negative, even during all of the amplification periods. That is, the wave 1 energy averaged over the upper region is not supplied by the direct conversion of energy from other waves. It should be noted that $C(K_z, K_1)$ suddenly increases during the early stage of the amplification period (day 40, 60, 80, and 100). The rapid increase in $C(K_z, K_1)$ destroys the balance with $C(E_1)$ and consequently leads to the amplification of wave 1.

After the large amplifications occur, wave 1 decays during day 47-60 and day 87-100. At these times, the wave-wave interaction term of wave 1 is negatively large, while $C(K_z, K_1)$ and $C(E_1)$ almost cancel each other. The energy of wave 1 is mainly converted to wave 3 and partially to wave 2. Therefore, the decay of wave 1 is caused by the energy transfer to other waves.

The variation of $C(E_1)$ is not synchronized with $\partial K_1/\partial t$ although the variation of $C(E_m)$ is large. The value of $C(E_1)$ in the upper region is controlled by the energy conversion to kinetic energy from available potential energy in the lower region (10-30km).

5.2.2 Potential enstrophy conversion

The temporal variation of wave activity can be expressed more simply by potential enstrophy analysis. The rate of change of quasi-geostrophic potential enstrophy (PE) for given wavenumber m is expressed by the sum of three conversion terms as

$$\frac{\partial}{\partial t}\left(\frac{1}{2}\overline{q_m^2}\right) = -\frac{1}{a}\frac{\partial \overline{q}}{\partial \theta}\overline{q_m v_m} + C(q_n, q_m) + D(q_m) \ , \tag{5.2}$$

where q_m is the quasi-geostrophic potential vorticity (PV) of wavenumber m, and $\partial\overline{q}/\partial\theta$ the meridional gradient of zonal-mean PV. The first term on the right-hand side of the equation represents the conversion of PE from the zonal-mean flow to wavenumber m. The second term $C(q_n, q_m)$ is the conversion of PE from other wavenumbers to wavenumber m. The third term $D(q_m)$ represents the dissipation of PE due to Newtonian cooling, Rayleigh friction and the vertical viscosity.

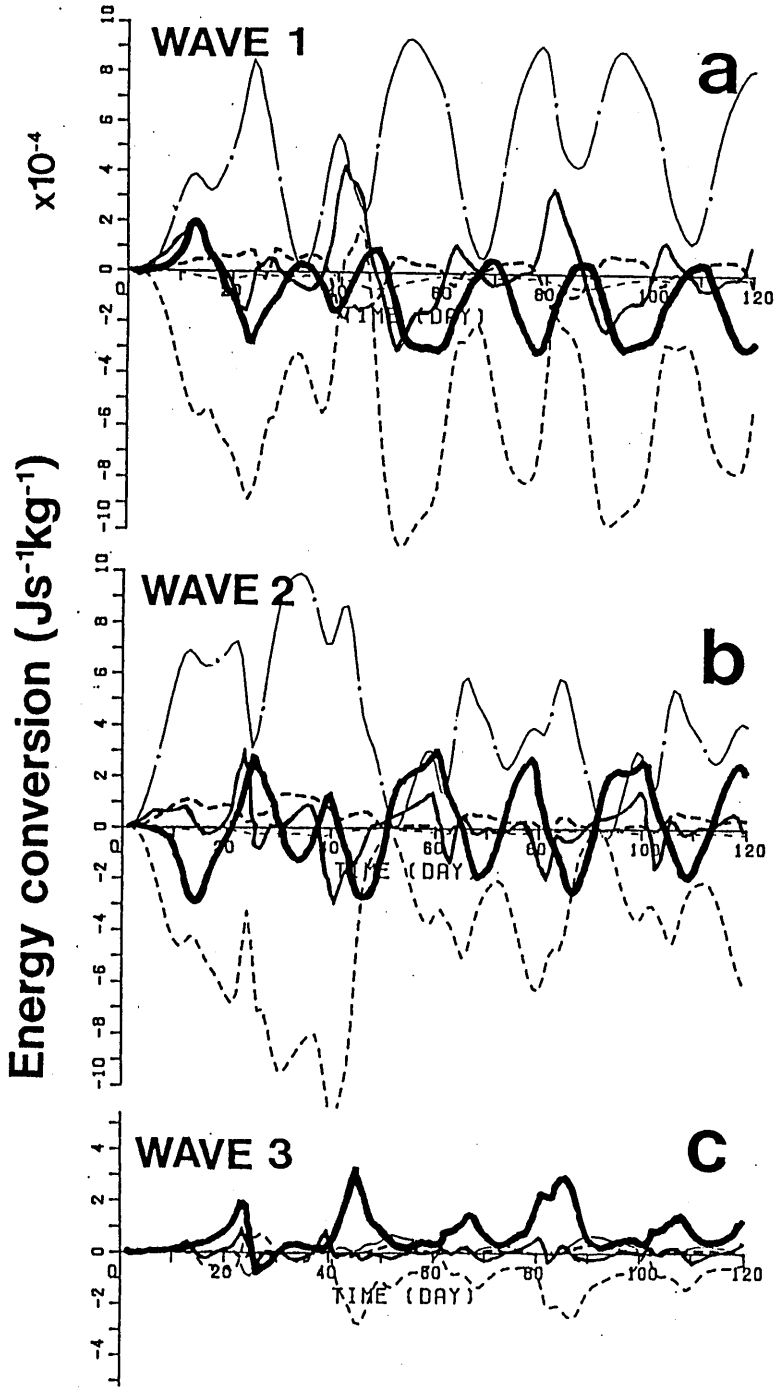

Fig.5.10: Temporal variation of the energy conversion terms averaged over the upper region. (a) wave 1, (b) wave 2, and (c) wave 3. Thin solid line represents $\partial K_m/\partial t$, thick solid line $C(K_n, K_m)$, dash-dotted line $C(E_m)$, middle dashed line $C(K_z, K_m)$, thick dashed line $C(A_m, K_m)$, and thin dashed line $D(K_m)$.

wavenumber m. The third term $D(q_m)$ represents the dissipation of PE due to Newtonian cooling, Rayleigh friction and the vertical viscosity.

Figure 5.11 shows the temporal variation of the rate of PE's change of wave 1 and its conversion terms, integrated over the upper region (30-110 km, equator to pole). The rate of PE's change (middle solid line) varies with time similar to that of energy (Fig.5.10a). The subharmonic variation appears to be more clear in the wave-wave interaction term (thick solid line) and the wave-mean flow interaction term (dotted line) for PE conversion than those for energy conversion (Fig.5.10a).

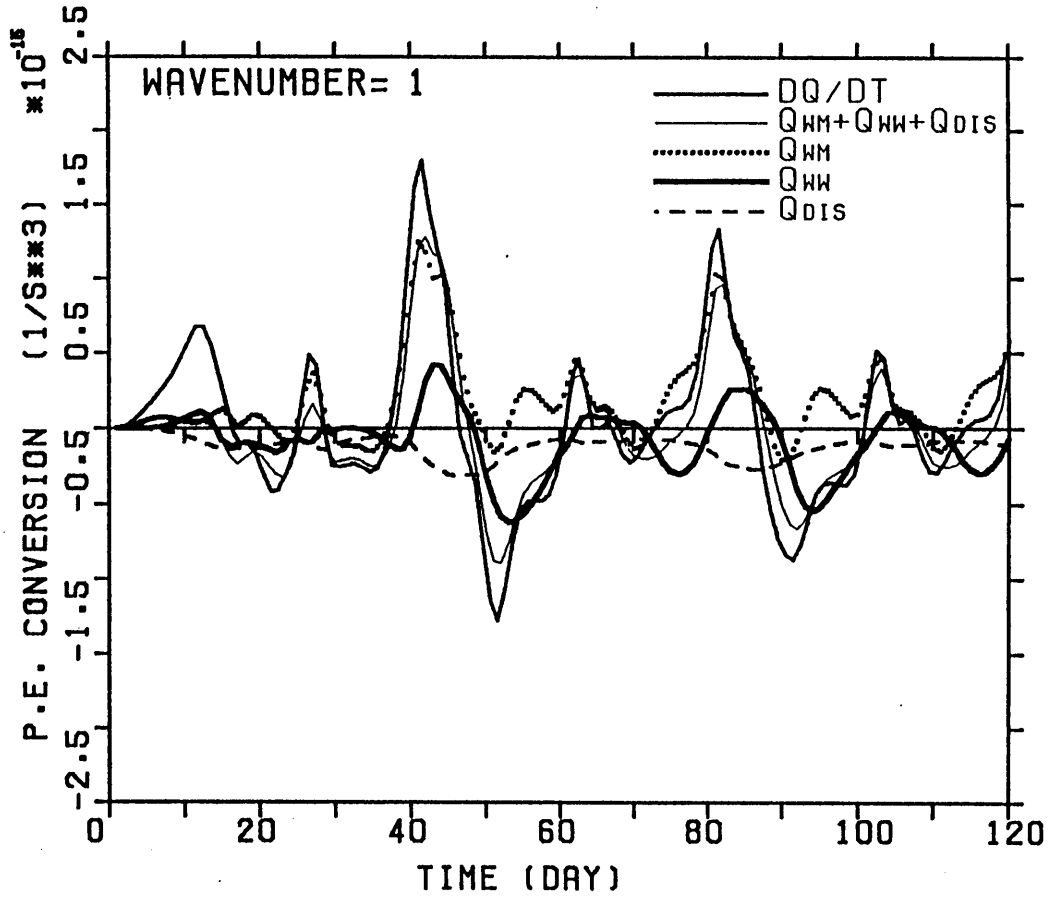

Fig.5.11: Temporal variation of the conversion of quasi-geostrophic potential vorticity for wave 1 of Case A1 averaged over upper region. Middle solid line represents time derivative of the potential vorticity. Dotted line represents the interaction term the with zonal-mean flow (Q_{WM}), thick solid line the wave-wave interaction term (Q_{WW}), dashed line the dissipation term (Q_{DIS}), and thin solid line the sum of these three terms ($Q_{WM} + Q_{WW} + Q_{DIS}$).

Figure 5.11 clearly shows that the amplifications of wave 1 during day 38-48 and day 78-88 are caused by the PE conversion from the zonal-mean flow to the wave, while the decays of wave after those amplifications are mainly caused by the PE conversion to other wavenumbers. For the energetics analysis discussed in previous subsection, the energy conversion term from the zonal-mean flow of wave 1, $C(K_z, K_1)$, is always

1. While, for the PE analysis, the PE conversion from the zonal mean flow, $C(q_z, q_1)$, is positive almost always during the period of calculation and the increase of $C(q_z, q_1)$ is directly related to the amplification of wave 1. Namely, the variation of enstrophy of wave 1 is mainly controlled by the variation of the wave-mean flow interaction.

The cause of the variation of wave 1 is same with that presented by Robinson(1985). In his model, wave 1 is traveling westward and wave 2 is stationary, while wave 1 is stationary and wave 2 is traveling eastward in our model. Robinson's configuration becomes equivalent to that of present study, when the coordinate is transferred to the rotating coordinate with the same speed of the westward traveling wave. This suggests that similar mechanism for the amplitude variation takes place in both studies.

5.3 Mechanism of wave 1 amplification

The analysis of energy and enstrophy budgets in the previous subsection reveals that the variation of the conversion term of wave-mean flow interaction has an essential effect in the process of the wave 1 amplification and that of wave-wave interaction has a secondary effects in the process. This subsection shows the mechanism of wave 1 amplification in the light of the quasi-linear theory.

5.3.1 Variation of EP flux

Figure 5.12 shows EP flux of wave 1 at day 72, 76, 81 and 91. Day 72 represents the day of the minimum of wave 1 amplitude, day 81 does the amplification stage and day 91 is the decay stage.

Direction of the EP flux considerably changes through the stages. At days 72 and 76, the flux around 60°S changes its direction from upward to equatorward with increasing altitude. On the other hand, the direction of EP flux at day 81 is almost vertical through the stratosphere. The amplification of wave 1 in the upper stratosphere is a result of the focus of EP flux to the highlatitudes during day 79-85. In the decay stage (day 91), the direction of EP flux inclines again equatorward similar to that of days 72 and 76.

The term of the energy conversion from a wave to the zonal mean flow is closely related to the direction of EP flux because the meridional component of EP flux is proportional to the latitudinal momentum transport. The term $C(K_m, K_z)$ $(= -C(K_z, K_m))$ can be considered as the product of the meridional gradient of the zonal-mean flow and the poleward momentum flux due to wavenumber m (the exact formula is shown in Appendix D). Thus, the rapid decrease of $C(K_1, K_z)$ in Fig.5.10a is due to the change of the direction of EP flux from equatorward to vertical in the stratosphere.

5.3.2 Wave-mean flow interaction (Quasi-linear theory)

Figure 5.13 shows the zonal-mean wind and refractive index square (RI) for wave 1 at days 75, 80, 85 and 90. RI for zonal wavenumber m is defined as follows

$$Q_m = \frac{a}{\overline{u}}\frac{\partial \overline{q}}{\partial \theta} - m^2 - \frac{f^2}{N_{BV}^2}\frac{a^2}{4H^2} \quad . \tag{5.3}$$

Distribution of the zonal-mean flow and the velocity of the polar night jet in the stratosphere do not change significantly but latitudinal shear of the zonal-mean wind in the midlatitudes at day 80 is slightly enhanced than other days.

RI is more changeable than the zonal-mean wind. There are a maximum line of RI along 65° in the stratosphere and a minimum line in the midlatitudes stratosphere every stage. The considerable difference of RI at day 80 from day 75 is appearance of a negative region in the midlatitudes upper stratosphere (around 50° and 45km). Appearance of the negative region is accompanied by extension of the minimum line in the midlatitudes to the lower mesosphere. The maximum line in the highlatitudes also extends to the stratopause level at day 80. Formation of the negative region of RI is a result of the enhanced latitudinal shear of the zonal-mean wind (Fig.5.13b). The negative region appear at day 78 and disappear at day 82. Appearance of the negative region forms a wave guide in the highlatitudes stratosphere. Comparing with EP flux

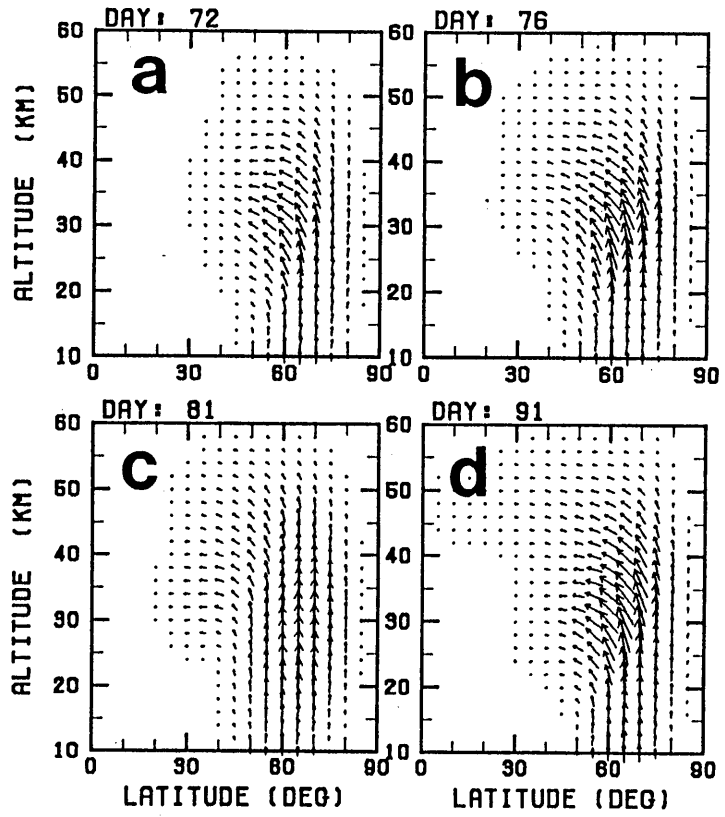

Fig.5.12: EP flux of wave 1 in a meridional plane at days 72, 76, 81 and 91. The vectors are multiplied by $\exp(z/2H)$.

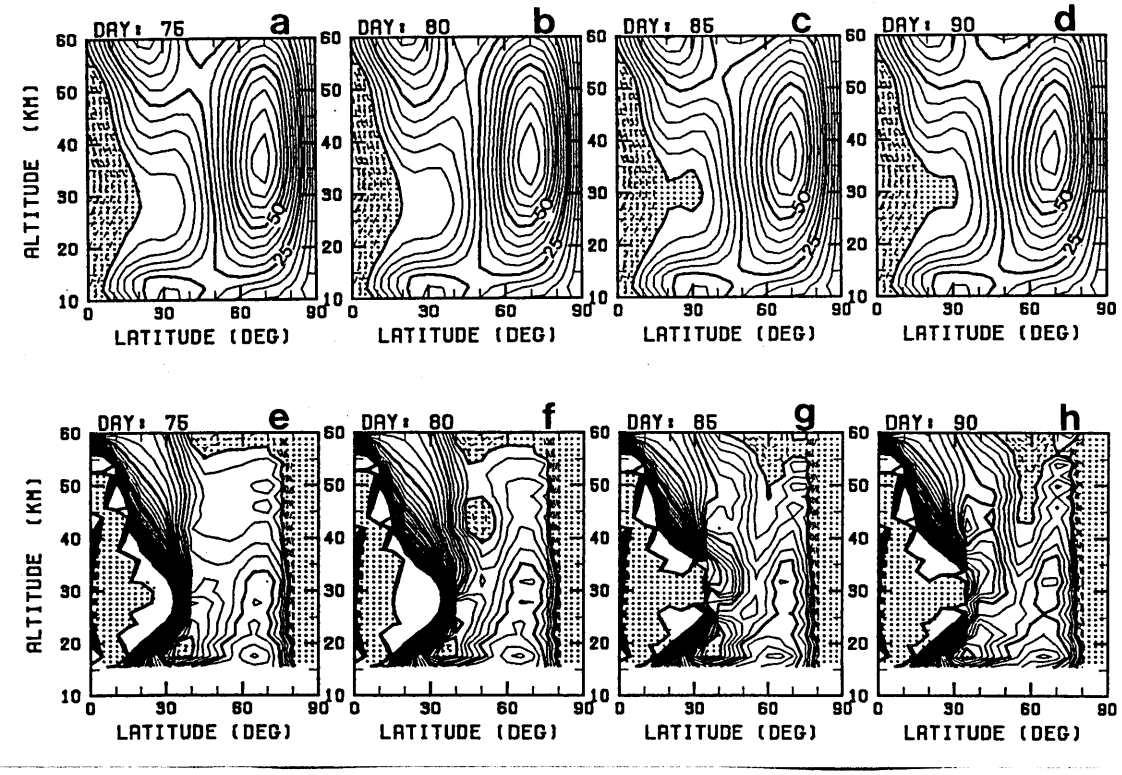

Fig.5.13: Zonal mean wind (a,b,c,d) and refractive index (RI) for wave 1 (e,f,g,h) in a meridional plane at days 75, 80, 85 and 90. Contour interval of the zonal wind is $5\mathrm{m\,s^{-1}}$ and that of RI is 5 (nondimension). Negative regions of the zonal wind and RI are shaded.

(Fig.5.12b,c) and RI (Fig12e,f), it is found that the variation of RI is followed by the variation of the direction of EP flux. Namely, the focus of EP flux to the highlatitudes stratosphere is due to the formation of the wave guide.

The internal jet instability condition presented by Charney and Stern (1962) is satisfied when the negative region appears. However, it is difficult to interpret the change of EP flux as a result of the instability because the kinetic energy conversion from the zonal wind to wave 1 is negative even in the amplification stage (Fig.5.10a).

It should be noted that the direction of EP flux does not always agree with the maximum line of RI. Although the maximum line of RI exists in the highlatitudes yet during decay stage (Fig.5.13h), the direction of EP flux inclines equatorward in the stratosphere (Fig.5.12d). Transiency of the wave may cause the inconsistency between the direction and RI. The direction of EP flux is also affected by the wave-wave interaction as considered in next subsection.

Figure 5.14 shows the wave driving (EP flux divergence divided by the air density and $\cos\theta$) of waves 1-3 at days 74 and 82. At day 74, negative region of the wave driving of wave 1 is centered at 55° and 35km and the value of the wave drivings of waves 2 and 3 is very small compared with that of wave 1. Induced residual circulation driven by the wave driving slightly accelerates the polar night jet in the highlatitudes. Deceleration of the zonal wind in the midlatitudes due to the wave driving of wave 1 leads to the enhancement of latitudinal shear of the zonal mean wind in the equatorial side of the polar night jet. During the amplification stage (day 82), the large negative value of the driving term of wave 1 is compensated by the large positive value of wave 2 (Fig13b,d). Positive value of wave 3 at day 82 contributes the net acceleration of the zonal-mean wind in the midlatitudes. This acceleration weakens the latitudinal shear of the zonal wind, which results in disappearance of the negative region of RI for wave 1. The contrast of the wave drivings between wave 1 and wave 2 at day 82 indicates the energy and enstrophy transfer between these waves.

The process of amplification of wave 1 shown in this subsection is summarized as follows. Wave 1 propagates upward and equatorward which is accompanying with poleward momentum transport. The zonal flow is accelerated in the highlatitudes and decelerated in the midlatitudes, which lead to the enhancement of latitudinal shear of the zonal-mean wind. In the course of time, the negative region appears in the midlatitudes and the wave guide forms at the highlatitudes. Then, wave 1 propagates almost vertically in the wave guide, which leads to the wave 1 amplification in the upper stratosphere.

This amplification process is essentially similar to that of stratospheric sudden warming firstly presented by Matsuno (1971), while deceleration of the zonal wind is very weak in our simulation because of weakness of the forcing amplitude. Holton and Mass (1976) showed that the wave-mean flow interaction leads to a periodic variation of a wave amplitude and zonal-mean wind. However, under the condition of Southern Hemisphere adopted in this study, the zonal-mean flow interaction does not cause the periodic variation. Indeed, if only the interaction between wave 1 and zonal-mean flow is allowed under the same condition with Case A1, the state of the stratosphere falls in the steady state where deceleration of the zonal wind due to wave 1 valances with acceleration caused by differential heating. The maximum amplitude of wave 1 for steady state is about 1200 m which is about half of the averaged value of the Case A1. This means that the wave-wave interaction causes the periodic variation around the steady state.

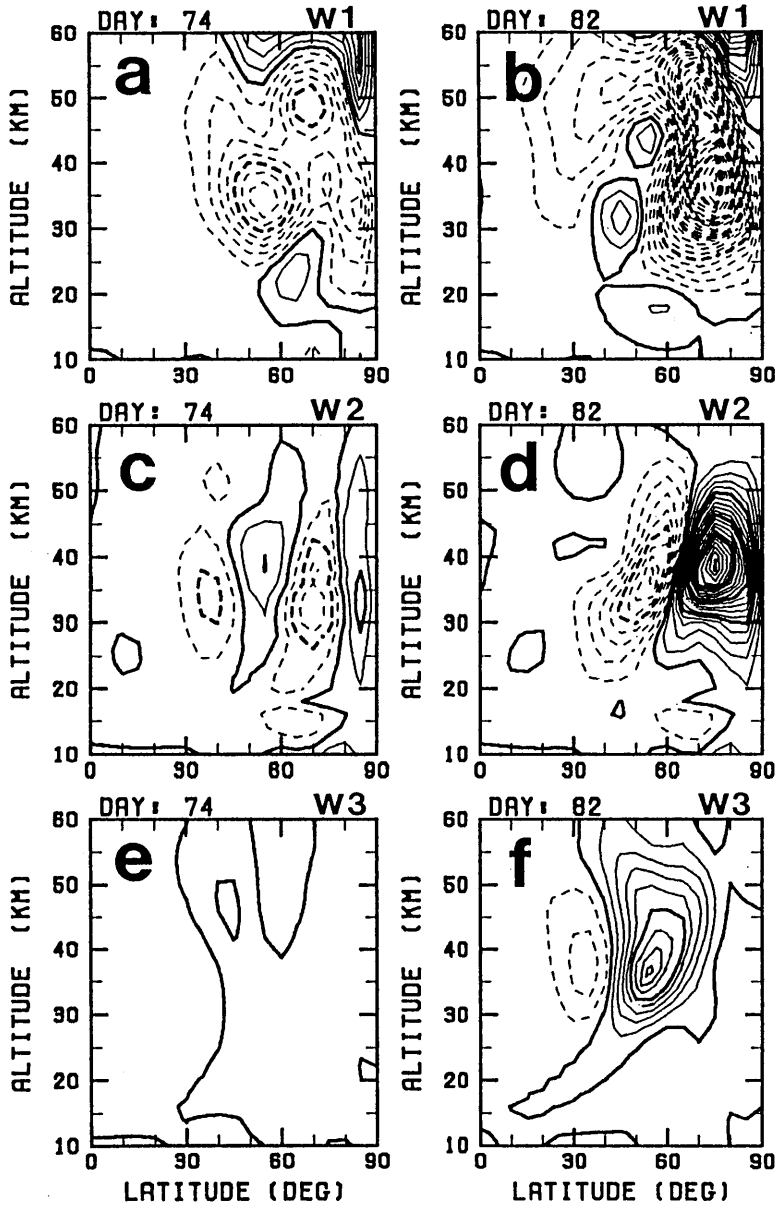

Fig.5.14: Wave driving of waves 1-3 in a meridional plane at days 74 and 82. Contour interval of wave driving is 10^{-5} ms^{-2}.

5.4 Role of wave-wave interaction

5.4.1 Role of wave 1-wave 2 interaction

The direct transfers of energy and PE to wave 1 due to wave-wave interaction do not cause the amplification of wave 1 as mentioned in Sections 4a and 4b. The interaction, however, must play an essential role in the periodic variation of wave 1 as stated in the last of previous subsection. Here, the details of the role of the interaction between wave 1 and wave 2 are considered.

The changes of vorticity in wave 1 due to wave-wave interaction are qualitatively considered using the vorticity equation. Under simplified conditions, the wave-wave interaction in the vorticity equation plays following roles; when the phases of waves 1 and 2 are overlapping, the phase of wave 1 moves eastward in the polar side of the wave center while it moves westward in the equatorial side. In turn, if the ridge of wave 2 is located at 90° apart from that of wave 1, the phase of wave 1 moves westward in the polar side and eastward in the equatorial side. Furthermore, if the ridge of wave 2 trails wave 1 by 45° , wave 1 receives kinetic energy and PE from wave 2 in the polar side and supplies them to wave 2 in the equatorial side. When the ridge of wave 2 is 45° ahead of wave 1, the energy and PE conversion are opposite to the previous case. Details of the discussion are presented in Appendix D.

Temporal variations of the conversion of kinetic energy due to wave-wave interactions in the upper region (30-110 km), integrated over the equatorial side (0°-60°) and polar side (65°-90°) of the polar night jet, are shown in Fig.5.15. The wave-wave interaction term of wave 1 varies opposite to that of wave 2 on both sides of the jet. This indicates that waves 1 and 2 periodically transfer energies each other. Variations over the equatorial and polar sides are also negatively correlated for both waves 1 and 2.

By comparing Fig.5.15 and Fig.5.1b, the following relationship can be determined. The interaction term of wave 1 has a negative peak on the equatorial side and a positive peak on the polar side when the wave 2 ridge lags approximately 45° behind the phase of wave 1. Conversely the term has a positive peak on the equatorial side and a negative peak on the polar side when the ridge of wave 2 is about 45° ahead of wave 1. The relations agree with those predicted from the vorticity equation (cf. Appendix E). This contrast in variation between the equatorial and polar sides causes the shift of wave centers on the meridional plane. Indeed, the position of wave 1 amplitude maximum shifts poleward a few degree after wave 1 receives energy in the polar side (Fig.5.2).

The other effect of wave 1-wave 2 interactions on wave 1 is to shift the phase of wave 1 either eastward or westward (Appendix E). The phase movement changes the direction of EP flux since the phase tilt on a horizontal plane is closely related with the meridional component of EP flux.

Figure 5.16 shows the phase lines of the waves at a latitude on polar side (75°) and that on equatorial side (45°). At the polar latitude (Fig.5.16a), the phase of wave 1 moves eastward when the phase of wave 1 and 2 are overlapped. When the longitudinal location of the ridge of wave 2 is within 80-100° from that of wave 1, it moves westward. This phase movement of wave 1 is the same as that predicted from the vorticity equation. The order of the movement velocity of wave phase estimated by (E7) in Appendix E is 10° day^{-1} when wave 2 amplitude is assumed to be 400 m. The eastward and westward movement velocities in Fig.5.17a are about 3° day^{-1} and 10° day^{-1}, respectively. These values are comparable with the estimated value. Namely, the wave-wave interaction

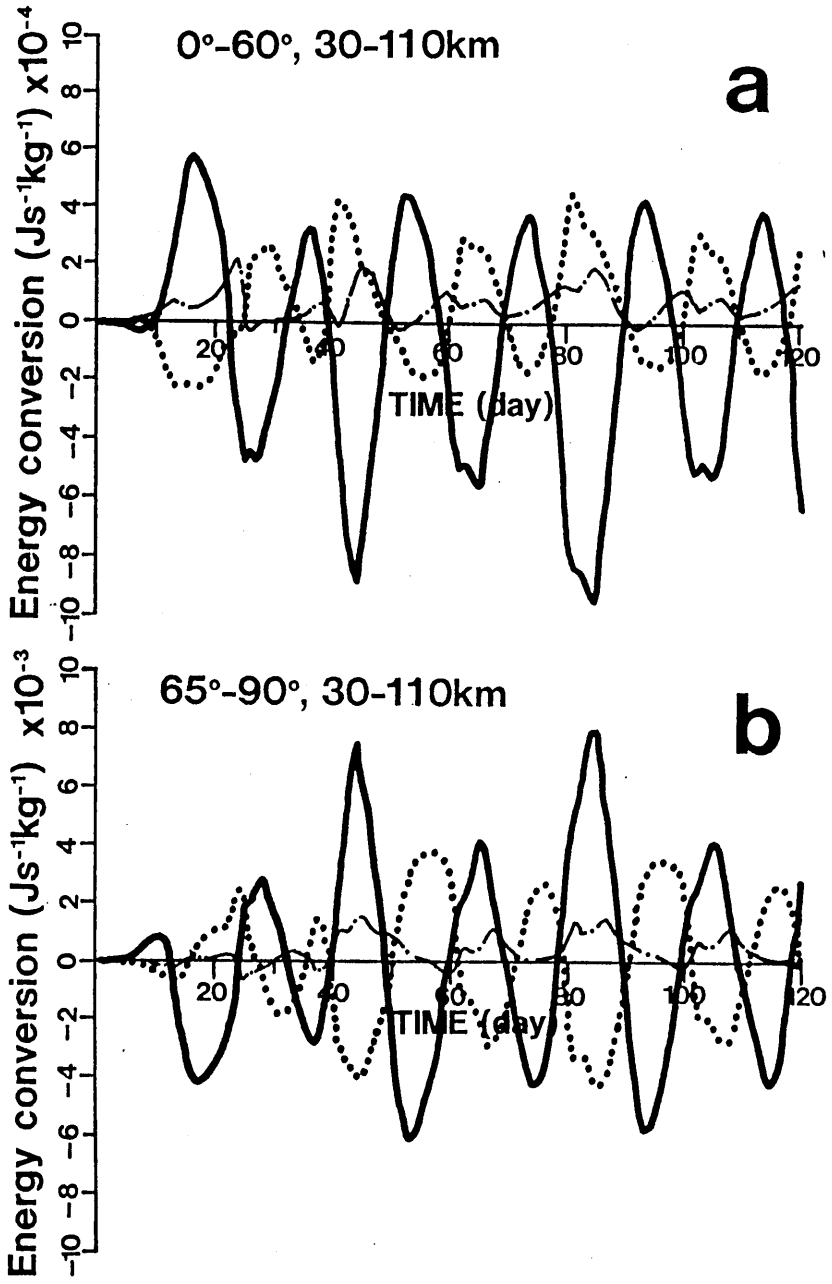

Fig.5.15: Temporal variation of energy conversion averaged over (a) equatorial side in the upper region: 30-110 km in height and 0-60°S in latitude, and over (b) polar side in the upper region: 30-110 km in height and 65-90°S in latitude. Solid line is the variation of wave 1, dotted line wave 2 and dash-dotted line wave 3.

center.

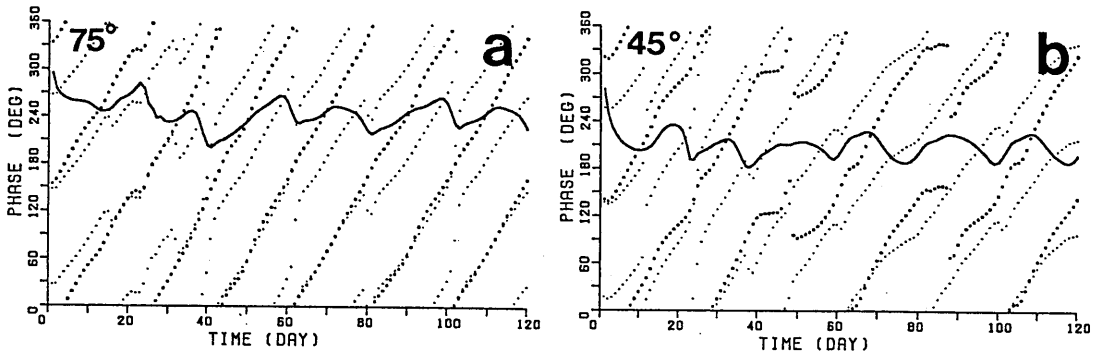

Fig.5.16: The same as in Fig.5.1b but for (a) at 75°S and (b) 45°S .

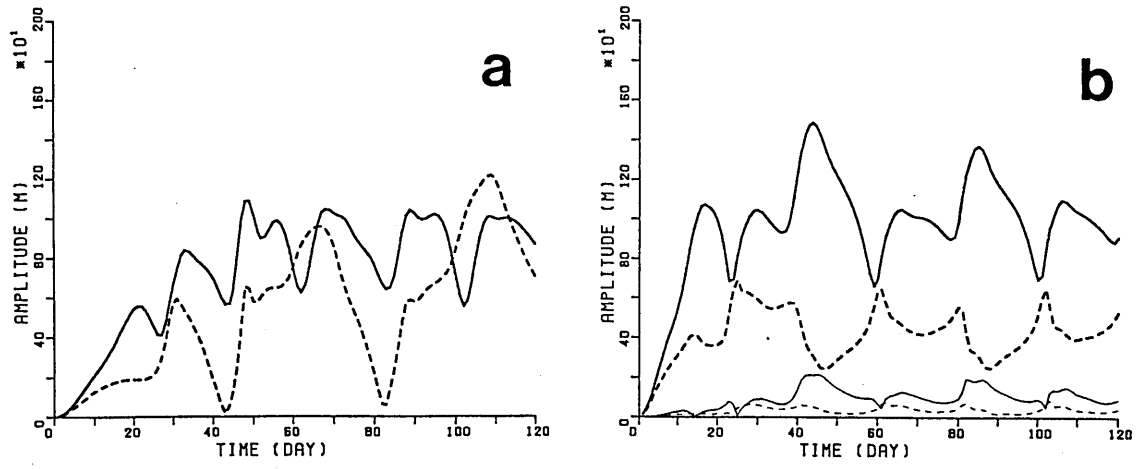

Fig.5.17: Temporal variation of amplitude at 60°S and 40 km. (a) Case for truncation wavenumber of 2. Solid line indicates the wave 1 amplitude, dashed line the wave 2. (b) Case for truncation number of 4. Thick solid line indicates wave 1 amplitude, thick dashed line wave 2, thin solid line wave 3, and thin dashed line wave 4.

The phase movement of wave 1 at a latitude on the equatorial side (Fig.5.16b) does not agree well with that predicted from vorticity equation. When the phase of wave 2 overlaps that of wave 1 (days 32, 69, and 109), the phase movement of wave 1 changes

direction from eastward to westward while it was predicted to move westward during the overlap. The phase movement of wave 1 is opposite to that predicted, when the ridge of wave 2 differs by 90° from wave 1 (days 72, 92, and 112).

The phase movement of wave 1 is also affected by the change of the refractive index. The timing of the eastward movement of wave 1 phase in the midlatitudes after day 30 coincides with the appearance of the negative region of RI. Thus, it is considered that the phase movement in the midlatitudes is controlled by the change of RI rather than the wave-wave interaction.

In this subsection, the role of the interaction between wave 1 and wave 2 was explored. The wave-wave interaction results in the periodic energy exchange between the waves and alters the horizontal phase tilt of wave 1. During first half of the amplification stage, the wave-wave interaction emphasizes the focus of EP flux of wave 1 to the highlatitudes stratosphere through the phase movement. The direct energy and enstrophy transfer to wave 1 from wave 2 shifts the position of amplitude maximum of wave 1 to the highlatitudes during the last half of the amplification stage.

5.4.2 Role of wave 3

Wave 3 also has an important part in the system of wave-mean flow interactions, although the amplitude of wave 3 only reaches about 250 m in maximum. When wave 3 is excluded from the system, the characteristics of the amplitude variation differ considerably from those when wave 3 is included. The variation of the wave amplitude, when wave 3 is excluded, is shown in Fig.5.17a, calculated under the same conditions of initial zonal-mean wind and wave forcing as in Case A1. The amplitude of wave 2 is as large as wave 1 and the amplifications of waves 1 and 2 are rather well in phase. Moreover, the subharmonic variation does not appear and the variation is more random.

When wave 4 is included in the system (i.e., the truncation number is 4), the variation of wave amplitude is slightly modified from Case A1. The amplitude variations of the four waves are shown in Fig.5.17b. The characteristics of the variations are quite similar to those of Case A1 except that the shapes of the maximum peaks of wave amplitude are somewhat sharp. Hence, it is concluded that the system of the variation is almost closed to the interactions among waves 1, 2, 3 and the zonal-mean flow.

The wave-wave interaction term between waves 1 and 2 in the vorticity equation generates not only wave 1, but also wave 3 (cf. Appendix E). Indeed, the wave interaction term of wave 3 is comparable to those of waves 1 and 2 (see Fig.5.10). Therefore, wave 3 must be involved in the system in order to simulate the interaction between planetary waves and the zonal-mean flow. On the other hand, wave 4 is generated by the interaction between waves 1 and 3, and two of wave 2. These may not be essential within the present system; the first interaction term is negligible due to the smallness of the wave 3 amplitude and the second interaction is also small compared with the interaction between waves 1 and 2 because the amplitude of wave 2 is usually smaller than wave 1.

5.5 Summary and discussion

It has been shown that the large temporal variation of quasi-stationary wave 1 results from the interaction between wave 1 and the eastward traveling wave 2. The calculated results were found to have similar characteristics to those observed, which can be summarized as follows.

Wave 1 amplitude reaches a maximum value ($\sim$ 2000 m) when the ridge of wave 2 overlaps that of wave 1. The amplitude of wave 2 is negatively correlated to wave 1. The degree of amplification varies according to the initial conditions and forcing. In many cases the large amplification of wave 1 occurs only once for every two passages of wave 2 over wave 1. The velocity of the polar night jet is minimum when the amplitude of wave 1 reaches its maximum.

From the energetics analysis, it was found that the amplification of wave 1 results from the abrupt decrease in the conversion of kinetic energy to the zonal-mean flow while the decay is caused by the energy transfer to wave 2. This feature was revealed more clearly by the analysis of the potential enstrophy conversion. The abrupt decrease of the energy conversion to the zonal-mean flow is due to the change of direction of EP flux. EP flux of wave 1 changes its direction from equatorward to almost vertical early stage of the amplification.

The process of the amplification is as follows. Before the amplification, wave 1 propagates upward and equatorward which is accompanying with poleward momentum transport. The zonal-mean wind is accelerated in the highlatitudes and decelerated in the midlatitudes, which lead to the enhancement of latitudinal shear of the zonal-mean wind . In the course of time, the negative region appears in the midlatitudes and the wave guide forms at the highlatitudes. Then, wave 1 propagates almost vertically in the wave guide.

The wave-wave interaction not only results in a direct exchange of their kinetic energies but also alters the horizontal phase tilt of wave 1. The direct energy transfer due to the interaction term is opposite between the equatorial and polar sides of the wave center, which leads to the movement of the position of the wave center. The interaction affects the degree of wave-mean flow interaction through the phase movement of wave 1. During first half of the amplification stage, the phase movement due to the wave-wave interaction enhances the focus of EP flux to the highlatitudes. While the direct energy transfer shift the position of the wave center poleward during later half if the stage.

Furthermore, it was found that wave 3 and the variation of the zonal mean flow also play important roles in the interaction system. If wave 3 was excluded from the system, the variation was changed considerably from that when wave 3 was included.

6 Conclusions

The planetary waves, as well as gravity waves, propagating into the stratosphere from the troposphere play important roles on the transports of momentum and materials in the stratosphere. Divergences of wave momentum accelerate or decelerate the zonal-mean wind and induce a meridional circulation in the middle atmosphere. Differences of wave activity between SH and NH cause asymmetrical patterns of dynamical quantities and materials.

The zonal-mean column ozone content in NH winter is monotonously increased toward to the pole, while that in SH has a maximum value at midlatitudes, called *subpolar maximum*. The first subject in this paper is to reveal the roles of planetary waves to form the subpolar maximum.

The activity of the planetary waves in SH is usually weaker compared with in NH. However, significant intraseasonal variations of the wave amplitude are observed even in the SH stratosphere. The most typical variation observed in SH is the quasi-periodic amplification of wavenumber 1. The amplification is well matched with overlapping of an eastward traveling wave with wavenumber 2.

The second subject in this study is to simulate the realistic variation of horizontal distribution of total ozone content through interactions of stationary wave with wavenumber 1 and eastward traveling wave with wavenumber 2. The third subject is to explore the mechanism of the wave 1 amplification through the interaction with wave 2.

Numerical experiments were performed using three dimensional model to express transient dynamical processes and accompanied ozone transports. The spherical version of the model was used to experiments calculating ozone transports (Sections 3 and 4) and the hemispheric version was used to examine wave 1 amplification (Section 5). The knowledges presented in this study are summarized as follows.

1. The series of numerical experiments of ozone transports showed that planetary waves in SH produce the subpolar ozone maximum at midlatitude and realize the seasonal change of the latitudinal location of the subpolar maximum. Total ozone content in SH winter is increased mostly in midlatitudes around 40° -50° and the position of subpolar maximum gradually shifts poleward from midwinter to early spring. This suggested that the seasonal variation of the subpolar maximum is controlled by the planetary waves. The circulation in SH winter does not reach the polar region and its downward motion is concentrated in midlatitudes. The location of downward motion shifts to higher latitudes as the season progresses similar to the corresponding maximum of the column ozone.

2. The difference of the meridional circulation depends on the structure of initial zonal-mean wind in each hemisphere. The zonal-mean wind in SH midwinter (before the

formation of highlatitude jet) forms equatorward tilt of refractive index and then prevents the propagation of planetary waves to higher latitudes.

3. Quasi-periodic amplification of wave 1 can be simulated in the framework of the interaction among stationary wave with wavenumber 1, eastward traveling wave with wavenumber 2 and zonal-mean wind. The calculated horizontal distribution of total ozone content and its temporal variation have considerable similarity with observation in SH winter.

4. Energetics and potential vorticity analysis reveal the mechanism of the amplification. The amplification of wave 1 results from the abrupt decrease associated with the conversion of kinetic energy to the zonal-mean flow. The decrease of the energy conversion to the zonal-mean flow at the first stage of the amplification is due to the change of direction of EP flux of wave 1 from equatorward to almost vertical. The wave-wave interactions also contribute to amplify wave 1. Increase of the energy flow from wave 2 and wave 3 to wave 1, is resulted from reduction of the horizontal (north-south) phase tilt of wave 1 rather than a direct exchanges of their kinetic energies.

Numerical experiments in this study were performed under idealized conditions using models including dynamical processes and simplest radiative process only. The phenomena occurring in the real atmosphere are more complex than simulated phenomena in this study. The phenomena simulated in General Circulation Model (GCM) including tropospheric processes and complex chemical and radiative processes are also complicated. Therefore, the presented knowledge in this study is expected to be extracted from data obtained by observations and GCM by critical analysis.

Acknowledgments

I wish to greatly thank Prof. H. Tanaka of Nagoya University for his encouragement and support all the time since I was a student of the university. I am very grateful to Prof. N. Morii of Numazu College of Technology for his support to continue this study.

I would like to thank Prof. I. Hirota and Dr. S. Yoden of Kyoto University, and Prof. K. Yamazaki and Dr. M. Shiotani of Hokkaido University for their critical comments on this study. My thanks are also extended to researchers who encourage me: Prof. S. Miyahara of Kyushu University, Dr. M. Yamanaka and Dr. K. Sato of Kyoto University, Dr. Y. Akiyoshi of National Institute for Environmental Science, Dr. K. Kodera of Meteorological Research Institute, Prof. H. L. Tanaka of Tsukuba University, and anonymous persons.

I am also grateful to reviwers of this thesis: Prof. T. Takeda, Prof. K. Nakamura, and Prof. Y. Kondo of Nagoya University. Furthermore, I wish to extend my thanks to many parsons of the Institute for Hydrospheric-Atmospheric Sciences at Nagoya University, especially to members of the laboratory of Atmospheric Physics. Also, I appreciates secretaries of the institute.

Data set of monthly mean zonal wind userd in this study was offered by NASA/Goddard Space Flight Center. TOMS data was supplied by Goddard Distributed Active Archive Center of NASA.

Numerical model used in this study was developed and run on computers in Nagoya University Computation Center. Most of the figures were drawn using NCARG developed by NCAR, and a part of them was produced by GFD-DENNOU Library developed by GFD-DENNOU Club.

A part of this study was supported by World Climate Research Programme (WCRP) in Japan and a Grant-in-Aid for encouragement of young scientists sponsored by the Ministry of Education, Science, and Culture of Japan.

This study was mainly performed during doctoral course of the Department of Science at Nagoya University.

APPENDIX A

List of Symbols

a	radius of the earth
c	phase velocity
D_F	wave driving
f	Coriolis parameter
$\mathbf{F}$	Eliassen-Palm flux (EP flux) (cf. Eq.(3.4))
H	scale height (=7 km)
k	zonal wavenumber
N_{BV}	Brunt-Väisälä frequency ($= 2 \times 10^{-2}\text{sec}^{-1}$)
q	zonal-mean potential vorticity
Q_k	refractive index for wavenumber m (cf. Eq.(3.5))
R	gas constant of dry air
t	time
T	temperature
t	time
$u, \overline{u}$	zonal wind and its zonal-mean component
$v, \overline{v}$	meridional wind and its zonal-mean component
$\overline{v}^*$	residual meridional wind (cf. Eq.(3.2))
$\overline{w}^*$	residual vertical wind (cf. Eq.(3.3))
$w, \overline{w}$	vertical wind and its zonal-mean component
z	log-pressure coordinate
α	Newtonian cooling coefficient
θ	latitude
ν_{RF}	Rayleigh friction coefficient
ν_z	biharmonic vertical diffusion coefficient (cf. Eqs.(2.6))
λ	longitude
β	latitudinal gradient of the Coriolis parameter
ρ_0	basic air density ($\rho_0 = \rho_s \exp(-z/H)$)
ρ_s	standard air density at the surface ($\rho_s = 1.3\ \text{kg}\,\text{m}^{-3}$)
ϕ'	perturbed geopotential
$\chi, \overline{\chi}$	ozone mixing ratio and its zonal-mean component
Ω	angular frequency of the earth's rotation

APPENDIX B

Wave-wave interaction terms

The wave-wave interaction terms in Eqs.(2.16),(2.17) and (2.18) are written as follows:
For $2 \leq k \leq N-1$,

$$\begin{aligned} A_k &= -e^{\frac{z}{2H}}\Big\{\frac{2i}{a\cos\theta}\Big[\sum_{n=1}^{k-1} nU_{k-n}U_n + \sum_{n=k+1}^{N} nU^*_{n-k}U_n - \sum_{n=1}^{N-k} nU_{k+n}U^*_n\Big] \\ &\quad + \frac{1}{a\cos^2\theta}\frac{\partial}{\partial\theta}\Big[(\sum_{n=1}^{k-1} U_{k-n}V_n + \sum_{n=k+1}^{N} U^*_{n-k}V_n + \sum_{n=1}^{N-k} U_{k+n}V^*_n)\cos^2\theta\Big]\Big\} , \end{aligned} \tag{B1}$$

$$\begin{aligned} B_k &= -e^{\frac{z}{2H}}\Big\{\frac{i}{a\cos\theta}\Big[\sum_{n=1}^{k-1} n(V_{k-n}U_n + U_{k-n}V_n) + \sum_{n=k+1}^{N} n(V^*_{n-k}U_n + U^*_{n-k}V_n) \\ &\qquad - \sum_{n=1}^{N-k} n(V_{k+n}U^*_n + U_{k+n}V^*_n)\Big] \\ &\quad + \frac{1}{a\cos\theta}\frac{\partial}{\partial\theta}\Big[(\sum_{n=1}^{k-1} V_{k-n}V_n + \sum_{n=k+1}^{N} V^*_{n-k}V_n + \sum_{n=1}^{N-k} V_{k+n}V^*_n)\cos\theta\Big] \\ &\quad + \frac{\tan\theta}{a}\Big[(\sum_{n=1}^{k-1} U_{k-n}U_n + \sum_{n=k+1}^{N} U^*_{n-k}U_n + \sum_{n=1}^{N-k} U_{k+n}U^*_n)\Big]\Big\} , \end{aligned} \tag{B2}$$

$$\begin{aligned} C_k &= -e^{\frac{z}{2H}}\Big\{\frac{i}{a\cos\theta}\Big[\sum_{n=1}^{k-1} n(T_{k-n}U_n + U_{k-n}T_n) + \sum_{n=k+1}^{N} n(T^*_{n-k}U_n + U^*_{n-k}T_n) \\ &\qquad - \sum_{n=1}^{N-k} n(T_{k+n}U^*_n + U_{k+n}T^*_n)\Big] \\ &\quad + \frac{1}{a\cos\theta}\frac{\partial}{\partial\theta}\Big[(\sum_{n=1}^{k-1} T_{k-n}V_n + \sum_{n=k+1}^{N} T^*_{n-k}V_n + \sum_{n=1}^{N-k} T_{k+n}V^*_n)\cos\theta\Big]\Big\} . \end{aligned} \tag{B3}$$

For $k = 1$,

$$A_1 = -e^{\frac{z}{2H}}\Big\{\frac{2i}{a\cos\theta}\Big[\sum_{n=2}^{N} nU^*_{n-1}U_n - \sum_{n=1}^{N-1} nU_{1+n}U^*_n\Big] + \frac{1}{a\cos^2\theta}\frac{\partial}{\partial\theta}\Big[(\sum_{n=2}^{N} U^*_{n-1}V_n + \sum_{n=1}^{N-1} U_{1+n}V^*_n)\cos^2\theta\Big]\Big\} , \tag{B4}$$

$$B_1 = -e^{\frac{z}{2H}}\Big\{\frac{i}{a\cos\theta}\Big[\sum_{n=2}^{N} n(V^*_{n-1}U_n + U^*_{n-1}V_n) - \sum_{n=1}^{N-1} n(V_{1+n}U^*_n + U_{1+n}V^*_n)\Big] + \frac{1}{a\cos\theta}\frac{\partial}{\partial\theta}\Big[(\sum_{n=2}^{N} V^*_{n-1}V_n + \sum_{n=1}^{N-1} V_{1+n}V^*_n)\cos\theta\Big] + \frac{\tan\theta}{a}\Big[(\sum_{n=2}^{N} U^*_{n-1}U_n + \sum_{n=1}^{N-1} U_{1+n}U^*_n)\Big]\Big\} , \tag{B5}$$

$$C_1 = -e^{\frac{z}{2H}}\Big\{\frac{i}{a\cos\theta}\Big[\sum_{n=2}^{N} n(T^*_{n-1}U_n + U^*_{n-1}T_n) - \sum_{n=1}^{N-k} n(T_{1+n}U^*_n + U_{1+n}T^*_n)\Big] + \frac{1}{a\cos\theta}\frac{\partial}{\partial\theta}\Big[(\sum_{n=2}^{N} T^*_{n-1}V_n + \sum_{n=1}^{N-k} T_{1+n}V^*_n)\cos\theta\Big]\Big\} . \tag{B6}$$

For $k = N$,

$$A_N = -e^{\frac{z}{2H}}\Big\{\frac{2i}{a\cos\theta}\sum_{n=1}^{N-1} nU_{N-n}U_n + \frac{1}{a\cos^2\theta}\frac{\partial}{\partial\theta}\Big(\sum_{n=1}^{N-1} U_{N-n}V_n\cos^2\theta\Big)\Big\} , \tag{B7}$$

$$B_N = -e^{\frac{z}{2H}}\Big\{\frac{i}{a\cos\theta}\sum_{n=1}^{N-1} n(V_{N-n}U_n + U_{N-n}V_n) + \frac{1}{a\cos\theta}\frac{\partial}{\partial\theta}\Big(\sum_{n=1}^{N-1} V_{N-n}V_n\cos\theta\Big) + \frac{\tan\theta}{a}\sum_{n=1}^{N-1} U_{N-n}U_n\Big\} , \tag{B8}$$

$$C_N = -e^{\frac{z}{2H}}\Big\{\frac{i}{a\cos\theta}\Big[\sum_{n=1}^{N-1} n(T_{N-n}U_n + U_{N-n}T_n)\Big] + \frac{1}{a\cos\theta}\frac{\partial}{\partial\theta}\Big(\sum_{n=1}^{N-1} T_{N-n}V_n\cos\theta\Big)\Big\} . \tag{B9}$$

Appendix C

Relationship between residual circulation and material circulation

A residual circulation derived from TEM theory strictly represents a Lagrangian-mean circulation (material circulation) only when the planetary wave amplitude is infinitesimal and the state is steady (Andrews and McIntyre 1978). Indeed, as shown by Iwasaki (1989), the circulation obtained by a pressure-isentrope hybrid coordinate, which represents well Lagrangian-mean circulation even if the wave amplitude is large, is substantially different from the residual circulation obtained by TEM used in present study. Schneider and Geller (1985) also concluded that the value induced by the residual circulation is overestimated about 50 % from a tracer experiment.

To examine the validity of representation of a material circulation by a residual circulation, we compare the ozone distribution calculated from residual circulations with the distribution in section 3. Here, ozone density is calculated using residual circulation based on the following mass conservation equation.

$$\frac{\partial \overline{\chi}}{\partial t} = -\left[\frac{1}{a\cos\theta}\frac{\partial}{\partial\theta}(\overline{\chi}\,\overline{v}^{*}\cos\theta) + \frac{1}{\rho_0}\frac{\partial}{\partial z}(\rho_0\overline{\chi}\,\overline{w}^{*})\right] \quad ,$$

where $\overline{\chi}$ is the mixing ratio of zonal-mean ozone. Calculation of ozone distribution in the text is termed as *direct* calculation and calculation based on residual circulations is termed as *indirect* calculation.

The variations of total ozone content obtained by the indirect calculation, where the standard forcing is applied in SH and NH midwinter, are shown in Fig.C1. In the case of July in SH, the total ozone content increases both in midlatitudes and highlatitudes till day 12. The latitude of the maximum increase is located around 50° S, which is similar to that obtained by direct circulation (Fig.3.5). However, the significant ozone decrease in highlatitudes is not simulated by the indirect calculation.

Characteristics of the ozone variation in the case of January is basically similar to that of the direct calculation. However, the increase of ozone content in highlatitude is about 40% larger than that by the direct calculation. This is consistent with the results of Schneider and Geller (1985).

From the comparison between direct and indirect calculations of total ozone content, it is verified that residual circulations approximately represent material circulations with some uncertainties.

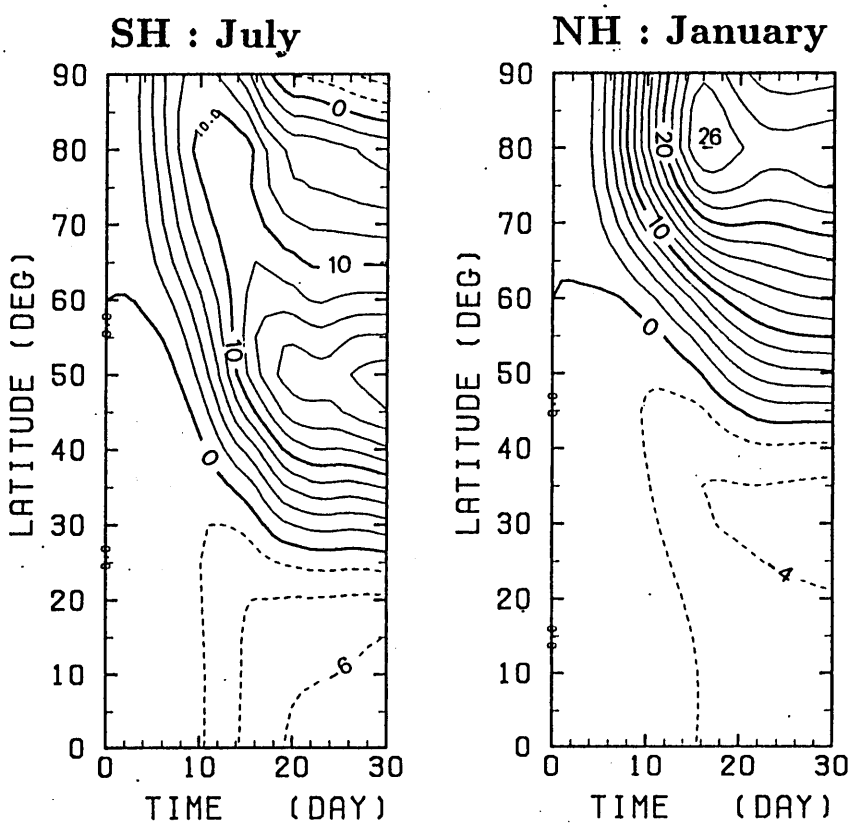

Fig.C1 Deviation of ozone amount from its initial value calculated from residual circulation. Left-hand panel shows the case of July in SH and right side shows January case in NH. Contour interval is 2 DU.

APPENDIX D

Energy conversion terms

The exact formula for the second term on the right-hand side of Eq.(5.1) integrated over the upper region can be written

$$C(K_z, K_m) = \frac{1}{M}\int_0^{\pi/2} a\cos\theta\, d\theta \int_{30km}^{110km} \rho_0\, dz \left(\frac{1}{\cos\theta}\frac{\partial}{\partial\theta}(\overline{u}\cos\theta) + 2\tan\theta\overline{u}\right)\overline{u_m v_m}\ , \tag{D1}$$

where u_m and v_m are the zonal and meridional velocities of wavenumber m, respectively. ρ_0 is the air density and M the mass of air in the integrated region. The second term in the bracket on the right-hand side arises from the metric force; this term is smaller than the first term except near the pole.

The third term on the right-hand side of Eq.(5.1) is written as

$$C(E_m) = -\frac{1}{M}\int_0^{\pi/2} a\cos\theta d\theta \int_{30km}^{110km} \rho_0\, dz \left\{\frac{1}{a\cos\theta}\frac{\partial}{\partial\theta}(\overline{\phi_m v_m}\cos\theta) + \frac{1}{\rho_0}\frac{\partial}{\partial z}(\rho_0\overline{\phi_m w_m})\right\}\ , \tag{D2}$$

where w_m is the vertical velocity, and ϕ_m the geopotential. With the aid of the upper and lateral boundary conditions of $\phi_m = 0$ at z=110km and $\theta = 0, 90°$, the equation for this term can be written as

$$C(E_m) = \frac{1}{M}\int_0^{\pi/2} a\cos\theta\, d\theta \left[\rho_0\overline{\phi_m w_m}\right]_{z=30km}\ . \tag{D3}$$

Consequently, this term is equivalent to the meridionally integrated vertical energy flux at the 30 km level.

APPENDIX E

Effects of the wave 1 - wave 2 interaction on wave 1

The temporal change of vorticity due to the interaction between wave 1 and wave 2 arising from advection term can be written as

$$\frac{\partial \zeta}{\partial t} = -u_2\frac{\partial \zeta_1}{\partial x} - u_1\frac{\partial \zeta_2}{\partial x} - v_2\frac{\partial \zeta_1}{\partial y} - v_1\frac{\partial \zeta_2}{\partial y} , \tag{E1}$$

where ζ is the vorticity, u the zonal wind, v the meridional wind, x and y the longitudinal and latitudinal axes, respectively. Subscripts with the variables denote the wavenumber. It is assumed that the maximum amplitudes of wave 1 and 2 are located at the same latitude ($y = 0$) and the phase of the waves do not tilt in the horizontal plane. The waves are confined in a channel with the width of $L(= \pi/l)$. Consequently, by using the geopotential, the waves are given by

$$\phi_1 = A_1 \cos kx \cos ly, \qquad \phi_2 = A_2 \cos\left(2(kx + \varphi)\right) \cos ly , \tag{E2a, b}$$

where A_1 and A_2 are the amplitudes of waves 1 and 2, respectively. k is the zonal wavenumber with $k = 1$ if x is written in longitudinal units of radians. φ is the difference in the location of the ridge of wave 2 from that of wave 1. Moreover, it is postulated that the zonal and meridional winds satisfy the geostrophic relationship

$$u = -\frac{1}{f}\frac{\partial \phi}{\partial y}, \qquad v = \frac{1}{f}\frac{\partial \phi}{\partial x} , \tag{E3a, b}$$

where f is Coriolis parameter which is assumed to be constant. Then the vorticity can be written as

$$\zeta = \frac{1}{f}\left(\frac{\partial^2}{\partial x^2} + \frac{\partial^2}{\partial y^2}\right)\phi . \tag{E3c}$$

1. Tendency when φ =0° or 90°

The temporal variation of wave 1 is considered when the ridge of wave 2 overlaps that of wave 1. Substituting Eq.(E2) with φ=0° into Eq.(E3) and after the simple calculation of Eq.(E1) combined with Eq.(E3), the following formula is obtained

$$\frac{\partial \zeta}{\partial t} = -\frac{3}{4f^2}A_1 A_2 k^3 l \sin 2ly(3 \sin kx + \sin 3kx) . \tag{E4}$$

The temporal tendency of the geopotential of wave 1 is written as follows, with the aid of Eq.(E3c)

$$\frac{\partial \phi_1}{\partial t} = \frac{9}{4f}A_1 A_2 \frac{k^3 l}{k^2 + l^2} \sin kx \sin 2ly . \tag{E5}$$

This equation denotes that wave 1 tends to shift eastward on the poleward side of the wave center ($y > 0$) and westward on the equatorward side ($y < 0$). This is illustrated in Fig. D1.

If the location of the ridge of wave 2 is 90° from that of wave 1 (i.e., φ=90°), the phase movement of wave 1 is opposite to the case of φ =0° . Namely, the vortex tends to shift westward on the poleward side and eastward on the equatorward side.

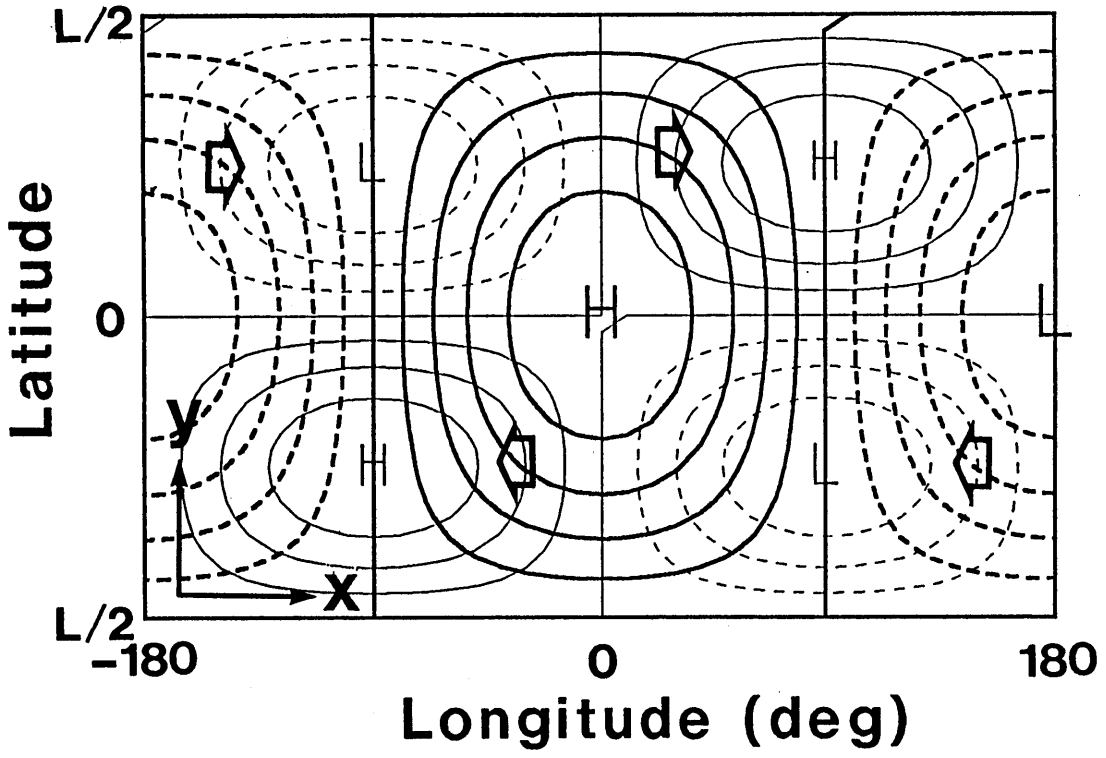

Fig.E1 Schematic figure of wave 1 phase movement due to the wave 1 - wave 2 interaction when the ridge of wave 2 overlaps the ridge of wave 1. Thick solid and dashed lines denote the geopotential field of wave 1 (Eq.E2a). Thin solid and dashed lines denote the distribution of the temporal tendency of geopotential for wave 1 (Eq.E7). Arrows show the direction of the phase movement.

2. Tendency when φ=45° or -45°

When the ridge of wave 2 is located 45° behind that of wave 1 (φ=45°), the tendency equation of vorticity can be written as

$$\frac{\partial \zeta}{\partial t} = -\frac{3}{4f^2} A_1 A_2 k^3 l \sin 2ly(3\cos kx + \cos 3kx) \ . \tag{E6}$$

With the aid of Eq.(E3c), the tendency of geopotential of wave 1 can be written as

$$\frac{\partial \phi_1}{\partial t} = \frac{9}{4f} A_1 A_2 \frac{k^3 l}{k^2 + l^2} \sin kx \sin 2ly \ . \tag{E7}$$

This equation denotes that wave 1 grows on the poleward side of the vortex center and weakens on the equatorward side.

If the ridge of wave 2 is located 45° ahead of the wave 1 (i.e., φ=-45°), the tendency is the reverse of that for φ=45° . Namely, wave 1 tends to decay on the poleward side and to amplify on the equatorward side.

It should be noted that the net energy and PE transfer between wave 1 and 2 due to the advection term can not take place because the energy and PE transfers on the poleward and equatorward sides cancels each other in this simplified configuration. However, if the phase of a wave in a horizontal plane has a relative tilt between wave 1 and wave 2, the tilt causes a time lag in the interaction between the poleward and equatorward side. In this case, net energy and PE transfers take place.

REFERENCES

Akiyoshi, H. and M. Uryu, 1992: Diagnostic model study of the seasonal variation of global ozone and the antarctic ozone hole. *J. Geophys. Res.*, **97**, 20837-20853.

Andrews, D. G. and M. E. McIntyre, 1976: Planetary waves in horizontal and vertical shear: The generalized Eliassen-Palm relation and the mean zonal acceleration. *J. Atmos. Sci.*, **33**, 2031-2048.

Andrews, D. G. and M. E. McIntyre, 1978: An exact theory of nonlinear waves on a Lagrangian-mean flow. *J. Fluid Mech.*, **89**, 609-646.

Bowman, K. P., 1990: Evolution of the total ozone field during the break down of the Antactic circumpolar vortex. *J. Geophys. Res.*, **95**, 16529-16543.

————, K. P., and A. J. Krueger, 1985: A global climatology of total ozone from Nimbus 7 total ozone mapping spectrometer. *J. Geophys. Res.*, **90**, 7967-7976.

Charney, J. G. and M. E. Stern, 1962: On the stability of internal baroclinic jets in a rotating atmosphere. *J. Atmos. Sci.*, **19**, 159-172.

Dütsch H. U., 1971: Photochemistry of atmospheric ozone. Advances in Geophysics (Academic Press), **15**, 219-322.

Fleming, E. L., S. Chandra, M. R. Shoeberl, and J. J. Barnett, 1988: Monthly mean global climatology of temperature, wind, geopotential height, and pressure for 0-120 km, *NASA Technical Memorandum*, **100697**.

Geisler, J. E. and R. R. Garcia, 1977: Baroclinic instability at long wavelengths on a β -plane, *J. Atmos. Sci.*, **34**, 311-321.

Geller, M. A. and M.-F. Wu, 1987: Troposphere-stratosphere circulation statics, *Transport processes in the middle atmosphere* (D. Reidel publishing company, Dordecht), 3-17.

Hartmann, D. L., 1976: The structure of the southern hemisphere in the southern hemisphere during late winter 1973 as observed by satellite, *J. Atmos. Sci.*, **33**, 1141-1154.

————, 1979: Baroclinic instability of realistic zonal-mean states to planetary waves. *J. Atmos. Sci.*, **36**, 2336-2349.

————, 1983: Barotropic instability of polar night jet stream. *J. Atmos. Sci.*, **40**, 817-835.

————, C. R. Mechoso and K. Yamazaki, 1984: Observations of wave-mean flow interaction in the southern hemisphere. *J. Atmos. Sci.*, **41**, 351-362.

————, C. R. Mechoso, and K. Yamazaki, 1984: Observations of wave-mean flow interaction in the Southern Hemisphere. *J. Atmos. Sci.*, **41**, 351-362.

Harwood, R. S., 1975: The temperature structure of the southern hemisphere stratosphere August-October 1971. *Quart. J. Roy. Meteor. Soc.*, **101**, 75-91.

Hirooka, T., 1986: Influence of normal mode Rossby waves on the mean field: influence with quasi-stationary waves. *J. Atmos. Sci.*, **43**, 2088-2097.

Hirota, I., 1971: Excitation of planetary Rossby waves in the winter stratosphere by periodic forcing. *J. Meteor. Soc. Japan*, **49**, 439-449.

————, K. Kuroi and M. Shiotani, 1990: Midwinter warmings in the southern hemisphere in 1988, *Quart. J. Roy. Meteor. Soc.*, **116**, 929-941.

Holton J. R., 1976: A semi-spectral model for wave-mean flow interactions in the stratosphere: Application to sudden stratospheric warmings. *J. Atmos. Sci.*, **33**, 1639- 1649.

————, and C. Mass, 1976: Stratospheric vacillation cycles. *J. Atmos. Sci.*, **33**, 2218-2225.

Hou, A. Y., H. R. Schneider and M. K. W. Ko, 1991: A dynamical explanation for the asymmetry in zonally averaged column abundances of ozone between northern and southern springs. *J. Atmos. Sci.*, **48**, 547-556.

Hsu, C.-P. F., 1981: A numerical study of the role of wave-wave interactions during sudden stratospheric warmings. *J. Atmos. Sci.*, **38**, 189-214.

Iwasaki, T., 1989: A diagnostic formulation for wave-mean flow interactions and Lagrangian-mean circulation with a hybrid vertical coordinate of pressure and isentropes. *J. Meteor. Soc. Japan*, **67**, 293-312.

————, 1992: General circulation diagnosis in the pressure-isentrope hybrid vertical coordinate. *J. Meteor. Soc. Japan*, **70**, 673-687.

Kanzawa, H. and S. Kawaguchi, 1990: Large stratospheric sudden warming in Antarctic late winter and shallow ozone hole in 1988. *Geophy. Res. Lett.*, **17**, 77-80.

Kruger, A. J., D. F. Heath and C.L. Mateer, 1973: Variations in the stratospheric ozone field inferred from nimbus satellite observations. *Pure Appl. Geophys.*, **106-108**, 1254-1263.

Leovy, C. B. and P. J. Webster, 1976: Stratospheric long waves: Comparison of thermal structure in northern and southern hemispheres, *J. Atmos. Sci.*, **33**, 1624-1638.

Madden, R. A., 1978: Further evidence of traveling waves. *J. Atmos. Sci.*, **35**, 1605-1618.

Manney, G. L., J. D. Farrara and C. R. Mechoso, 1991a: The behavior of wave 2 in the Southern Hemisphere Stratosphere during late winter and early spring. *J. Atmos. Sci.*, **48**, 976-998.

————, C. R. Mechoso, L. S. Elson and J. D. Farrara, 1991b: Planetary scale waves in the Southern Hemisphere winter and early Spring stratosphere: stability analysis. *J. Atmos. Sci.*, **48**, 2509-2523.

————, L. Froidevaux, J. W. Waters, L.S. Elson, E.F. Fishbein, R.W. . Zurek, 1993: The evolution of ozone observation by UARS MLS in the 1992 late winter Southern ploar votex, *Geo. Res. Lett.*, **20**, 1279-1282.

Matsuno, T., 1971: A dynamical model of the stratospheric sudden warming. *J. Atmos. Sci.*, **28**, 1479-1494.

————, and K. Nakamura, 1979: The Eulerian- and Lagrangian-mean circulations in the stratosphere at the time of sudden warming. *J. Atmos. Sci.*, **36**, 640-654.

Mechoso, C. R. and D. L. Hartmann, 1982: An observational study of traveling planetary waves in the southern hemisphere. *J. Atmos. Sci.*, **39**, 1921-1935.

————, D. L. Hartmann and J. D. Farrara, 1985: Climatology and interannual variability of wave, mean-flow interaction in the Southern Hemisphere. *J. Atmos. Sci.*, **42**, 2189-2206.

————, A. O'Neill, V. D. Pope and J. D. Farrara, 1988: A study of stratospheric final warming if 1982 in the southern hemisphere. *Quart. J. Roy. Meteor. Soc.*, **114**, 1365-1384.

Newman, P. A., M. R. Schoeberl and R. A. Plumb, 1986: Horizontal mixing coefficients for two-dimensional chemical models calculated from National Meteorological Center data. *J. Geophys. Res.*, **91**, 7919-7924.

Plumb, R. A. and J. D. Mahlman, 1987: The zonally averaged transport characteristics of the GFDL general circulation/transport model. *J. Atmos. Sci.*, 44, 298-327.

Pyle, J. A. and C. F. Rogers, 1980: A modified diabatic circulation model of stratospheric tracer transport. *Nature*, **287**, 711-714.

Robinson W. A., 1985: A model of the wave 1-wave 2 vacillation in the winter stratosphere, *J. Atmos., Sci.*, **42**, 2289-2304.

Rood, R. B. and M. R. Schoeberl, 1983: Ozone transport by diabatic and planetary wave circulations on β plane. *J. Geophys. Res.*, **88**, 8491-8504.

Rosenfield, J. E., M. R. Schoeberl and M. A. Geller, 1987: A computation of the stratospheric diabatic circulation using an accurate radiative transfer model. *J. Atmos., Sci.*, 44, 859-876.

Schneider, H. R. and M. A. Geller, 1985: A comparison of two- and three-dimensional tracer transport within a stratospheric circulation model. *J. Atmos. Sci.*, **42**, 1792-1808.

Shapiro, R., 1971: The use of linear filtering as a parametrization of atmospheric diffusion. *J. Atmos. Sci.*, **28**, 523-531.

Shiotani, M. and I. Hirota, 1985: Planetary wave-mean flow interaction in the stratosphere: a comparison between northern and southern hemispheres. *Quart. J. Roy. Meteor. Soc.*, **111**, 309-334.

————, K.Kuroi and I. Hirota, 1990: Eastward traveling waves in the southern hemisphere during the spring of 1983, *Quart. J. Roy. Meteor. Soc.*, **116**, 913-927.

Smith, A. K., J. C. Gille and L. V. Lyjak, 1984: Wave-wave interactions in the stratosphere: observations during quiet and active wintertime periods. *J. Atmos. Sci.*, **41**, 363-373.

Tanaka, H. and M. D. Yamanaka, 1985: Atmospheric circulation in the lower stratosphere induced by the mesoscale mountain wave breaking. *J. Meteor. Soc. Japan*, **63**, 1047-1054.

————, 1986: A slowly-varying model of the lower stratosphere zonal wind minimum induced by mesoscale mountain wave breakdown. *J. Atmos. Sci.*, **43**, 1881-1892.

Ushimaru, S. and H. Tanaka, 1990: Characteristics of internal gravity waves and intertial waves in the lower stratosphere observed by the MU radar. *J. Meteor. Soc. Japan*, **68**, 1-18.

————and ————, 1992: A numerical study of the interaction between stationary Rossby waves and eastward-traveling waves in the Southern Hemisphere stratosphere. *J. Atmos. Sci.*, **49**, 1354-1373.

————and ————, 1994: The role of planetary waves in the formation of inter-hemispheric asymmetry in ozone distribution. *J. Meteor. Soc. Japan*, **72**, 653-670, 1994.

Young, R. E. and H. Houben, 1989: Dynamics of planetary-scale baroclinic waves during southern hemisphere winter, *J. Atmos. Sci.*, **46**, 1365-1383.